2023

Machine Learning Applications in Advanced Additive Manufacturing: Process Modeling, Microstructure Analysis, and Defect Detection

Peter Warren
University of Central Florida

STARS Citation
Warren, Peter, "Machine Learning Applications in Advanced Additive Manufacturing: Process Modeling, Microstructure Analysis, and Defect Detection" (2023). *Electronic Theses and Dissertations, 2020-*. 1693.
https://stars.library.ucf.edu/etd2020/1693

MACHINE LEARNING APPLICATIONS IN ADVANCED ADDITIVE MANUFACTURING: PROCESS MODELING, MICROSTRUCTURE ANALYSIS, AND DEFECT DETECTION

by

PETER WARREN
B.S. University of Central Florida, 2017
M.S. University of Central Florida, 2018

A dissertation submitted in partial fulfilment of the requirements
for the degree of Doctor of Philosophy
in the Department of Mechanical and Aerospace Engineering
in the College of Engineering and Computer Science
at the University of Central Florida
Orlando, Florida

Spring Term
2023

Major Professor: Ranajay Ghosh

ABSTRACT

Non-destructive evaluation (NDE) techniques are critical for assessing the integrity, health, and mechanical properties of materials manufactured from various methods. High fidelity NDE techniques are essential for quality control but often lead to massive data generation. Such a vast data load cannot be manually processed, this leads to a severe bottleneck for process engineers. Machine learning (ML) offers a solution to this problem by providing powerful and adaptable algorithms capable of learning patterns, identifying features, and finding hidden relationships in large sets of data. Various ML models are used in this work to improve predictions, improve measurements, detect anomalies, classify anomalies, segment images, determine material health, and directly model behavior. These neural network or ML models are implemented to perform these tasks by utilizing data gathered through various NDE techniques. Additive manufacturing enables the production of complex geometries and customized parts with reduced waste and lead times. The development of new material printing capability and techniques is necessary to expand its capabilities to produce high-performance parts with unique properties and functionality. Contributions to advanced additive manufacturing are made via the application of customized machine learning algorithms in this work. The development of a novel grain image generation method was completed to improve grain and grain boundary image segmentation methods on microstructure images. Convolutional Neural Networks (CNNs) were also applied to datasets of Stainless Steel Powder to help identify, qualify, and classify the health of the powder prior to print application. A feasibility study of the implementation of Binder Jetting (BJT) is conducted on Martian and Lunar regolith using a simplistic binder in this work. The need for efficient techniques to process data gathered from NDE methods is crucial to enhance the accuracy, efficiency, and speed of the analysis of this data. This will lead to faster development and implementation of advanced manufacturing techniques.

This work is dedicated to my mother, Susan With Perszyk, who showed me what it means to be caring, kind, consistent, loving, determined, hardworking, and unbreakable.

ACKNOWLEDGMENTS

I would like to express my appreciation to my research advisor and thesis chair, Dr. Ranajay Ghosh, who has been an incredible advisor, a skillful motivator, an exemplary example of work-ethic and determination. He has helped me continuously and selflessly during my graduate academic career.

I also give my gratitude to my thesis committee members Dr. Seetha Raghavan, Dr. Jayanta Kapat, and Dr. Gita Sukthankar for their advice, contributions, and support.

I also must give my gratitude to Dr. Ramesh Subramanian, Ranier Valentin, and other engineers at Siemens for the many opportunities they provided to me. They allowed me to use their equipment, taught me many valuable skills, and guided me on my journey to becoming a better engineer.

I must thank all of my colleagues here at the University of Central Florida who assisted me in a variety of ways on my many projects. Hossein Ebrahimi and Hessien Ali were my first lab mates and I am grateful for all of the guidance they provided me during our time in the Cosmos Lab. I learned so much from them. I am also very grateful for the all the time I spent and got to work with Nandhini Raju, Quinten Fouliard, Milos Krsmanovic, Shahjahan Hossain, Pranta Sarkar, Sandip Haldar, and Ryan Horton.

Finally and most importantly, I am and will always be profoundly grateful for my wife Ngan Thuong Vo-Warren and my son Ethan Vo-Warren. They are both perfect in every way, and they have given me everything that I could ever want.

TABLE OF CONTENTS

LIST OF FIGURES

LIST OF TABLES

CHAPTER 1: INTRODUCTION

1.1 Motivation

There is a large amount of data that is generated through (NDE) Non-Destructive Evaluation that could be better processed through a data-driven machine learning approach. A substantial amount of data is gathered every year through NDE techniques. NDE techniques are also constantly being developed and improved. As the techniques become more accurate, precise, and able to collect larger amount of data, engineers will struggle to process this data. The vast majority of these techniques could benefit greatly from (AI) Artificial Intelligence assisted data processing methods. NDE is can be used to determine material health before, during, and after the manufacturing process for a given material. If more knowledge can be derived via a AI approach, then ultimately the material manufacturing process can be improved [1, 2]. The main areas this work will investigate machine learning applications in NDE is in defect detection (Chapter 3), microstructure data collection (Chapter 4), and in material health (Chapter 5)

One of the newest and most innovative ways to construct materials is through additive manufacturing. Additive manufacturing can provide the user with faster component manufacturing times, increased design flexibility, increased customization of material properties, and reduction of waste material. There are several new and innovative methods in additive manufacturing that will be discussed in section 2.1. The increase in techniques has also yield in increase in materials that are able to be printed, such as metallic and ceramic materials. The process to print metallic components are often complex and are currently being improved upon. When NDE is used in conjunction with the construction/printing of a given material, the data that is gathered can then be used to improve the process [3, 4]. This work will investigate new and innovative methods that additive manufacturing can be used (Chapter 6).

Some of the main pitfalls to additive manufacturing are cost of equipment, build size, standard safety regulatory procedures, material selection, and material quality. The selection of materials has grown, and continues to grow, but this is a slow process. The more complex metals that may be desired, are also the ones that are used in the most high temperature and high stress environments. The quality of these metals must be at or above the standard in order to withstand these conditions [5, 6]. The manufacturing of various parts for turbomachinery operations is a very delicate and detail oriented process. The application of heat, hard machining, cutting, and other processes have many variables that can have a direct and drastic effect on the product which is manufactured. This work will use machine learning to help improve existing additive manufacturing methods to allow for components that could be implemented in a turbomachinery environment (Chapter 7).

There are many forms of NDE that help engineers to determine part viability and quality prior to certifying a part for operation [7, 8]. Some of the more commonly implemented NDE techniques include: eddy-current, magnetic-particle, liquid penetrate, radiography, ultrasonic, and visual [9]. All of these techniques produce a significant amount of data and the processing and analyzing of this data can often be both time-consuming and inefficient for humans to perform. Artificial intelligence can either take over completely or play an assistance role in the processing of the massive amounts of data that is produced through NDE. Anytime the data produced is visual (either image or video) then neural networks can have a substantial effect on the processing efficiency of this data. Neural networks are well equipped to process images, but can also be used to process ultrasonic data and eddy-current data[1, 10, 11]. The field of NDE is well suited for the application of neural networks, and will most likely be transformed by it. The increased capability of NDE will also have a key role in improving the field of additive manufacturing.

1.2 Intellectual Merit

This work will make many contributions to the field of machine learning, additive manufacturing, and non destructive evaluation. The three fore mentioned fields all have the potential to work together and improve upon each other. This work is aimed in that direction. The most obvious contributions are in data generation, data collection, data analysis, novel methodology development, existing methodology improvement, and novel methodology feasibility studies.

One of the key ways to improve the collaboration between NDE and machine learning is by creating or collecting relevant data. There is currently a lack of relevant data available online that can be used to develop and improve NDE methods. The availability of data cannot be understated. If data is made available to the public, this will encourage innovation, foster collaboration, facilitate reproducibility, improve model accuracy, and enables more people to have access to this knowledge. All applications in mechanical engineering, materials science, and NDE that produce data can benefit from publishing that data to help encourage machine learning applications. This work provides data for this purpose in a few forms on Kaggle. This work provides particle SEM (scanning electron microscope) images of particles that are to be used in metallic additive manufacturing [12]. This work also provides SEM data and optical microscope data of stainless steel printed on a binder jet printer [13, 14]. This work provides new and innovative ways to examine this data as well, but just publishing the data is a very necessary contribution to the science. These contributions should be encouraged in these fields if growth is desired.

One of the most obvious roles that machine learning or artificial intelligence will be able to immediately contribute to assembly of parts, is through inspection. Machine learning can improve quality control of assembly-style production through direct camera observation by automating the inspection process and identifying defects in real-time. This can help reduce the time and cost of manual inspection while improving the overall quality of the final product. This can be achieved through computer vision techniques that enable cameras to capture images of the assembly process and identify defects using algorithms or neural networks. The ability to train on a dataset of images that have been labeled as good or bad based on specific quality criteria, will be a huge contribution to the manufacturing industry, and by extension the additive manufacturing industry. This work makes contributions to this connection between machine learning and manufacturing in Chapter 3. In this work, a dataset of sheet steel defects is examined. A convolutional neural network is then implemented to determine the type of defects and the locations of defects. A systematic study of this process is completed. Work like this must be done to help allow image processing techniques to be applied to manufacturing for the purposes of quality control.

To better understand the material properties, and the micro-structure of a given material, it is necessary to implement microscopy. This is a standard method to better understand a material. Whether a standard optical microscope is used or an SEM, the images gathered can provide a lot of useful data on the material. These images require a laborious and extensive analysis. Certain features in the images must be identified, quantified, correlated, gathered, and analyzed. Machine learning can also be implemented to assist in the processing of these images as well. In this work, machine learning based image processing techniques were implemented on a variety of metallic microstructure data. The analysis process was completed through traditional methods, through basic machine learning methods, and also new methods were developed. A novel approach to data generation for grain boundaries of metallic micro-structure was developed in this work. This method can be easily expand to other material systems, in the future.

Another important task over the next decade will be the further development of existing additive manufacturing techniques. Sintering is a paramount portion to the success of many of the existing additive manufacturing techniques that are used on advanced materials, such as metallics and ceramics. This work investigates the effect of sintering on material systems that were constructed through binder jetting. This work also examines the effect that sintering has on the final material properties. A feasibility study on binder jetting for both Martian and Lunar regolith was completed in Chapter 6. Another contribution to sintering analysis is made in Chapter 7. In this chapter, a monte carlo style model for sintering behavior is completed and presented. The sintering phenomena is complex, and has held the attention of many brilliant engineers and scientists over the centuries. This behavior needs to continue to receive attention if new and inventive manufacturing methods are to be developed.

1.3 Dissertation Outline

The dissertation is comprised of eight chapters. Chapter 1 is the introduction, which includes motivation of this research, the intellectual merit, and an outline of this work. Chapter 2 is a literature review, it is composed of three sections. The first is additive manufacturing, the second is sintering, and the third is Machine Learning. Chapter 3 is on the utilization of machine learning for detecting defect in manufactured metallic components. Chapter 4 is using machine learning for microstructure analysis. More specifically, Chapter 4, is about segmenting grains from grain boundaries in microscopic images. Chapter 5 is implementing machine learning to determine the quality of powder for additive manufacturing purposes. Chapter 6 is a feasibility study on the implementation of Binder Jet additive manufacturing on either the Moon or on Mars. Chapter 7 is on shrinkage prediction methods for metallic additive manufacturing methods. Conclusions are provided at the end of each chapters and pertain to the content in that specific chapter.

1.4 List of Publications

This research resulted in the following peer-reviewed publications:

- **Warren, Peter**, et al., Effect of sintering temperature on microstructure and mechanical properties of molded Martian and Lunar regolith, (Ceramics International) Volume 48, Issue 23, Part B, 1 December 2022, Pages 35825-35833.

- **Warren, Peter**, et al., Rapid defect detection and classification in images using convolutional neural networks, (Turbo Expo: Power for Land, Sea, and Air) Volume 84966, 2021.
- **Warren, Peter**, et al., Shrinkage Prediction Using Machine Learning for Additively Manufactured Ceramic and Metallic Components for Gas Turbine Applications, (Turbo Expo: Power for Land, Sea, and Air) Volume 85987, 2022.
- **Warren, Peter**, et al., Investigation of an advanced acoustic based nondestructive evaluation method, (Turbo Expo: Power for Land, Sea, and Air) Volume 58677, 2019.
- **Warren, Peter**, et al., Modeling Thermally Grown Oxides in Thermal Barrier Coatings Using Koch Fractal, (Turbo Expo: Power for Land, Sea, and Air) Volume 58677, 2019.
- **Warren, Peter**, et al., Investigating Load Transfer in Ceramic Reinforcements, (Turbo Expo: Power for Land, Sea, and Air) Volume 51128, 2018.
- Raju, Nandhini, **Warren, Peter**, et al., Sintering Behaviour of 3d Printed 17-4PH Stainless Steel, (Turbo Expo: Power for Land, Sea, and Air) Volume 86052, 2022.
- Raju, Nandhini, **Warren, Peter**, et al., Material properties of 17-4ph stainless steel fabricated by atomic diffusion additive manufacturing (adam), (2021 International Solid Freeform Fabrication Symposium) 2021.

CHAPTER 2: LITERATURE REVIEW

2.1 Additive Manufacturing

Additive manufacturing has developed quite rapidly over the past few decades. Although it is now possible to print metallic and ceramic components, polymers are still the most commonly printed material. This is due to the simplicity of the printing process. FDM (Fused Deposition Method) is the most common 3D printing method for polymer material, but there are now many new and innovative techniques for 3D printing plastic polymer material. Some of the more common 3D printed techniques for PLA (Polyactic Acid) include: FDM (Fused Deposition Method), SLA (Stereolithography), DLP (Digital Light Processing), SLS (Selective Laser Sintering), MJ (Material Jetting), and DD (Drop on Demand). PLA and other polymers have become quite lucrative to print in a timely manner. Metal has proven to be a much more challenging material to 3D print. Metal has a much higher melting temperature. Also Metal can be toxic to humans while in a fine powder form. Metal 3D printing also has a variety of techniques to use, but they are much more complex than the methods used for polymer printing [3, 4, 5, 6].

2.1.1 Metallic Additive Manufacturing

There are many types of 3D printing for metallic materials, and even more when other materials are included. It is difficult to organize them in a chart or graphic that paints a clear picture of the current state of the additive manufacturing industry. A good way to organize the various types of AM techniques would be to split them up into four categories: Liquid, Filament, Powder, and Solid [15]. The label is indicative of the state that the material is in prior to printing. The categories can then be further broken down into subgroups, this is illustrated in Figure 2.1.

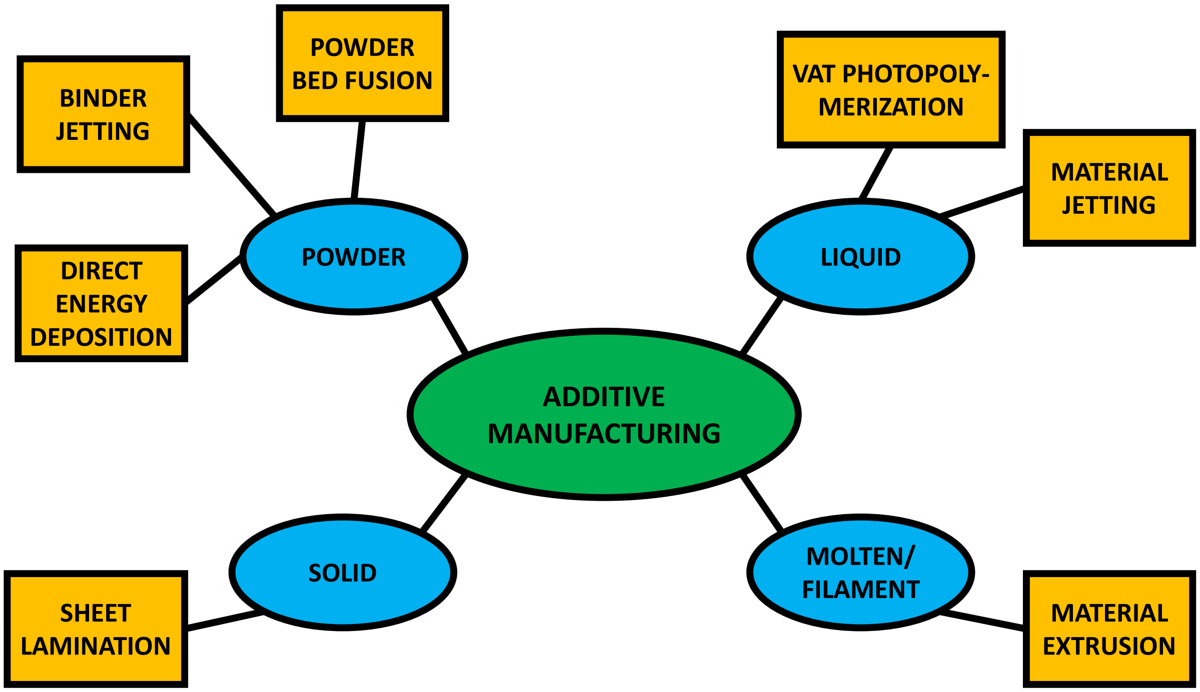

Figure 2.1: Categories of additive manufacturing methods organized based upon the starting state of the printable material. [16]

The first type of Metal 3D printing that is examined is metal binder jet printing. In metal binder jetting, the first step is completed when a liquid binder is dripped onto a bed of fine metallic powder. This binder will cause the particles to adhere to one another. The powder bed is lowered and another layer of binder liquid is applied to the powder bed. The part will be constructed and will slowly be submerged deeper and deeper into the powder bed as it is built. After printing is completed, the excess powder can be removed and only the part will remain. Now the part is simply metal particles with a liquid binder holding them together. The part will now need to be cured at around 150 °C to 200 °C. This process can take several hours. Finally the part will need to be sintered to remove the rest of the binder and fuse the metal particles together. The temperature needs to be raised to just below the metal temperature to slightly liquify the particles, and the pressure from the oven will fuse the particles together[17, 18, 19]. The part will shrink by around

Table 2.1: Additive Manufacturing Process and Material Table

AM Starting State	AM Process/Acronym	Material Capability
Liquid	(SLA) Stereolithography	Polymer
Liquid	(MJM) Multi-Jet Modeling	Polymer
Liquid	(LTP) Liquid Thermal Polymerization	Polymer
Molten/Filament	(FDM) Fused Deposition Method	Polymer
Powder	(LBPF) Laser Powder Bed Fusion	Metallic, Ceramic
Powder	(SLS) Selective Laser Sintering	Polymer, Metallic, Ceramic
Powder	(SLM) Selective Laser Melting	Polymer, Metallic, Ceramic
Powder	(EBM) Electron Beam Melting	Polymer, Metallic, Ceramic
Powder	(BJT) Binder Jetting	Polymer, Metallic, Ceramic
Powder	(DED) Direct Energy Deposition	Polymer, Metallic, Ceramic
Solid	(LOM) Laminated Object Manufacturing	Metallic, Ceramic

10-20%. The shrinkage is not always uniform and this is the area of prediction the AI could assist. An optimization of the complex sintering process, will ultimately lead to an optimization of the final material properties.

2.1.2 Fused Deposition Method

Fused Deposition Modeling (FDM), is a type of additive manufacturing technology that exploits the melting point of thermoplastic material. A filament of the thermoplastic material is heated and extruded through a small nozzle. The filament is extruded layer by layer to build up the final printed design. FDM technology was first patented by S. Scott Crump at Stratasys, Inc. in 1989. The first commercial FDM machine, the 3D Modeler, was released by Stratasys in 1992. In the more recent past, FDM technology has seen significant growth and there are a wide number of printers available from many different companies. It is the most popular form of additive manufacturing. This technology has seen many application in various industries for the rapid prototyping and manufacturing of a wide range of products. A few examples are aerospace components, medical devices, and consumer products [20, 21, 22].

Recently, machine learning (ML) has been applied to the FDM process to improve the quality of the printed parts and to automate certain aspects of the process. Some crucial examples of the application of ML to FDM is predictive modeling, automated support generation, real-time monitoring, adaptive slicing, and failure prediction [23, 24, 25].

Predictive modeling: ML can be used used to predict the properties of the printed parts, such as strength, flexibility, and dimensional accuracy. This allows for the optimization of the printing process and the selection of the appropriate materials.

Automated support generation: ML algorithms are used to automatically generate support structures for the printed parts, which helps to improve the quality and reliability of the printed parts.

Real-time monitoring: ML algorithms are used to monitor the printing process in real-time, which allows for the detection and correction of errors before they become a problem.

Adaptive slicing: Instead of using pre-determined slicing algorithms, ML algorithms are used to adapt the slicing process for each print job in order to optimize the print quality and reduce material waste.

Failure prediction: ML algorithms can be trained to predict when a printer is likely to fail, allowing for proactive maintenance and reducing downtime.

These are some of the current applications of machine learning to FDM printing, the field is still evolving and new application may arise in the future.

2.1.3 Laser Powder Bed Fusion

Laser Powder Bed Fusion (LPBF) is a type of additive manufacturing (AM) technology that uses a laser to selectively melt and fuse small particles of metal or polymer powder together to create a solid object. The process is similar and somtime used interchangeably with Directed Energy Deposition (DED) or Selective Laser Melting (SLM). The history of LPBF can be traced back to the 1980s, when researchers at the Fraunhofer Institute in Germany first began exploring the use of lasers to melt and fuse metal powders. In the 1990s, researchers at the Lawrence Livermore National Laboratory in the United States developed the first LPBF machine for the production of metal parts [26, 27].

In the early 2000s, companies such as EOS, Concept Laser, and SLM Solutions began commercially producing LPBF machines for industrial use. The technology quickly gained popularity in the aerospace and medical industries for the production of complex and high-performance parts. Over the years, LPBF technology has evolved and improved significantly, with new materials and improved process parameters. Today, LPBF is considered one of the most promising AM technologies for the production of high-performance metal parts, with a wide range of applications in aerospace, automotive, medical, and many other industries. The field of Laser powder bed Fusion is still evolving, with new materials and printing methods being developed, and the technology is seeing more and more adoption in various industries [28, 29].

2.1.4 Binder Jetting

Binder jetting is a type of additive manufacturing (AM) technology that uses a print head to selectively deposit a liquid binder onto a bed of powder material. The binder cures and binds the powder particles together. Next, another layer of powder is spread over the current layer, and the process is repeated. In the end the solid component can be removed carefully from the powder bed, and then proceed to sintering. Binder jetting technology has the advantage of being able to print with a wide range of materials, such as metals, ceramics, and polymers. It can also print with a variety of different powders, such as sand, gypsum, and metals. If the binder can adhere a powder together, than the technology can be implemented, making this technology very versatile. Binder jetting is being used for functional prototypes and end-use parts in a variety of industries, such as aerospace, automotive, and construction [30, 31, 32].

Binder jetting was developed in the late 1980s and early 1990s, by researchers at the Massachusetts Institute of Technology [33, 34, 35, 36]. It wasn't until the early 2000s that the first commercial binder jetting machines were developed and released by companies such as Z Corporation and Objet Geometries. In recent years, Binder jetting technology has improved with the development of multi-material printing, full-color printing and high-resolution printing. This technology shows a lot of adaptability and promise [37, 38].

2.2 Sintering

2.2.1 History of Sintering

Sintering is a process of compacting and forming a solid mass of material from smaller particles by heating to near melting temperature for a given time. At this near melting temperature, the particles will merge together. This process has been used for thousands of years for producing ceramics and metallic materials. The use of sintering for producing better materials is widespread across many ancient civilizations [39, 40]. The sintering capabilities of a given civilization can be used to quantify how advanced, a given civilization was. Historians have referred to different time periods, as the stone age, the bronze age, the iron age, and so on [41]. This sintering capability and knowledge of the behavior of the material at higher temperatures is a contributing factor to the "age" that a civilization would be in.

In ancient China, sintering was implemented for producing ceramics as early as the Neolithic period (around 10000 BC) [42]. All throughout Europe, evidence of sintering for iron objects for a myriad of purposes, has been discovered as far back as 1200 BC [43]. The Hittites, who lived in Anatolia (modern-day Turkey) from around 1600 BC to 1180 BC, are known to have used sintering to produce iron, bronze, and silver objects [44]. Sintering was even performed by the ancient Egyptians for producing various ceramics for pottery and other purposes [45]. Sintering was widely used, in many ancient civilizations for producing both ceramic and metallic objects. The development of sintering and the development of materials can be directly related to the advancement of civilization.

2.2.2 Sintering Quantification

The quantification of sintering can be a difficult process. Sintering is often performed at high temperatures, making it difficult to get measurements in situ. Some of the properties that can be measured to help quantify the amount or quality of sintering are: density, appearance, size, or mechanical strength [46].

Typically and often ideally the density will increase after sintering has been performed. Density measurements can be obtained through the Archimedes method, X-ray diffraction, CT scanning, or gas pycnometry. The appearance of a material will also change during sintering [47].

An examination of the microstructure of a given material can be used to provide insights into the extent a material has been sintered. A microstructural analysis could be completed with an optical microscope, a scanning electron microscopy (SEM) or transmission electron microscopy (TEM).

With a clear image of the microstructure it is possible to quanify porosity, grain size, grain shape, and grain boundaries. These properties can be very useful in the quantification of sintering [48].

In general materials are expected to shrink after the sintering has been completed. They may expand during sintering due to thermal expansion, but once could the object should be smaller than it was prior to sintering. Simple dimensional measurements can taken before and after sintering to record the amount of shrinkage that has occured. If shrinkage during sintering is desired, dilatometry is needed. A dilatometer is a simple device that will measure the linear shrinkage over time during the sintering process [49].

More optimal material properties are often another benefit or goal of sintering. Higher tensile and compressive strength are typically found after sintering. A material property that changes during sintering can be used to quantify the sintering as well. Material strength, thermal conductivity, modulus of elasticity, hardness are all good examples of a material property that could potentially be used to help quantify a given sintering process.

The input conditions for sintering can also be used to quantify sintering. Input conditions can include sintering temperature, duration, and environment. Ideally both input and output properties and variables are necessary to have a good model of a sintering behavior for a given material.

2.2.3 Sintering Models and Theory

There are several models for sintering that have been developed to describe and predict the behavior of materials during the sintering process. Some of the more common models include: Diffusion-controlled sintering models, neck-growth models, and kinetic models.

A diffusion-controlled sintering model describes the sintering process as a diffusion-controlled process where particles move towards each other and form a compact structure. The Johnson-

Mehl-Avrami (JJMA) model is an example of a diffusion-controlled sintering model [50, 51].

Neck-growth models are a geometric model of the material. These models describe the sintering process as the growth of necks or bridges between particles, which eventually form a compact structure. These models will typically model the interaction between particles using a combination of surface energy and strain energy associated with the inter-particle contact [40].

A kinetic model for sintering describes the rate of sintering as a function of time, temperature, and other parameters. These models often use the Arrhenius equation to predict the rate of sintering based on the activation energy required for sintering to occur and the effect of temperature on that activation energy. Other factors can be used in these models, such as the particle size distribution, porosity, and surface area of the starting powder material. Input conditions such as rate of heating, cooling, and sintering environment are also used frequently in kinetic models [52, 53, 54].

Accurate sintering models are difficult to formulate, but they are also necessary to predict the evolution of the microstructure and properties of a sintered material as a function of time and temperature. They are also necessary in order to optimize the sintering conditions to achieve desired final shape and material properties for a given object or material.

2.3 Machine Learning

2.3.1 Introduction

Machine Learning (ML) is a subset of Artificial Intelligence (AI) that focuses on the development of algorithms and statistical models that enable computers to learn from data and make predictions or detect patterns without being explicitly programmed to do so. The foundation of ML was developed in the 1950s and 60s, but it wasn't until significant advances were made in computational power in the late 90s and early 00s that the field was able to show it's true potential. With better computational power, ML algorithms and techniques were better developed and implemented in more inventive ways. Currently ML is being implemented in several different fields for many applications.

Some of the more common tasks performed by ML include: classification, regression, clustering, and anomaly detection. Classification is the process of sorting data into different categories, such as determining whether an email is spam or not. Another example is classifying a pixel on a given image to a certain object. Regression is a technique that relates a dependent variable to one or more independent variables. An example would be to predict a continuous value over time, like the density of a material during sintering or stock price over time. Clustering is the process of grouping data together based on the properties of the items of interest. Anomaly detection is the process of detecting outliers in a dataset. These are just a few examples of the many applications of ML. The field has received a tremendous amount of attention recently and is constantly evolving and new applications are being discovered and deployed regularly.

2.3.2 Linear Regression

Linear regression is a statistical modeling technique that quantifies the relationship between a dependent variable and one or more independent variables. It is used to make predictions about a continuous outcome based on the values of the independent variable(s). The first step in performing linear regression is to collect and prepare the data. A determination of the dependent and independent variables is necessary to choose the correct model for the data. Two common models are single variable and multiple variable. With multiple independent variables, the weight of each parameter should also be analyzed and estimated. Independent variables can be weighed via coefficients.

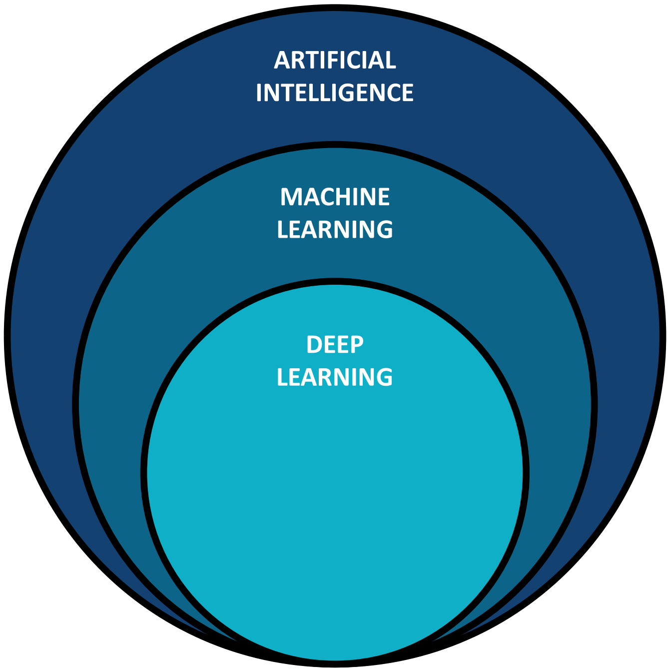

Artificial Intelligence (AI) – Intelligence that is demonstrated via computers of machines rather than humans. Intelligence can be demonstrated through perception, communication, creation, hypothesizing, organizing information, or dispensing information.

Machine Learning (ML) – ML is a subset of AI. ML is the implementation of statistical models or mathematical algorithms to enable a system to learn and adapt from data

Deep Learning – Deep learning is a subset of machine learning. Deep learning uses multiple layers in a single model or network to extract patterns from a set of data. A common example is the neural network.

Figure 2.2: A graphical layout of the fields Artificial Intelligence (AI), Machine Learning (ML), and Deep Learning. Definitions are provided for each of the terms on the right side of the figure.

Ordinary least squares, which is the most commonly used method, can be used to determine the intercept and also be used to determine the independent variable coefficients as well. Next the fit of the curve can be assessed. The model fit is evaluated by assessing the fit of the model to the data. A common method of accuracy quantification is the R-squared value. The R-squared value measures the proportion of variation in the dependent variable that is modeled by the independent variables. Once a model is determined to be adequate, it can be used to make future predictions. Linear regression is a widely used statistical method that and is the most simple to implement. Although the method is simple it still is used frequently in several fields. It is often a good first choice to use when analyzing a new set of data and trying to determine key insights on how to proceed forward.

2.3.3 Neural Network

The origin of neurons withing neural networks can be traced back to the work of Warren McCulloch and Walter Pitts in 1943 [55]. They proposed a model of a simple artificial neuron, which they called the McCulloch-Pitts neuron, and showed how such neurons could be combined to form a network that could perform simple computations. Many people currently refer to these neurons as an accurate representation of the neurons in the human brain, which could be true, but as of now there is no evidence of this. We have little knowledge of what governs the behavior of the neurons in our brains, and it would be hard to imagine that each nueron in our head behaves according to EQ. 2.1.

$$F(z) = F(b + \sum_{n=1}^{n} x_i w_i) \tag{2.1}$$

The pratical development and implementation of the neural network models occured in the late 1950s and early 1960s. Frank Rosenblatt introduced the concept of the perceptron, a simple type of neural network in 1958 [56]. Deep learning saw very small increments over the next few decades. A big breakthrough occurred when Yann LeCun developed the first successful deep learning model for handwritten digit recognition using Neural Networks in the late 1980s. This small simple task, displayed the power of deep learning in an elegant and intuitive way [57].

A neural network is a type of deep learning model that utilizes the layer by layer structure of the model to extract features from the data from different scales. The applications of neural networks can be classification and segmentation of images. Neural networks can also be used for natural language processing as well. They can even be implemented to perform regression, this would simply just be a more complex method to perform linear regression, the same method explained in the previous section. Neural networks just have the added benefit of being redesigned to allow for the input of data in a variety of different forms. A image is simply an array of numerical values which just happens to be a good input format for a neural network.

Neural networks have proven to be a powerful tool for machine learning and have been used in many successful applications. However, like all machine learning models, they must be implemented correctly. The choice of model architecture, training algorithm, loss function, and many other hyperparameters will determine the success of failure of a neural networks ability to perform a given task.These values can vary based on the specifics of the problem.

2.3.4 Convolutional Neural Network

Yann LeCun, should be credited with developing the first successful implementation of the Convolutional Neural Network (CNN) when he used it for deciphering handwritten digits [57]. Larger and more substantial improvements to the CNNs were able to be made in the mid-2010s. These improvements were possible due to the availability of large amounts of data and computational resources This led to the widespread use of CNNs in various computer vision and machine learning tasks, and it has since become the most popular deep learning model [58, 59, 60].

A convolutional neural network (CNN) is a type of deep neural network designed to process data with grid-like data structure, such as an image. An image is simply an array of numerical values for the pixels. CNN uses convolutional layers with filters that scan the input and apply different weights to the local regions. This is what makes them different from standard neural networks. The resulting feature map from a CNN is then processed using a combination pooling and convolution through the fully connected layers, which eventually produce the final output of the CNN.

The main difference between a CNN and a traditional neural network is that a CNN is specifically designed for image or audio data formats. A standard neural network is more general and can be applied to various types of data. CNNs work by applying filters to the input data to extract local features, and then using these features to make predictions.

The main components of a CNN are the convolutional layers, the pooling layers, the fully connected layers, and the output layers. A convolutional layer is where filters are applied to extract local features. This filter (or kernel) slides over the input image, performing element-wise multiplications with the elements in the image, and then producing a transformed output, which is also a matrix of values. The pooling layers typically come after the convolutional layers. The pooling layers reduce the spatial dimension of the feature map. This helps to reduce the computational cost of the network, as well as make the features more robust to small translations in the input data. After a few iterations of convolutional and pooling layers the fully connected layers are used. These layers are the same layer architecture found in a standard neural network. The final output comes from the output layer. This comes after all the convolutional, pooling, and fully connected layers. The output layer is in the desired format of the output prediction, whether that is highlighted pixels or class labels. The output is usually performed by a softmax activation function, which converts the predictions into a probability distribution over the possible classes.

CNNs work by extracting local features from the input data using convolutional layers, reducing the spatial dimensions of the feature map using pooling layers, and finally making predictions using fully connected layers.CNNs are widely used for a variety of computer vision tasks, such as image classification, object detection, and semantic segmentation. They are also used for speech recognition, natural language processing, and other applications where grid-like data is processed.

2.3.5 Generative Adversarial Neural Network

Generative Adversarial Networks (GANs) were first introduced in 2014 by Ian Goodfellow and colleagues at the University of Montreal. The paper "Generative Adversarial Nets" was published in the Conference on Neural Information Processing Systems (NIPS) and introduced the concept of using a competition between two neural networks to generate new data samples [61, 62, 63]. GANs have recently become a widely researched area in the field of deep learning and have been applied to a wide range of tasks. The basic idea of adversarial training has proven to be a powerful technique for generating new data, and GANs continue to be a popular and active area of research.

A Generative Adversarial Network (GAN) is a type of deep learning model that is used to generate new data samples that are similar to an existing dataset. It consists of two parts: a generator and a discriminator. The generator's goal is to create new data samples that are as similar as possible to the existing dataset, while the discriminator's goal is to distinguish between the generated data samples and the real data samples from the existing dataset.

The two parts of the GAN are trained simultaneously, with the generator trying to produce samples that fool the discriminator into thinking they are real, and the discriminator trying to correctly identify whether a sample is real or generated. Over time, the generator becomes better at producing realistic data samples, and the discriminator becomes better at detecting them. GANs have seen success in a wide range of applications, including image generation, video synthesis, text generation, and more. They have the ability to generate highly diverse and realistic outputs, making them a powerful tool in areas such as computer vision and natural language processing.

CHAPTER 3: MACHINE LEARNING FOR DEFECT DETECTION

3.1 Introduction

The manufacturing of various parts for turbomachinery operations is a very delicate and detail oriented process. The application of heat, hard machining, cutting, and other processes have many variables that can have a direct and drastic effect on the product which is manufactured. There are many forms of non destructive evaluation (NDE) that help engineers to determine part viability and quality prior to certifying a part for operation[7, 8, 1, 2]. Some of the more commonly implemented NDE techniques include: eddy-current, magnetic-particle, liquid penetrate, radiography, ultrasonics, and visual[9]. All of these techniques produce a significant amount of data and the processing and analyzing of this data can often be both time-consuming and inefficient for humans to perform. Artificial intelligence can either take over completely or play an assistance role in the processing of the massive amounts of data that is produced through NDE. Anytime the data produced is visual (either image or video) then CNNs can have a substantial effect on the processing efficiency of this data. There are a variety of new and innovative NDE methods that could benefit from the assistance of machine learning to process the data produced [64]. Neural networks are well equipped to process images, but can also be used to process ultrasonic data and eddy-current data[1, 10, 11]. The field of NDE is well suited for the application of neural networks, and will most likely be transformed by it.

In this work, a dataset composed of visual images of freshly manufactured sheet steel is examined. This image dataset was provided by a Russian steel manufacturing company known as Severstal. They supplied this data to the Kaggle community with a prize money of 120,000$ in 2019. Kaggle is a online data science community where many datasets are posted with certain modeling aspirations, and users often collaborate and compete to achieve those goals. The sheet steel surface images provided in this dataset are of both specimens with defects and without defects. The specimens with defects will have varying types and varying size of defects. The first goal for the CNN is to be able to determine if the sample has a defect, and if it does, then the second step is to determine what type of defect it has. This type of technology could be reconfigured and applied to several other manufacturing industries. It could also be applied to part inspection during operation. CNNs are well suited for image segmentation and classification. The next section will explain the Severstal Kaggle Competition requirements in further detail. There have been a few previous studies into this particular dataset which have experimented with various CNN architectures [65, 66, 67, 68].

The determination and classification of present defects in a product is a highly critical task to the manufacturing process and timeline. The rapid identification of defects in a finished product will also contribute to the determination of the cause of the defects. This will allow engineers to become much more efficient at manufacturing a defect free product in the future. An online database of the history of defects within manufactured parts can also serve as a reference during the determination of which areas of the manufacturing process will require further research and development in the future. CNNs are well equipped to provide the framework for rapid part inspection via images. In this work, only surface images will be analyzed, but in the future computed tomography (CT) images can also be examined. CT scans can show the internal details of a component and therefore internal defects can be found and analyzed. This type of work would be very beneficial to part manufacturing and operational equipment monitoring.

In this work, two specific CNN architectures will be implemented and trained on the Severstal steel dataset. Various accuracy metrics will be recorded during the training of the CNN architectures used on this dataset. This work will provide a benchmark for the performance of these two CNN architectures. The process of applying a CNN could be broken down into four basic steps. The first is a preliminary data analysis, the second is model selection (this should be done with some thought of the end goal for the data), the third step is to apply the model to the data, and step four is to analyse the results. It is common to iterate over steps three and four in order to obtain a good model. This paper will be broken down into sections with this process in mind. First there will be a dataset details section (step 1), then implementation (step 2), then a testing plan section (step 3), then a results section (step 4), and finally a conclusion section.

The CNN for this work is designed to both segment and classify images with an anomaly, which CNNs are quite capable of doing. Mechanical parts have not yet seen a significant amount attention from the artificial intelligence community. In recent years, CNNs have seen and are currently seeing a significant amount of research and attention in the medical imaging industries[69, 70]. They are mostly being used to find defects or ailments within the human body. The technology is highly transferable to mechanical parts.

In Figure 3.1, there is a very basic and simplified layout of how the neural network should operate for this specific task. The pictures on the right side are taken from a high frequency camera of the surface of newly manufactured sheet steel. Some of those images will have defects of various types, and some will not. The images will be fed through a fully trained model, which will determine if the images contain a defect and if they do, they will be annotated in a certain color to indicate which type of defect it possesses. There are examples of this in the right side of Figure 3.1. The middle is simplified representation of the architecture of a neural network.

This dataset is available for public viewing on Kaggle. The dataset could be broken down into 3 sections. There is a training set, a public testing set, and a private testing set. The training set is for training the model. The public testing set is for testing the model, and it is available for the public to see. The private set is a set of data that nobody, except for Kaggle has access too. The code is submitted, then Kaggle runs the private test set through it. Our models were scored on both the private and public test set. The scores are in the results section.

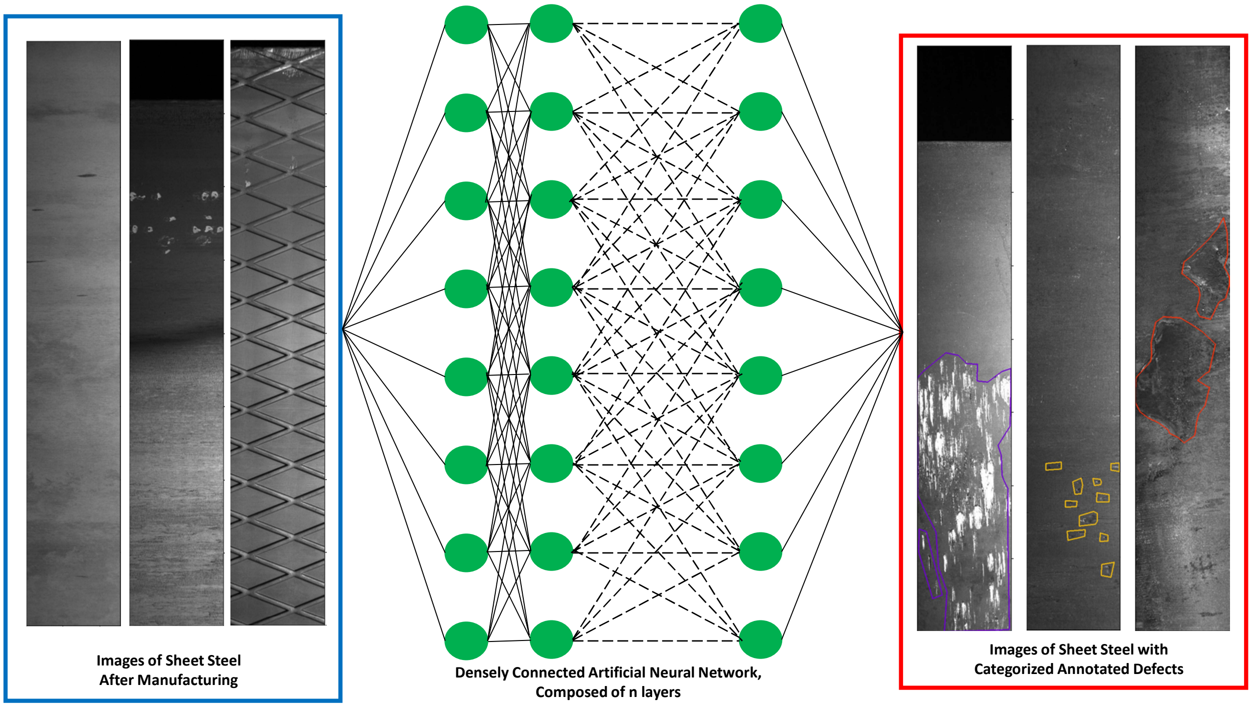

Figure 3.1: A visual representation of a convolutional neural network implemented for steel defect detection and categorization.

3.2 Dataset Details

As mentioned previously in the work, this dataset was published on Kaggle for a competition, and it is still currently available there [71]. There are an ample amount of notebooks, some of which are very well annotated, that are of great use and reference on Kaggle. This dataset is composed of images of sheet steel, which were gathered just after the steel was manufactured using a high-frequency camera. In the images there are several types of defects, so each image will either have no defects, have one class of defect, or have multiple classes of defects. The purpose of the competition is to be able to implement a CNN to not only detect if the steel has a defect, but also what type of defect is present within the specimen.

In order to evaluate performance the mean dice coefficient will be used as a metric. The dice coefficient can be used to determine if there is an agreement between predicted defect area and the ground truth. The formula in true statistical notation for the dice coefficient is given in Eq. 3.1. X is representative of the predicted pixel area and Y indicates the ground truth. X and Y are in the form of a 3rd order tensor. The dimensions are length and width in pixels, and the 3rd dimension is the value of the RGB (Red Green Blue) in the color scale. A high dice score indicates that the predicted areas of defect occurrence have a good match to the actual area of defect occurrence. The scale of the dice score is from 0 to 1, and a score of 1 would indicate perfect classification in the image at every pixel. There is an added complexity to the problem because it is not simply binary classification. The predicted area must also classify the defect into the correct type (1-4). The dice coefficient was used as a metric for the Kaggle Severstal steel dataset competition, so it will be calculated in this work as well.

$$Dice(X,Y) = \frac{2 * |X \cap Y|}{|X| + |Y|} \tag{3.1}$$

There is also another metric that is commonly used on pixel segmentation and classification tasks. This is called the intersection of union (IoU). The IoU and the dice coefficient are very similar. The formula for Dice coefficient is given in a different form in Eq. 3.2. This formula is given because it is easier to interpret. TP is true positives, FP is false positives, and FN is false negatives. TP is a group of pixels in the image that is representative in a defect that have been correctly predicted as a defect of the correct defect type. FP is a group of pixels that have been predicted as a defect, but are actually defect free or a defect of a different type. FN is an area predicted to be defect free, but actually contains a defect. True negatives are not included in the equation because the vast majority of the pixels in the images negative, so this would give an over inflated score. This is standard practice with image segmentation and classification. The formula for IoU is given in

Eq. 3.3. Both the IoU and Dice scores will be calculated in this work.

$$Dice = \frac{2TP}{2TP + FN + FP} \tag{3.2}$$

$$IoU = \frac{TP}{(TP + FP + FN)} \tag{3.3}$$

There is a stipulation on the submission format for this challenge. In order to reduce the size of the submission file the run length of encoded pixel values will be submitted. This means that only the first pixel and the length of the encoded area will be submitted. Pixels are numbered from left to right in rows and then top to bottom. Pixel 1 is in the top left corner and pixel 1601 would be one pixel below that. The images are 1600x256 pixels. A quick example of encoded pixel notation would be (12,4) which would cover pixels (12,13,14,15). The first number in (12,4) indicates the first pixel encoded, and the second indicates how many pixels following that pixel should be encoded.

When starting to analyze a dataset, it is important to examine the data carefully, prior to the implementation of a CNN. This initial examination helps to identify what could cause problems later during the training of the CNN. The first step of this initial examination is to look at some of the very basic statistics within the dataset, and then graph them. The competition stipulates that there are 4 distinct types of defects within the samples, unfortunately a specific category of defect (scratch, ablation, crack, etc.) was not provided by Severstal. The defects are only categorized by number(1,2,3,4). Upon examination it would appear that type 1 is small divots, type 2 is vertical cracks, type 3 is surface scratches, and type 4 is an ablation (this is a guess). In Figure 3.2, the composition of defects across the entire dataset is given. Defect type 3 is the most common type of defect to occur. Defect type 2 is very uncommon. In Figure 3.3, the amount defects in each image are given. It is about half with defects and half without, and there is a small group of images which possess multiple defects.

One of the more challenging aspects of this dataset is the image segmentation and classification. One issue with doing this is the way that the pixels have been encoded or marked. The entire surrounding area of a defect is marked as the defect. There are examples of this in the right side of Figure 3.1. The CNN is training to find the defect, and also grab some of the nearby area. This is because the training set images were annotated in this manner, the CNN will try to replicate it as best it can. It is a tedious job to mark the defects with more accuracy and precision, especially for such a massive dataset, so it is an understandable problem to have. Also the surface scratching is only counted as a defect if it is substantial enough. Minor surface scratching is sometimes not marked on some of the images. There are some images in the dataset, that are marked as having no defect, but they do have some minor surface scratches visible.

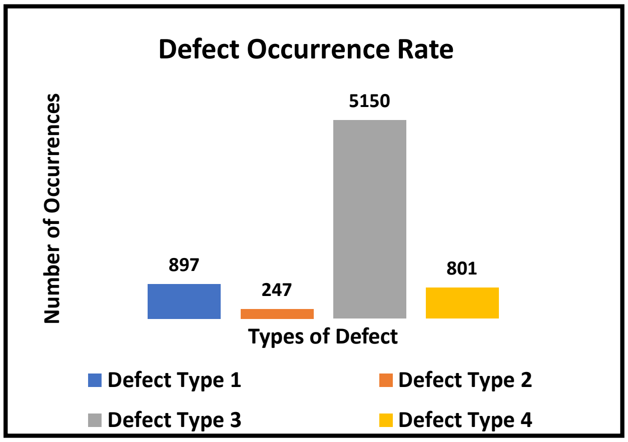

Figure 3.2: A bar graph of the number of specific defect types over the entire span of the training dat set of images.

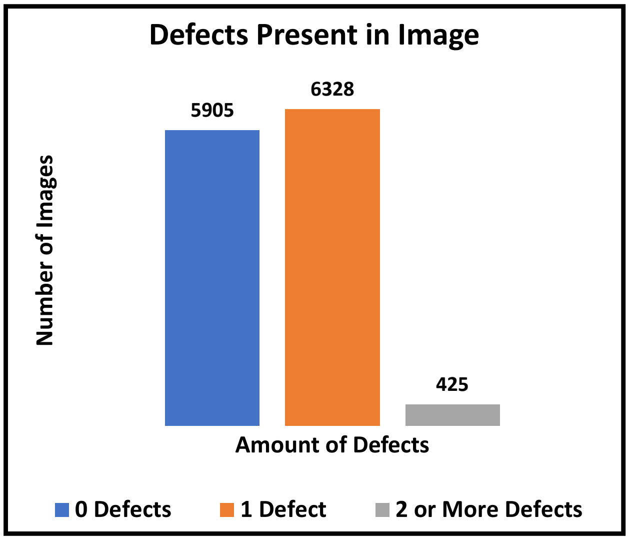

Figure 3.3: A bar graph of the number of defects of any type per image in this data set.

3.3 Implementation

The development of the Residual Network (Resnet) has enabled CNNs to be designed with hundreds of layers. Previous CNN architectures could have an infinite amount of layers, but the effectiveness of the CNN would drop off at a certain quantity of layers. CNN's with a Resnet architecture can have hundreds of layers and will see no drop off in the performance of the network. The Resnet was actually developed to solve the famous "vanishing gradient" problem during back propagation. So many layers in the CNN will cause the loss function to get a smaller and smaller, until it "vanishes."

The equation for a single neuron in a neural network is given in Eq 3.4. This equation is quite simple on it's own, but when compiled into a network of thousands of neurons it is difficult to solve without a computer. The w is the weight, b is the bias, the a^{l+1} indicates the neuron under consideration, and the a^l indicates the previous neuron. The σ is a nonlinear activation function. Usually a sigmoid function or a ReLu (rectified linear unit) are used for the nonlinear activation function for the neuron. As the neural network obtains more and more layers the weight function and the bias will drop off to zero. The later layers in the network do not improve the network. Resnet networks offer a solution partially skipping every other connection. This connection is shown in Figure 3.4. This "skipped connection" allows the network to learn the identity function into the deeper layers. Another way to think about it, is at the deeper levels of the neural network, the features that the network is learning are too abstract. The initial levels of the network focus on objects, edges, positions, and other lower level features of the image. The deeper levels become to abstract and irrelevant. This skipped connection layer or the residual block in the network has proven to be a good solution to this issue.

$$a^{l+1} = \sigma(w^{l+1}a^{1} + b^{1+1}) \tag{3.4}$$

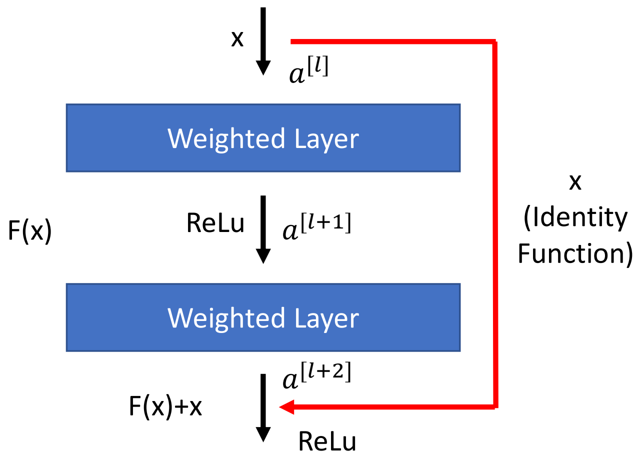

Figure 3.4: A basic residual building block diagram that makes up the resnet architecture. Relu is a rectified linear unit. This diagram details how the identity function passes through the layers of a given neural network.

The Resnet was implemented on the CIFAR-10 (Canadian Institute for Advanced Research) dataset and achieved first place in the ILSVRC 2015 classification competition (ImageNet Large Scale Visual Recognition Challenge). The CIFAR-10 dataset is a collection of images which are commonly used to train machine learning and neural network algorithms.The error rate that was achieved for that competition was 3.57%. This novel CNN architecture shook up the deep learning community and the Resnets have seen significant implementation and development over the past five years[72].

3.4 Testing Plan

For this work, two of the more common Resnet architectures are tested on the Severstal steel dataset. The two types of network layouts that we will be testing are the Resnet-18 and the Resnet-50. The batch size for the simulations was 2. The number of epochs for each architecture tested was 40. The batch size is how many images are processed per iteration, and the epochs are an entire cycle through all of the images in the training set. The learning rate was determined to be most effective at 0.0005, so that is what was implemented. This number indicates how far the weights will shift based on the feedback from gradient descent.

The loss function is a very critical part of implementing any type of machine learning. For this project a combination of a sigmoid layer and a binary cross-entropy (BCE) loss function was used to calculate loss. In python notation it is referred to as BCEwithLogitsLoss(). This loss function is well-suited and frequently implemented on datasets that require both image segmentation and classification. The BCE function can be seen Eq. 3.5. The y is a binary indicator and the p represents the probability that it belongs to either class. This function is combined with a sigmoid to determine how accurately the weights in the network are categorizing the pixels between iterations. The dice score cannot be used as a loss function because it is hard to differentiate it.

$$BCE_{LossFunction} = -\frac{1}{N}\sum_{i=1}^{N} y_i \cdot log(p(y_i)) + (1-y_i) \cdot log(1-p(y_i)) \tag{3.5}$$

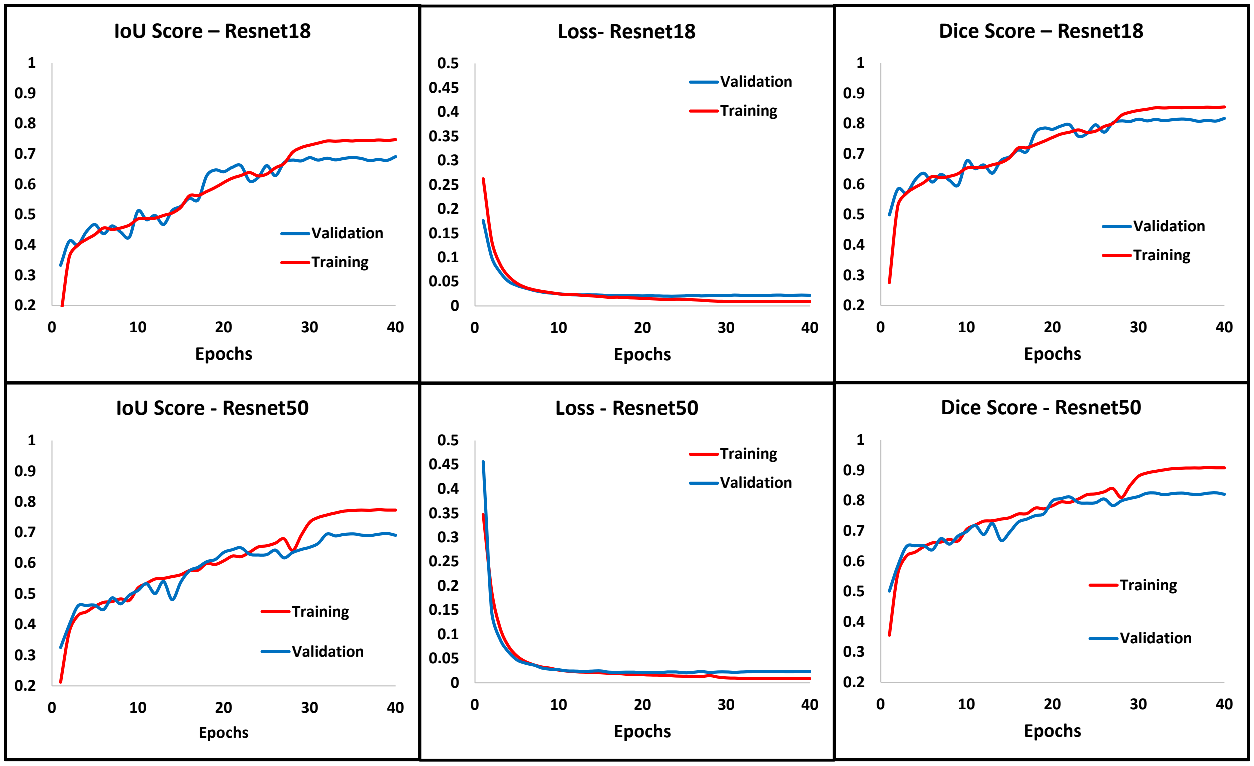

Figure 3.5: The results generated from the training of differing CNN architectures: (Top) The resnet-18 (Bottom) The resnet-50 (Left) Y-axis is the intersection of union score and X-axis is the number of epochs (Middle) Y-axis is the binary cross-entropy loss and X-axis is the number of epochs (Right) Y-axis is the dice score and X-axis is the number of epochs

The models used for this work were trained on Googles's AI platform on the cloud. The hardware used was 8 CPUs with 30GB of ram. The GPU was an Nvidia Tesla T4. The coding was completed with pytorch and several other common python packages under the GUI of jupyter notebook.

3.5 Results

As mentioned, two types of network architectures where used while training the model. They are the Resnet-18 and the Resnet-50. The results from training the networks are shown in Figure 3.5.

The results illustrate 3 critical factors which are the the IoU score, the loss, and the Dice score. All 3 of these factors have been plotted against the epochs. The IoU and the Dice scores are very similar, but both are plotted for reference for future works. A total of 40 epochs were run for the training. The training took about 10 minutes per epoch for the Resnet-18 and about 20 minutes per epoch for the Resnet-50. The final dice score for the Resnet-18 (the 40th Epoch) was 0.86 for the training set and 0.77 for the validation set. The final dice score for the Resnet-50 was 0.91 for the training set and 0.83 for the validation set. The final loss for the Resnet-18 was 0.85% for the training and 2.1% for the validation. The final loss for the Resnet-50 was 0.85% for the training and 2.3% for the validation.

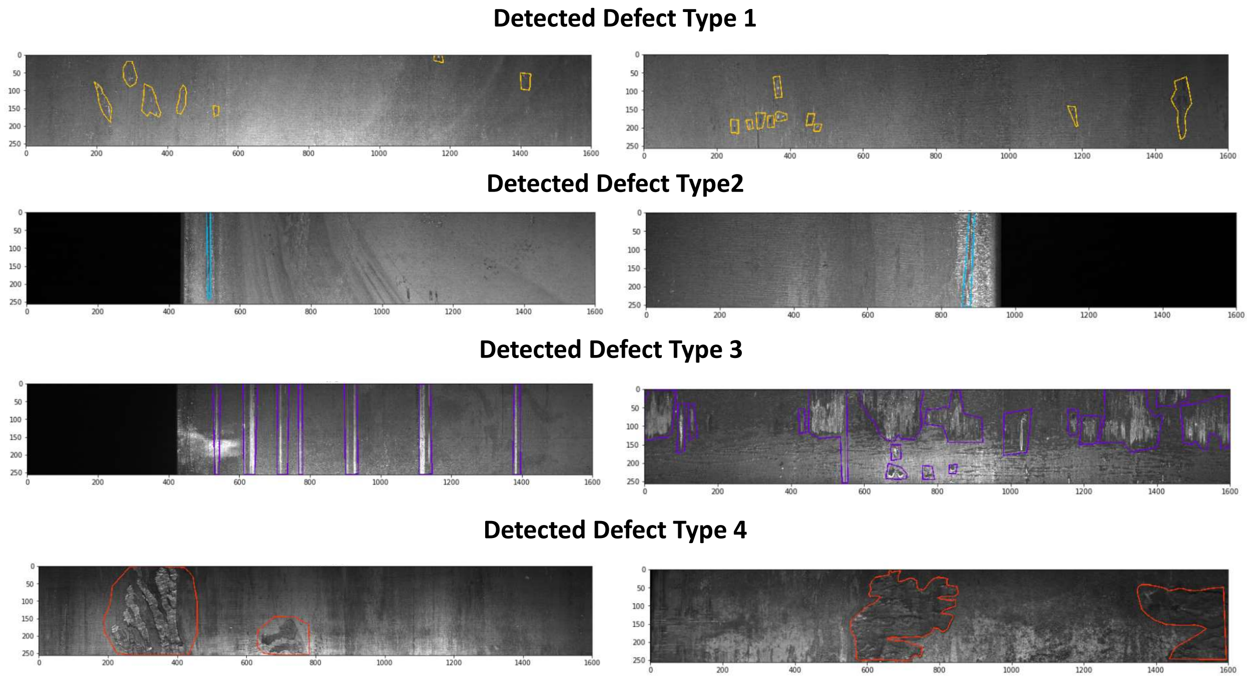

Detected Defect Type 1

Detected Defect Type2

Detected Defect Type 3

Detected Defect Type 4

Figure 3.6: Color coded defects for the resnet-50 CNN. Defect type 1 is yellow, defect type 2 is blue, defect type 3 is purple, and defect type 4 is red. Original images are from the test folder from the dataset.

This kernel was submitted under the stipulations of the contest, after the contest was over with.

One requirement is that the testing set images must be classified and segmented within one hour. The testing set images are a set of images that the CNN has never seen during training. There are about 1800 images in the public testing set. The code created for this work was able to do that, however the initial training of the model was done separately. The initial training took over an hour for both CNN architectures. Once trained though, both CNNs could analyze the 1800 images in the test set in about 10-20 minutes. The Resnet50 was submitted late for the competition and scored 0.86 on the public set, and 0.88 on the private set. The private set is a test set that Kaggle users do not have access to. The scoring is shown in tabular form in Table 2.1. The top scores are the top scores on the Kaggle competition. The Resnet18 and the Resnet50 are the scores acheived in this work.

Table 3.1: Dice Scores Comparison Table

Model	Public	Private
Top Score	0.92	0.91
Resnet18	0.85	0.87
Resnet50	0.86	0.88

The Resnet50 model performed quite well for being so straight forward, it placed in the top 1000 submissions for the public set and top 500 on the private set. The highest score on Kaggle are 0.91 on the private and 0.92 on the public, as indicated in Table 3.1. The way that kagglers often achieve these last couple decimal points is to run several models and perform a soft voting function. For this work we only examined the capability of the Resnet 18 and 50 on this dataset, in order to display more straight forward results that can be benchmarked.

In Figure 3.6 we can see some of the specific output files generated from this work. The defects are highlighted and color coded to correspond to what defect it is. This steel dataset is far superior to previous steel defect datasets in sample size, image quality, and defect diversity. Some noteworthy steel datasets include the one gathered by Northeastern University and the one gathered by Univeristy of Califonia Irvine [73, 74]. Currently there is not a substantial amount of manufactured part data from NDE methods available on Kaggle.

One interesting find in this paper is the area which the CNN finds as a defect. In Figure 3.6, we can see some images that are generated from running them through our CNN. We can see that the area around the defect is also marked as a defect. This is because of the way it was annotated. The area around defects was circled by whoever annotated the steel defects. The area in the test set was also annotated in this fashion. The neural network will try to annotate the images exactly like the human did for the training set. It is possible that by more accurately annotating the defects could lead to a higher Dice or IoU score. Essentially what these results say is that a CNN will do whatever it is trained to do. In this case it is trained to grab and oversized area of the defect region, so it grabs an oversized area of the defect. The fact that it can achieve such a high dice score with this quality of annotation is extremely impressive.

3.6 Conclusion

Our models in this work achieved an accuracy of 0.88 on the private and 0.86 on the public test sets for this competition. The results show that both of the Resnet architectures begin to overtrain at around 20 to 25 Epochs. This is clear from the slight divergence in the loss functions. The overtraining is very slight however (probably negligible), and the models still scored very well on the testing data set.

The data set here is highly beneficial to the data science and computer vision community. It demonstrates in a very clear fashion how powerful CNNs can be in this field. The annotation of defects is a little larger than the actual defect in all of the images. This could be an area of improvement in the future. It could be determined if a more accurate defect annotation area would increase the overall accuracy in the CNNs ability to detect and categorize defects. Also implementing CNNs on CT images could provide some very interesting results in defect detection efficiency.

It is very easy to see how this type of technology could be transformative to the manufacturing industry. The quantity and quality of data gathered from NDE industries continues to grow every year. Computer vision systems can provide instant feedback on the quality of the part that is being manufactured. It could also provide an excellent database of defects and help data scientists and product engineers to collaborate and improve product manufacturing procedures. There are thousands of parts that are manufactured for turbomachinery operation every year that could benefit from this technology. It is also a good idea to try to implement computer vision for part inspection during operation as well. This will lead to an increase in efficiency of operation. Artificial intelligence is very capable in assisting, improving, and rapidly analyzing data generated from many NDE techniques currently utilized for turbines inspections.

CHAPTER 4: MACHINE LEARNING FOR MICROSTRUCTURE ANALYSIS

4.1 Introduction

Grains are an observable unit in many materials, but are very useful for the examination of metallic materials. For metals, a grain is a region within the material that has a uniform, crystalline structure. Grains are often measured by slicing a sample and observing it with either a SEM (Scanning Electron Microscope) or a standard optical microscope. When grains are observed via a cross-sectional image, they tend to have an irregular polygonal shape. The grains are dependent upon the material and the processing method. For metals the three most common grains are Equiaxed, Columnar, and Lamellar [75, 76]. Equiaxed grains are roughly the same size in all directions, columnar grains tend to be elongated along on direction and lamellar grains are thin layers or sheets. It is difficult to get the full three dimensional story that a grain wants to tell, when we are only listening in two dimensions. It is difficult, but not impossible. There are many image processing techniques that can extrapolate more data from these images than was previously possible.

Grains play a crucial role in the structure of a material. For metallic materials, grain size and shape can have a significant effect on the mechanical properties. In general, metals with small, uniform grains are stronger and more ductile than those with large, irregular grains[77, 78, 79]. In addition to strength and ductility, the grain size and shape of a metal can also affect other properties, such as its electrical and thermal conductivity, corrosion resistance, and wear resistance [80, 81]. Understanding the grain size and shape of a metal is critical for optimizing its properties for specific applications. The role that grain size and shape play in material properties is still being researched and discovered. Advances in the way we study or analyze the microstructure of materials can directly contribute to a more thorough understanding of this crucial relationship grain size and shape to macro material properties.

Metallic components have traditionally been forged through casting, and then machining. Over the past two decades the ability to 3D print metals has become a reality, with more and more techniques becoming available. Metallic additive manufacturing is a process in which a three-dimensional object is created by adding layers of metal material one on top of the other. Additive manufacturing allows for the creation of complex shapes and geometries that would be difficult or impossible to produce using traditional methods. It also allows for the creation of objects with internal features and voids, such as channels and passages, these features can be very beneficial in turbomachinery components. For producing small batches or customized parts, 3D printing can be more efficient and cost-effective than traditional casting and machining methods. Alongside the benefits that these new 3D printing techniques provide, there are also many new challenges. The shrinkage that occurs during the sintering portions of manufacturing cycles is difficult to quantify, making final geometric and material properties more difficult to quantify[82, 83, 84, 85].

In this work we analyzed how grains are measured and how image processing techniques can be used to assist this process. We used both artifically generated grains and actual metallic grains seen under a microscope. The generated grains were made with a voronoi tessalation pattern, and then adding noise to the image in a variety of ways. The actual metallic grains are from optical microscope images of stainless steel 316L that was printed on a ExONE BJT printer. A large dataset of grains was created in this work, in order to implement a variety of machine learning techniques. The grains observed experimentally in this work, can be classified as equiaxed grains.

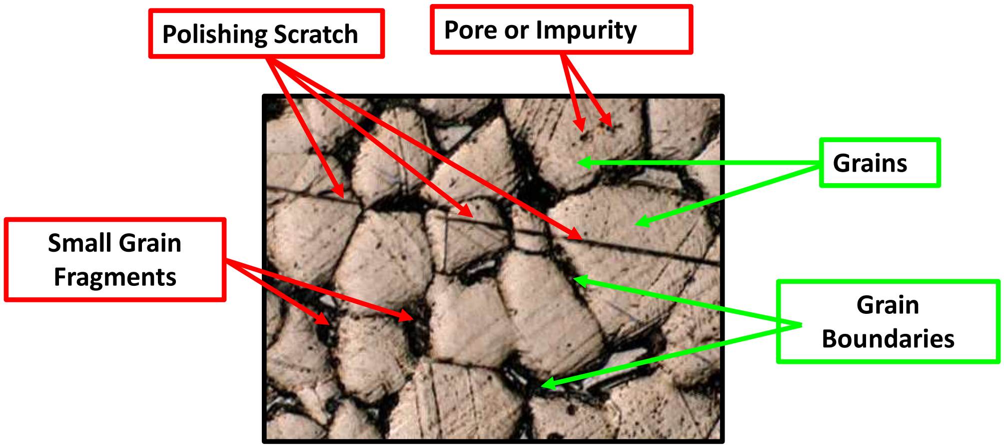

Figure 4.1: An example image of a metallic grain structure. This image shows some of the challenges that are present in a typical grain image, when trying to classify pixels into either grains or grain boundaries. These challenges include: polishing scratches, pores, impurities, and small grain fragments.

4.2 Image Segmentation Techniques

In order to take measurements of the grains, first images of the microstructure must be taken. This can be done with either an SEM or an optical microscope. After the images are taken they need to be segmented into two components: the grains and the grain boundary. The section of the paper will explain the four most common ways to segment an image into grains and grain boundary. The four ways are: (1) Manual Thresholding (2) Gradient Based Methods (3) Holistically Based Edge Detection (4) Manual Segmentation. In practice these methods can be combined in a variety of ways to segment and image. The (HED) Holistically Based Edge Detection method is an example of a neural network style approach. There are many new developing methods that use neural networks to detect edges of an image, HED is just the most well known and popular at the time of writing this paper. The HED method was developed specifically for detecting the edges of an image in any image.

4.2.1 Manual Thresholding

The coding for the manual thresholding was done using OpenCV [86]. All of the code for this work is available on github and kaggle [87]. A step by step approach to manual thresholding can be seen in Figure 4.2. The first image is one taken of 316L stainless steel printed on an EXone printer from an optical microscope at 500X. Step 2: Convert the image to black and white. Step 3: plot a histogram, the X-axis is pixel intensity and the Y-axis shows the number of times that pixel intensity has occured. The histogram is used to determine a good approach for threshold. Step 4a and step 4b are both examples of thresholding. Step 4a is an example of standard thresholding where all of the pixels ($>$130) are set to 255 (white) and all pixels ($\leq$130) are set to 0 (black). The value 130 is shown in red on the histogram. Step 4b is an example of an adaptive gaussian threshold. The threshold value is a gaussian-weighted sum of the neighbourhood values minus the constant C. The neighborhood values are a block of pixels, for this case it was (55x55), and the constant subtracted was 2.

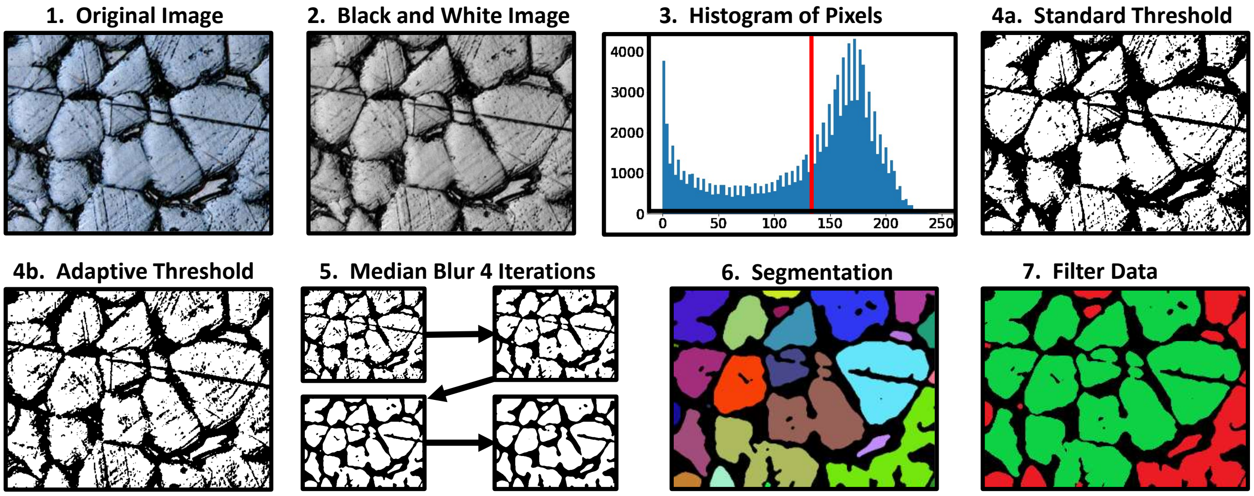
1. Original Image
2. Black and White Image
3. Histogram of Pixels
4a. Standard Threshold
4b. Adaptive Threshold
5. Median Blur 4 Iterations
6. Segmentation
7. Filter Data

Figure 4.2: A step by step example of the manual thresholding technique being applied to a metallic equiaxed grain boundary image.

In step 5 a median blur is applied 2 times to a 5x5 pixel area, and then 2 more times to a 7x7 pixel area. In step 6 image segmenation is applied, and the grains are seperated from the grain boundaries. In step 7 the grains are filtered, usable grains are shown in green and unusable grains are shown in red. Unusable grains are grains that are too small or grains that have too much perimeter per area. Too much perimeter per area indicates the grain did no get properly segmented during the total process. Essentially two or more grains are connected by a small "neck" region.

Image segmentation via threshold is a simple but highly customizable process. There are several steps in this process where the user has to select a value and check the results. For example, threshold cutoff, block size for blurring, block size for the adaptive gaussian method, etc. All of these values lead to different results, so the user must pick the one that looks the best in order to automate the grain segmentation process. Different materials, imaging equipment, or image settings can effect the images, and could easily require different variables for optimal segmentation.

4.2.2 Gradient Based Methods

Gradient based image segmentation is also possible to separate the grains from the grain boundaries. The gradient based approach will identify sharp changes in pixel intensity, and it will classify those areas as an edge. There are several mathematical tricks to determine the best way to detect this change in pixel intensity, many of which involve taking the first or second derivative. The method often considered to be the most robust is the "Canny Edge Detection Method," developed by John Canny [88]. The basic process is to first to convert the image to greyscale and then apply a Gaussian filter to smooth the image. The gaussian filter makes the image slightly more blurry. This reduces the amount of noise that will be detected in the process. Next the pixel intensity gradient is calculated (the first derivative of the image). Lower changes in pixel intensity can be filter out, unless they directly connected to a high change in pixel intensity.

The application of the Canny Edge Detector can be seen in Figure 4.3. First the image was converted to black and white. Next the Canny Edge Detector was used. In the third step, two Gaussian blur iterations were applied to a 3x3 pixel block. In the fourth step, the image is thresholded into 0 and 255 (black and white). The threshold value was very high (200), meaning most gray pixels were set to black. Step 5: segmentation occurs. Step 6: Filtering of the data occurs. The same filters were used as the previous section. Too much perimeter per area were filter out, and too little a grain size were also filter out.

Image segmentation via gradient detection is also a simple but highly customizable process. There are several steps different gradient based methods to choose from. Also the pre and post filter selected will lead to different results. Again the user must tailor the settings and parameters of the algorthm for specific materials or image settings.

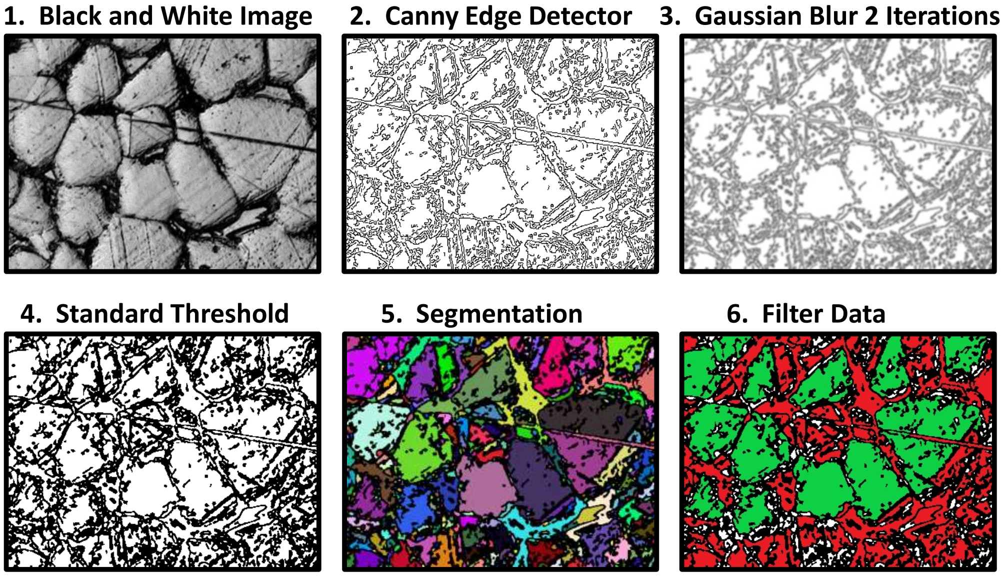

Figure 4.3: A step by step example of the gradient based technique being applied to a metallic equiaxed grain boundary image.

4.2.3 Holistically Nested Edge Detection

The next detection method involves machine learning and neural networks. The (HED) Holistically Based Edge Detection method is an example of a deep learning approach.[89] This method uses a (CNN) convolutional neural network architecture to classify the pixels of an image as an edge or not an edge. CNNs are particularly well-suited for tasks involving image processing and analysis, such as object detection, image classification, and image segmentation o2015introduction, albawi2017understanding, warren2021rapid. Essentially the CNN was just trained to detect edges and works quite well.

In Figure 4.4, there is a layout of using the HED approach. First the image is converted to black and white. Next it is fed into the HED model to determine the edges. The third step is to apply an adaptive guassian threshold to convert all pixels to either 0 or 255 (white or black). The final two steps are again segmentation and data filtration. The HED model works exceptionally well, and provides the user with a pixel intensity that represents the confidence that the pixel is an edge or not an edge. That is why step 3 (adaptive thresholding) is required.

So far the HED method seems to be the most effective, but there are some downfalls to it. The HED is a robust edge detector, and is not specifically trained to detect edges of grain boundaries, but is trained to detect edges of any possible image. It can be a airplane, an animal, or even the microstructure of an additively manufactured piece of stainless steel. If a network is trained specifically for grains and grain boundaries it would be able to outperform the HED method. Also the next section is manual (human) segmentation, which is currently the most accurate.

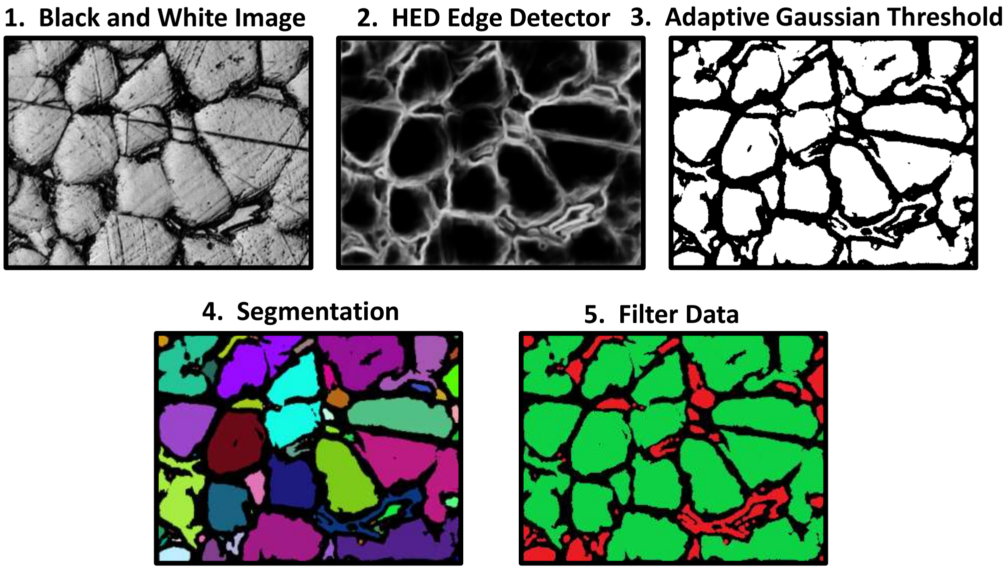

Figure 4.4: A step by step example of the (HED) Holistically Nested Edge Detection neural network technique being applied to a metallic equiaxed grain boundary image.

4.2.4 Manual Segmentation

The most arduous way to segment the grains of image is the manual segmentation. This is dont by the user manually annotating the grains or grain boundaries. For this work this was done by marking the grain boundaries in a specific color, and then thresholding the image so that all annotated pixels are 0 (black) and all others are 255 (white). After that the same process of segmenting the image computationally and filtering out small particles occurs. This process is shown in Figure 4.5. The process is very simple and straight forward. This method is the most accurate. The challenges of avoiding polishing scratches and pores is easy if the person annotating the image is careful. The only downfall to this method is that it cannot be automated. Each image requires human attention, for one image it may be worth while, but for many it may not.

For this work the authors did manually segment all 480 images of grains, and this was used for machine learning purposes that will be explained later. Also all of the previosly mentioned segmentation methods/algorthms were used (HED, Gradient, Threshold) on the dataset. All of this data is available on Github and Kaggle.

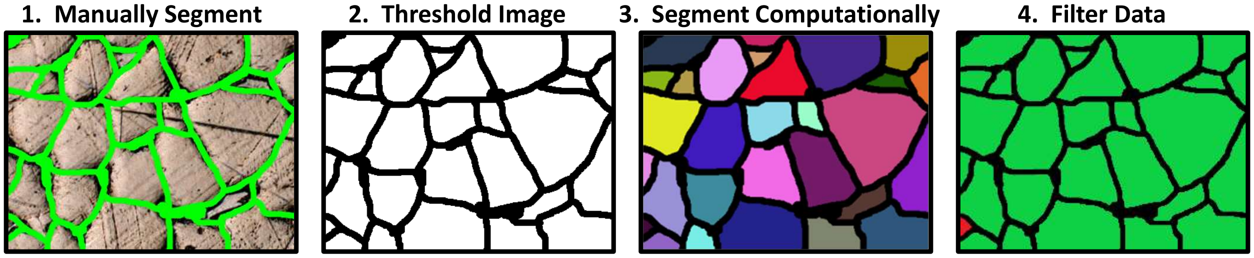

Figure 4.5: A step by step example of the manual segmentation being applied to a metallic equiaxed grain boundary image. This was done by hand, by a human.

4.3 Grain Measurement and Accuracy Quantification

There are a few ways to quantify how accurate the methods developed an implemented to segment images the grains from grain boundaries in this work. One method is to look at the actual grain data obtained. Traditional grain measurements techniques will be as a baseling to compare to. The two most popular traditional measurement techniques are line intercept (Heyn method) and the planimetric method (Saltykov method). These two methods will be explained in the following sections.

Another way to quantify accuracy is to compare the actual pixels being segmented and classified. The current standard is the dice score or the Intersection of Union (IoU) score. These two methods are frequently used to determine how accurate a neural network is at segmentation, and they will be explained in this section as well.

4.3.1 Line Intercept Method

As stated before, the grain boundary image dataset gathered for this work is 480 images, and each image is 400 x 300 pixels. The grain intercept method or line intercept method developed by Heyn, has long been the standard way to get quick grain size measurements [90]. It works by drawing a line through the image and counting the number of grains that the line is in contact with. The average grain size is then calculated by dividing the number of grains by the length of the line. The simple formula is shown in Equation 4.1. A simple code was written for to automate this process and perform the measurement at every pixel. This was completed for all of the segmentation techniques listed in section 2. That is a total of 144,000 X-direction measurements, and 192,000 Y-direction measurements. The average grain size and the standard deviation for both the horizontal and vertical direction is shown in Table 4.1. Although this grain intercept method can provide so many measurements, it still lacks in capability. It is a rough 1-D measurement of a complex 3-D structure. It is still used frequently today, so including is still relevant.

$$Grain\ Size = \frac{Number\ of\ Grains\ in\ Contact\ With\ Line}{Total\ Length\ of\ the\ Line} \tag{4.1}$$

Table 4.1: Line Intercept Grain Measurements

Direction	Manual Threshold	Gradient Method	HED Method	Manual Segmentation
X-Direction	41.45 ± 6.42	20.86 ± 10.90	33.05 ± 6.53	36.87 ± 4.84
Y-Direction	42.28 ± 7.59	22.64 ± 5.99	34.02 ± 6.80	37.40 ± 5.44

4.3.2 Planimetric Method

The planimetric method is a 2-D method, and can provide data on the size and shape of the grains. The more critical size and shape data that can be extracted from the segmented data was gathered. The data is divided into size data in Table 4.2, and the shape data in Table 4.3. The data is available for all for of the segmentation methods listed in section 2.

The planimetric size data includes four different measurements. The first is total grains, that is the entire amount of grains found in all of the images. This is just for a comparison point. The second is the individual grain area average. This is the average area of the grains plus or minus the standarad deviation. The third and fourth items in Table 4.2 are the total grain area per image and the total grain boundary area per image. These two values can be easily calculated from each other, as shown in equation 4.2.

$$Total\ Image\ Area = Total\ Grain\ Area + Total\ Grain\ Boundary\ Area \tag{4.2}$$

Table 4.2: Planimetric Size Measurements

Measurement	Manual Threshold	Gradient Method	HED Method	Manual Segmentation
Total Grains	9,575	24,740	15,297	11,002
Individual Grain Area Average	$844 \pm 1,314$ μm^2	248 ± 1033 μm^2	488 ± 823 μm^2	1068 ± 929 μm^2
Total Grain Area %	53.3%	40.5%	49.3%	77.5%
Total Grain Boundary Area %	46.7%	59.5%	50.7%	22.5%

The planimetric shape data includes five different measurements. Circularity is a simple geometric property of a shape that will be between 1 and 0, where 1 is a perfect circle and 0 is the opposite. The closer to 0 the more rough the 2-D shape is. The equation for circularity is show in equation 4.3. The average max diameter, this is maximum distance from one side of the grain to another that crosses through the centroid of the grain. The next 3 measurements are in the X and Y directions. The first is the average width of the grains, referred to as the average X-diameter. The next is the average diameter in the Y-direction or the average height. The final value is the aspect ratio, this is just width over height, or average x-diameter divided by average y-diameter.

$$Circularity = \frac{4\pi A}{P^2} \tag{4.3}$$

Table 4.3: Planimetric Shape Measurements

Measurement	Manual Threshold	Gradient Method	HED Method	Manual Segmentation
Circularity	0.55 ± 0.18	0.28 ± 0.15	0.50 ± 0.18	0.61 ± 0.12
Average Max Diameter	39.31 ± 30.69	25.14 ± 18.60	30.57 ± 22.84	47.38 ± 20.52
Average X-Diameter	32.18 ± 25.39	22.64 ± 15.90	24.81 ± 19.51	39.07 ± 18.49
Average Y-Diameter	32.94 ± 26.70	22.64 ± 15.40	25.47 ± 19.76	39.06 ± 18.97
Aspect Ratio X/Y	1.09 ± 0.55	1.06 ± 0.53	1.07 ± 0.51	1.11 ± 0.58

4.3.3 Evaluation of Segmentation

To evaluate the accuracy of the segmentation models, the dice score and the IoU score will be used. There are four ways to classify a pixel of an image that has been segmented. TP is true positives, FP is false positives, TN is true negatives and FN is false negatives. The dice equation is given in the form of these variables in equation 4.4. The probabilistic version of the equation is given in equation 4.5.

$$Dice = \frac{2TP}{2TP + FN + FP} \tag{4.4}$$

$$Dice(A,B) = \frac{2 * |A \cap B|}{|A| + |B|} \tag{4.5}$$

For this to be implemented a ground truth needs to be determined and indicated. The ground truth for this work will be the manually segmented images. The only error in these images is the error caused from a human while sketching the grain boundaries. The comparison of Dice and IoU scores for the manually thresholded method, the gradient method, and the HED method can be seen in Table 4.4. These scores can be used as bench marks along with the other specific grain properties to quatify the accuracy of the machine learning methods developed in this work.

Table 4.4: Planimetric Shape Measurements

Scoring Method	Manual Threshold	Gradient	HED
Dice	0.55 ± 0.18	0.28 ± 0.15	0.50 ± 0.18
IoU	39.31 ± 30.69	25.14 ± 18.60	30.57 ± 22.84

4.4 Artificially Generated Grains

Artificial grains and grain boundaries were generated using a voronoi tessalation pattern. This tessalation pattern has a very similar pattern to equiaxed grain boundaries. The noise found in the images of the grains for this work was also simulated using various noise generation methods.

4.4.1 Voronoi Tessellation

A Voronoi tessellation pattern is generated by partitioning a plane into regions based on distance to known points in the plane [91]. That set of points (also called seeds) have a corresponding region consisting of all area in the plane that is closer to that point than to any other. Once the cell is partioned into regions defined on proximity to a seed, the graph can be referred to as a Voronoi Diagram. An example of a Voronoi Diagram used for this work, can be seen in Figure 4.6. The size of the cells is based on the area measurements from the previous section. The average Voronoi cell area is approximately equal to the inverse of the point density. For example, if the point density is 10 points per unit area, the average cell area would be approximately 0.1 units. Based on this simple calculation the average grain (cell) area for this generated data is 1000 μm^2. This average individual grain area for the manually segmented images was 1068 μm^2, so 1000 μm^2 was selected for the generation to portray the actual data.

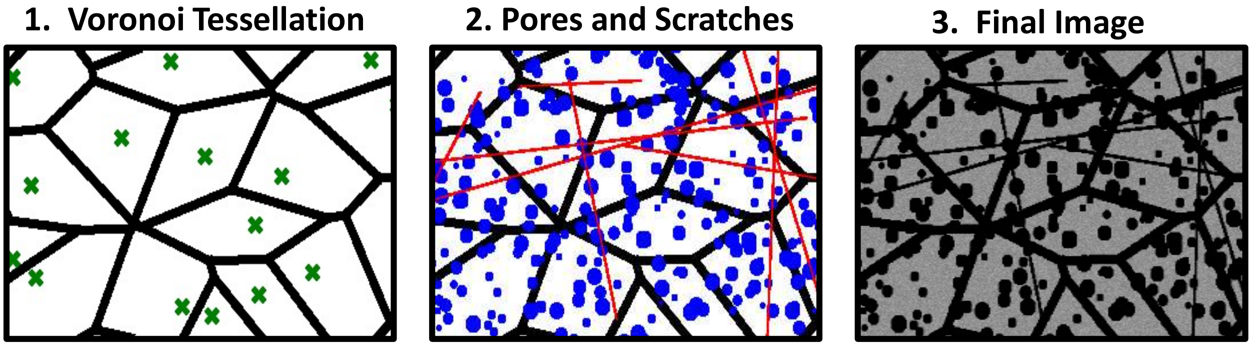

Figure 4.6: Artificial grain generation via Voronoi Tessalation pattern: (1) randomly generated voronoi tessalation pattern with centroids marked in green. (2) Polishing scratches marked in red and large and small pores marked in blue (3) Gaussian Noise applied to simulate the black and white grain color, this is also an example of a artificial grain generated through this method

4.4.2 Artificial Noise

The noise generated for the Voronoi Tessellation pattern was performed to mimic the actual challenges seen in the images. The two biggest challenges are polishing scratches and pores, as shown in Figure 4.1. Scratches were added by plotting random lines in the Voronoi graph, and pores were added by plotting random dots of random sizes. An example of the pores and scratches is shown in Figure 4.6. These defects could be eliminated from the data by more careful polishing and by a better etching method. Polishing and etching are complex processes that are difficult to perfect, so using machine learning methods to automatically ignore these defects is also a suitable path to eliminating the undesired effects these defects inflict during the measurement process.

The total plot area is from 0 to 800, but the actual image is from 200 to 600. This creates a 400x400 pixel image (the same as the experimental data). This also allow for the scratches to sometimes travel the entire sample image or just start and stop in the image. The amount of pores and scratches was varied when creating the artificial data, this will be explained in the next section.

4.4.3 Artificial Dataset

The amount of scratches in the total plot was a uniform random number between 2 and 10. The start and stop locations were also random (uniform random for both X and Y). The number of randomly sized pores was a uniform random number between 2000 and 4000. There was also random black pixels placed in the images, the amount was a uniform random number between 10000 and 20000. To give the grains the gray color all of the white pixels (255) had a number subtracted from them. The number was a normal Guassian distribution of 100 ± 10. All of the numerical values for the first round of noise distributions are given in Table 4.5. The goal is for a convolutional neural network (CNN) to be able to take a noisey Voronoi tessellation and predict the mask (the initial noiseless Voronoi Tessellation). A CNN easily be able to do this, so to make the model more robust more noise will be added.

Table 4.5: Applied Noise Distribution Table

Noise Type	Distribution/Application
Added Black Pixels	**U** $\sim$ (10,000, 20,000)
Added Black Dots	**U** $\sim$ (1,000, 2,000)
Dot Size (Radius)	**U** $\sim$ (5, 25)
Gaussian Noise Subtracted	**N** $\sim$ (100, 10)
Total Scratches	**U** $\sim$ (2, 10)
Scratch Start and End Point	**U** $\sim$ (0, 800)
Total Area Plotted	X and Y : (0, 800)
Area in Image (From Original Plot)	X and Y : (200, 600)

The next round of noise added to the artificial dataset was the inverse of two of the segmentation techniques listed Section 2. The two techniques are the Manual Thresholding and the Gradient Based Method. The deficiencies of the these image processing techniques can be exploited to further train and create a more robust CNN for image segmentation. The median blur technique seen in section 2.1 was implemented, as was the Gaussian blur technique seen in section 2.2. The inverse of an adaptive threshold is similar to an erosion technique, this was also used. These techniques were applied in varied iterations and also used in conjuction with each other. The application method can be seen in Table 4.6. The example of an original Voronoi tessalation with the full applied noise for each set in Table 4.6, can be seen in Figure 4.7.

4.5 Machine Learning Methods

The method for machine learning is a convolutional neural network (CNN) that will be used to identify whether a pixel is a grain or a grain boundary. The architecture will be a U-NET. The U-

Table 4.6: Image Distortion Applications Table

Set of 100 Images 256x256	Erosion and Dilation Kernel [3,3]	Gaussian Blur Kernel [15,15]	Median Blur Kernel [5,5]
1	YES	NO	YES (1 iteration)
2	YES	NO	YES (2 iteration)
3	YES	YES (1 iteration)	NO
4	YES	YES (2 iteration)	NO
5	NO	NO	YES (1 iteration)
6	NO	NO	YES (2 iteration)
7	NO	YES (1 iteration)	NO
8	NO	YES (2 iteration)	NO

Net used will be explained in the section U-NET. There were a few different methods of training that were used and that will be explained in the section training styles.

4.5.1 U-Net

The U-NET architecture was recently developed in 2015 [60]. The U-Nets architecture is well-suited for pixel segmentation because they are able to effectively capture both local and global features in the input image. Another beneficial feature is the use of skip connections, which allows the model to make use of both high-level and low-level features. In most image classification problems both level of features carry critical information, that is needed for classification. We are currently in a Artificial Intelligence growth period and there are many new spins on the classic U-NET model. Rather than try 20 different models to see which one performs the best, in this work we will use the standard U-NET as a benchmark. The selection of the best model can be performed easily, since all the data is public.

The activation functions in between the layers was the Relu function. The final activation function

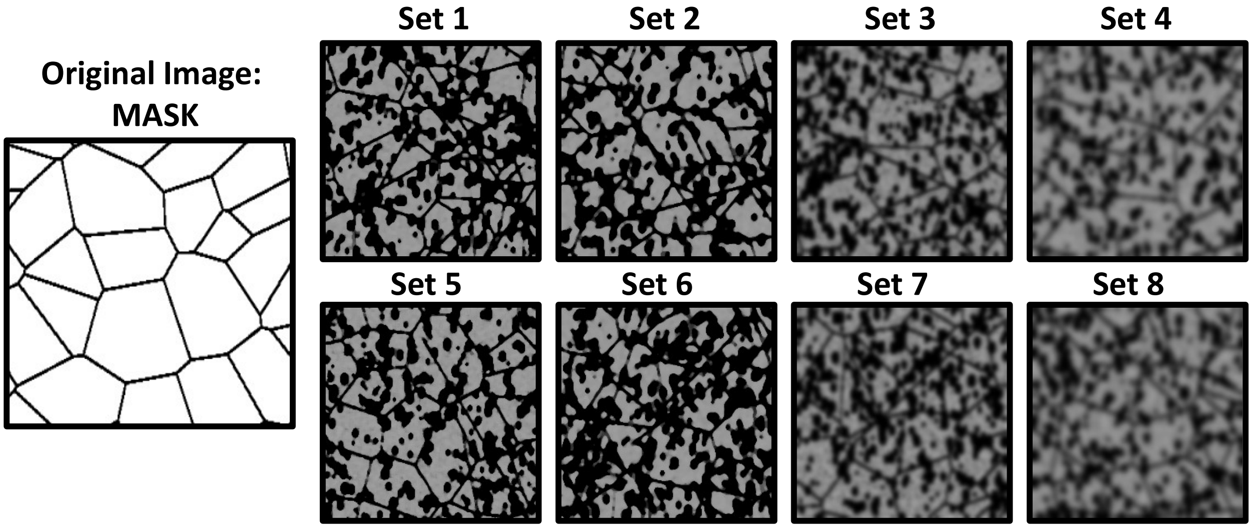

Figure 4.7: Artificial grain generation method: The original mask is on the left hand side of the figureand all of the different sets of generated grains are on the right and labeled set 1 through 8. The method of noise generation for each set is given in Table 4.6

for the classification was a sigmoid. The optimizer function was ADAM and the loss function was binary cross entropy. The batch size was 16, and training was conducted for 50 epochs. The validation split was 10%. The layout for the U-NET used can be seen in Figure 4.8.

4.5.2 Training Styles

The training and testing set split was 80 percent training and 20 percent testing. The two critical points are what is the training data and what is the desired outcome. The desired outcome is referred to as the mask. The mask is the group of pixels that we want to classify. In this case we want to classify specific pixels as either a grain or grain boundary. The mask is an image that has all the grain boundary pixels valued at 0 (black) and all grains valued at 255 (white). The masks for this work was always the manually segmented by human grain boundaries, except for the Voronoi generated data. The mask for the Voronoi generated data is known, it is the original, unaltered

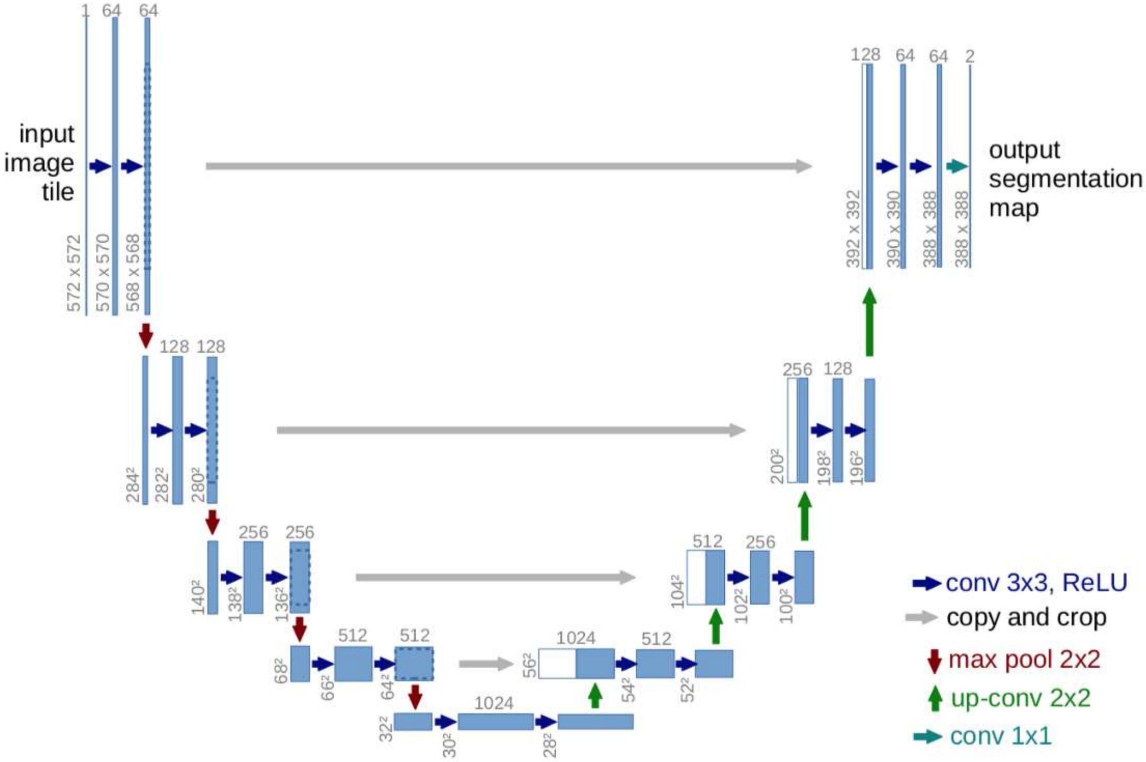

Figure 4.8: This is a diagram of a UNET from the First and Original paper on the UNET. caption[60]

Voronoi diagram. One example of this mask is shown in Figure 4.6.

The next critical portion of this work is what composition of the data is used for training. The most obvious method is too simply train the data using only data the has been manually segemented. The question is, would including the Voronoi tessalation grain generated data make the model more robust. This will be answered in the results section. The layout of the various training set compositions can be seen in Figure 4.9. The first 5 training compositions are just varying percentages of generated and manual segmentation. This was done to see the effect on just using the Voronoi method and just using the Manual method and be able to compare them to using a combination two techniques.

The training sets 6-10 are a little more intricate. The use of the traditional segementation methods in section 2.1, 2.2, and 2.3 were used to preprocess the data. This means that the mask remains the same (manually segmented image), but the original grain image is altered. The original grain image is altered by applying either the manual threshold method, the HED method, or the gradient method. After the traditional method has been applied, the U-NET is trained to go from the manually segmented image to the mask (manually segmented image). This was also done to see if this would make a more robust model.

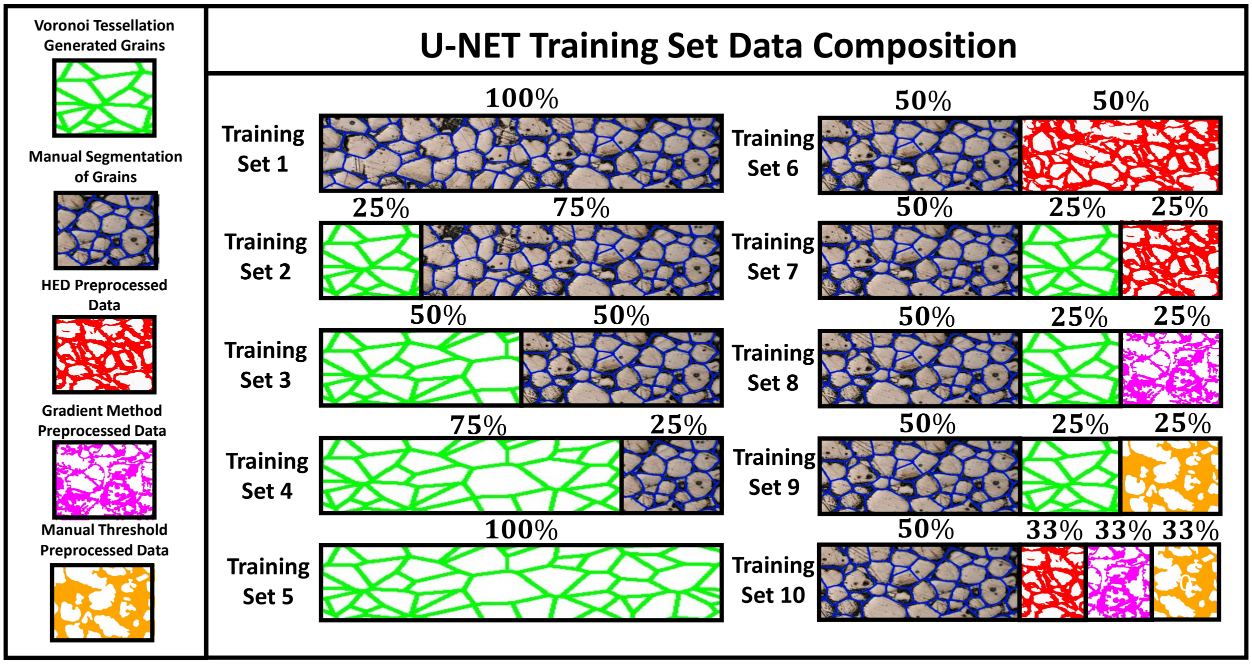

Figure 4.9: A visual breakdown of the various sets of data used for training neural networks in this work. The training sets are composed of either manually segmented data, artificially generated data, or preprocessed data through the HED method, Gradient Method, or Manual Threshold method

4.6 Results

In order to quantify the accuracy of the results of the different segmentation methods we need to examine the results. There are essentially two paths from which to approach how to examine the results. The first approach is a standard segmentation accuracy quantification method, known as the Dice score. The second will be to look at the actual grain data and see how accurate the measurements of various properties are. Both of these methods will be implemented and explained in the following sections. After looking at the quantative results, there is a section on the qualitative results of this work as well.

4.6.1 Dice Score

The dice score is a measure of the overlap between two sets of data. It is well suited for comparing the results of an image segmentation method. It is often used in machine learning and computer vision communities. This was used on all of the training set compositions for the U-NET seen in Figure 4.9. The dice score is a simple score that ranges from 0 to 1, where 1 is a perfect overlap and 0 is no overlap. For this work, the grain boundaries were the region of interest, so the Dice score was calculated based on how well the models could classify the pixels as grain boundaries. There are two graphs in this section which show the dice score for the various methods presented in this work. The dice score graph in Figure 4.10, shows the dice score for all of the traditional methods given in section 2. The dice score graph in Figure 4.11, shows the dice scores for the various UNET training compositions used in this work. The manually segmented image is regarded as ground truth in this work, that is why it scores a perfect score in both figures.

In the graph in Figure 4.10, we can see that the traditional methods do not score very high. One suprising piece of data is that the HED method actually scored the worst in the Dice score. The

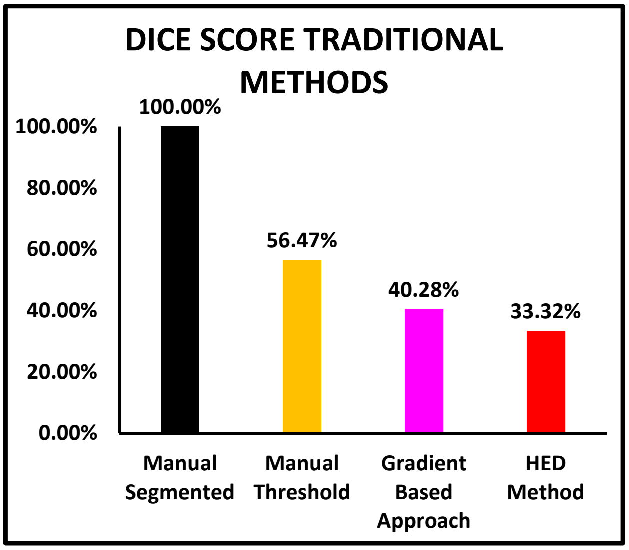

Figure 4.10: Bar graph for the Dice scores for the 3 traditional methods of grain segmentation: Manual Thresholding, Gradient Based Thresholding, and HED method for Thresholding. The ground truth for this measurement is the Manually Segmented images.

HED method does use a neural network model to detect edges, so the low Dice score was not expected. In general, all three of the traditional segmentation methods scored much lower, but that does not mean that these methods are completely useless. Noise can be generated using these methods to create more robust models, like the various UNET training methods seen in this work.

In the graph in Figure 4.11, the scores are all around 90%. The inclusion of fully artificially generated data in training sets 2, 3, and 4 did not have a negative effect on the score. The score did drop to 87%, when using all artificially generated data, which was training set 5. The dice score for training set 5 may be lower, but it is still an impressive score considering that the neural network for this model was never trained on any real grain images.

The dice scores for the training sets 6 through 10 show that incorporating the noise generated from the traditional methods does not have a negative impact in the dice score. This could be used to train models to become more robust or immune to the noise generated from these methods.

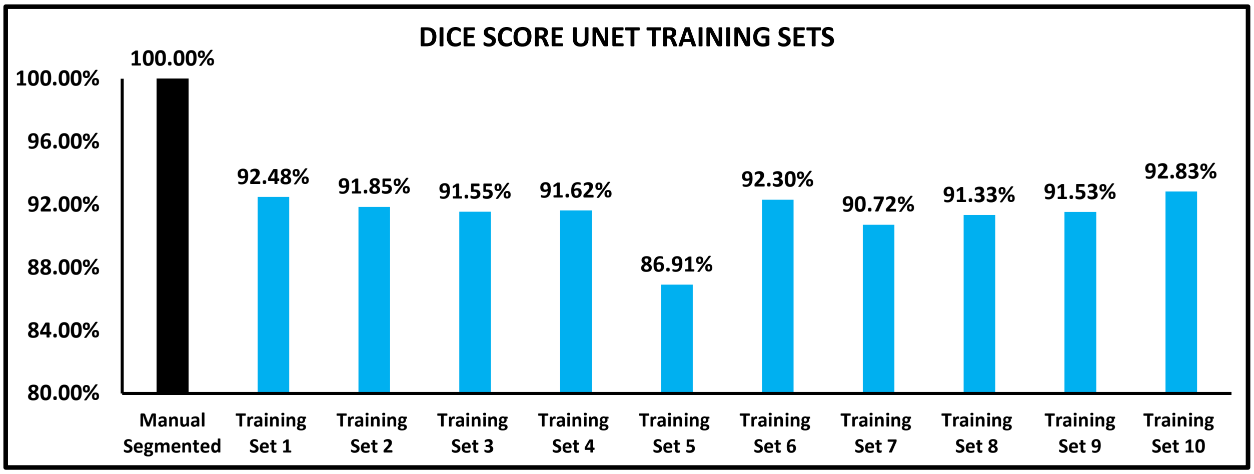

Figure 4.11: Bar graph for the Dice scores for the 10 training sets of data used to train the UNET used in this work. The ground truth for this measurement is the Manually Segmented images.

Training set 10 did have the highest score, and it did include some noise generated from all three of the traditional segmentation methods shown in section 2.

4.6.2 Grain Data

The dice score is a good metric for quantifying how well a neural network can classify pixels and is used frequently in the computer vision community. The materials science community though, should be more interested in how accurate are the geometrical measurements of the grains themselves. To get a basic view of how accurate all of the methods used in this paper are at grain measurements, we can use the standard error equation in Equation 4.6. Typically the absolute value is taken, but in order to see whether the method is over or under predicting the value, the absolute value was not included. The measured value is the average of all of the grain measurements and the true value is the average value for all of the grain measurements for the manually segmented method.

The error values are shown in Figure 4.12. On the X-axis of this figure, there are many important grain measurement values including: circularity, Average Maximum Diameter, Average X-Diameter, Average Y-Diameter, Grain Intercept Method X-Direction, Grain Intercept Method Y-Direction, Average Grain Area, and the Total Grains. The total grains counted is the only value where the average was not taken just the total number of grains found in the entirety of the images is given. All of the values in this table were calculated by measuring the grain data, taking the average, and then using Equation 4.6. The grain measurement values from the manually segmented images are regarded as the true value. The colorbar in Figure 4.12 illustrates how under or over the estimated value is. Blue indicates a positive error, this means the value has been overestimated. Red indicates a negative error, this means the value has been underestimated.

$$Error\ Percent = \frac{Measured\ Value - True\ Value}{Measured\ Value} \tag{4.6}$$

From the values in Figure 4.12, the three methods from section 2 (manual threshold, Gradient Approach, and HED Method) have the most inaccurate results. The error percentage is higher in these methods for all of the measurements. Of the three traditional methods, the manual threshold method seem to have the lowest error. The Gradient approach method and the HED method also both significantly overestimated the number of grains total in all of the images. This means that most of the values should skew smaller than they are in reality, because these methods are predicting so many grains. This is confirmed by looking at the average max diameter, average x-diameter, and average y-diameter. The manual threshold method also underestimates these, but not as much. The gradient method had the highest errors of all the methods.

The Unet training set variations all had much lower errors in general. The highest error of the UNET was training set 5, which was trained entirely on artificial data. Training set 5 underpredicted the amount of grains by about 38%. This is becuase some of the boundaries did not get

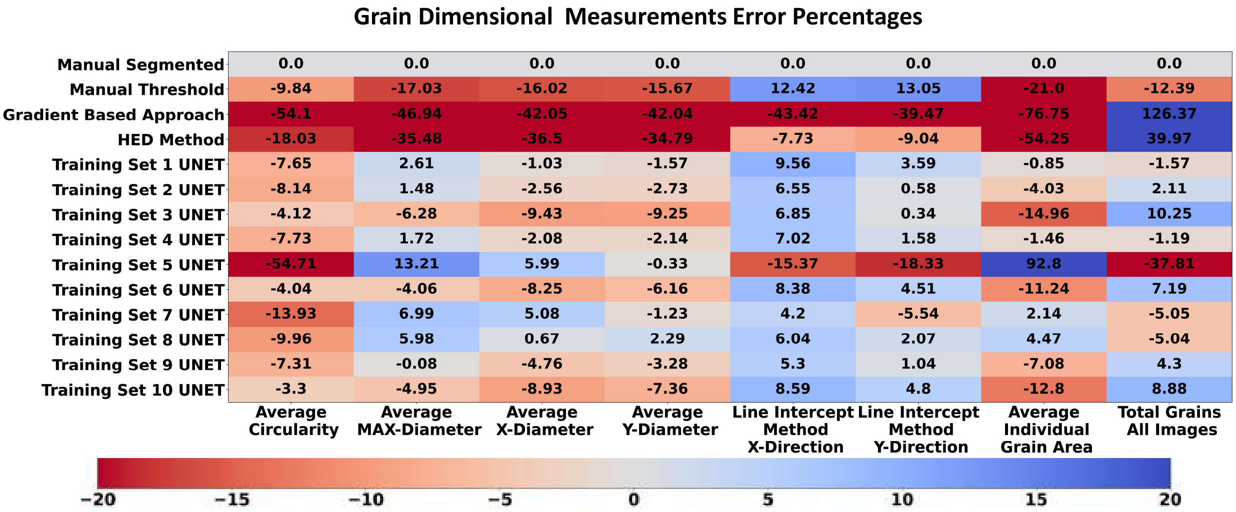

Grain Dimensional Measurements Error Percentages

	Average Circularity	Average MAX-Diameter	Average X-Diameter	Average Y-Diameter	Line Intercept Method X-Direction	Line Intercept Method Y-Direction	Average Individual Grain Area	Total Grains All Images
Manual Segmented	0.0	0.0	0.0	0.0	0.0	0.0	0.0	0.0
Manual Threshold	-9.84	-17.03	-16.02	-15.67	12.42	13.05	-21.0	-12.39
Gradient Based Approach	-54.1	-46.94	-42.05	-42.04	-43.42	-39.47	-76.75	126.37
HED Method	-18.03	-35.48	-36.5	-34.79	-7.73	-9.04	-54.25	39.97
Training Set 1 UNET	-7.65	2.61	-1.03	-1.57	9.56	3.59	-0.85	-1.57
Training Set 2 UNET	-8.14	1.48	-2.56	-2.73	6.55	0.58	-4.03	2.11
Training Set 3 UNET	-4.12	-6.28	-9.43	-9.25	6.85	0.34	-14.96	10.25
Training Set 4 UNET	-7.73	1.72	-2.08	-2.14	7.02	1.58	-1.46	-1.19
Training Set 5 UNET	-54.71	13.21	5.99	-0.33	-15.37	-18.33	92.8	-37.81
Training Set 6 UNET	-4.04	-4.06	-8.25	-6.16	8.38	4.51	-11.24	7.19
Training Set 7 UNET	-13.93	6.99	5.08	-1.23	4.2	-5.54	2.14	-5.05
Training Set 8 UNET	-9.96	5.98	0.67	2.29	6.04	2.07	4.47	-5.04
Training Set 9 UNET	-7.31	-0.08	-4.76	-3.28	5.3	1.04	-7.08	4.3
Training Set 10 UNET	-3.3	-4.95	-8.93	-7.36	8.59	4.8	-12.8	8.88

Figure 4.12: A color map superimposed on the numerical values for the various grain dimensional measurements used in this work. The measurement error is provided for the 3 traditional segmentation methods and all ten of the UNETs trained on differing training sets. The training set compositions are given in Figure 4.9. The manually segmented images are regarded as the true value for this error measuremnt.

closed entirely causing too many grains to be connected, by small neck regions. This is also evident by looking at the circularity of the training set 5 predictions. The lower circularity means that the regions of predicted grains were not enclosed in a circular manner, most likely having extended neck regions that were not closed correctly. Training set 1 performed very well acroxx the board, and the addition of artificial grains in set 2, set 3, and set 4 did slightly increase the error percentages. Sets 2, 3 and 4 did outperform all of the traditional methods and some of the other training sets. Training set 10 also performed well, this indicates including some of the noise from the traditional methods can be beneficial to the training process, and including a variety of this noise is beneficial as well.

4.6.3 Qualitative Results

In order to take a deeper look into the capabilities of this approach, some qualitative results will be supplied in this section. The qualitative results are given in the form of individual image results. By looking at an individual grain boundary segmentation we can see what is happening on a case by case level.

The first example images are given in Figure 4.13. The images in this figure are from the UNET that was trained on data set 3. Data set 3 was composed of 50% real grains with manual segmentations and 50% artificially generated grains from the Voronoi tessellation method created in this work. Image 3 in Figure 4.13 shows the UNET prediction of the original mask (shown in image 2). The UNET was able to predict mask after only receiving image 1. Image 1 was an image taken from the testing set, which means the UNET had never seen this specific image, but was trained on similar images.

This same UNET (from training set 3) was also able to predict the grain boundaries of a real grain image as well. An example of this is also shown in Figure 4.13. Image 4 is an example of a real grain image. Image 5 is an example of the manual segmentations, hand drawn by a human. Image 6 is the prediction that the UNET made of the same grain boundaries. The similarities between image 5 and 6 is very striking. This grain image and manually drawn segmentation, are also from the testing set, meaning the UNET never saw these images during training, but did see similar images. The superior ability of neural networks for grain boundary segmentation is shown very clearly in this figure.

In Figure 4.14, the results of a UNET that was trained entirely on artificially generated data (training set 5) is displayed. This UNET was never trained on actual grain boundary images, and only trained on data created via the Voronoi tessellation grain generation method created in this work.

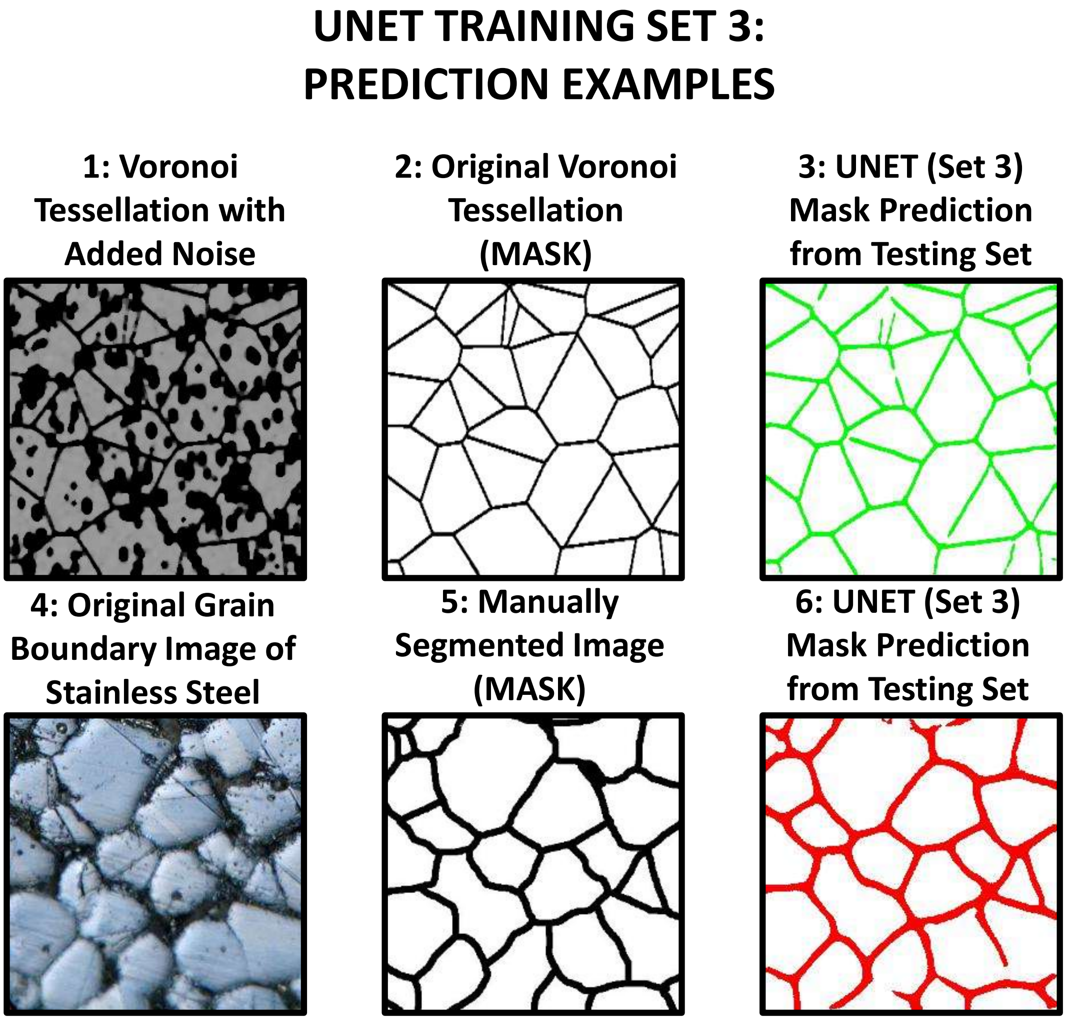

Figure 4.13: Qualitative results from the UNET trained on training set 3. This training set is composed entirely of artificial data. (1) An artificial grain generated from the Voronoi Tessellation method. (2) The mask from image 1. (3) Prediction of the mask from UNET trained on data set 3. (4) Real grain image. (5) Mask of the manual segmentation of image 4, complete by a human. (6) UNET training set 3 prediction of the mask of image 4.

Images 1 in Figure 4.14, shows a real grain image of stainless steel (image was taken for this work), and overlayed on the image in green is the predicted mask from UNET trained on data set 5. Even though the UNET was not trained on this data at all, it was still able to make a fairly accurate estimation of the grain boundaries. The grain boundaries with a manually drawn grain boundary is

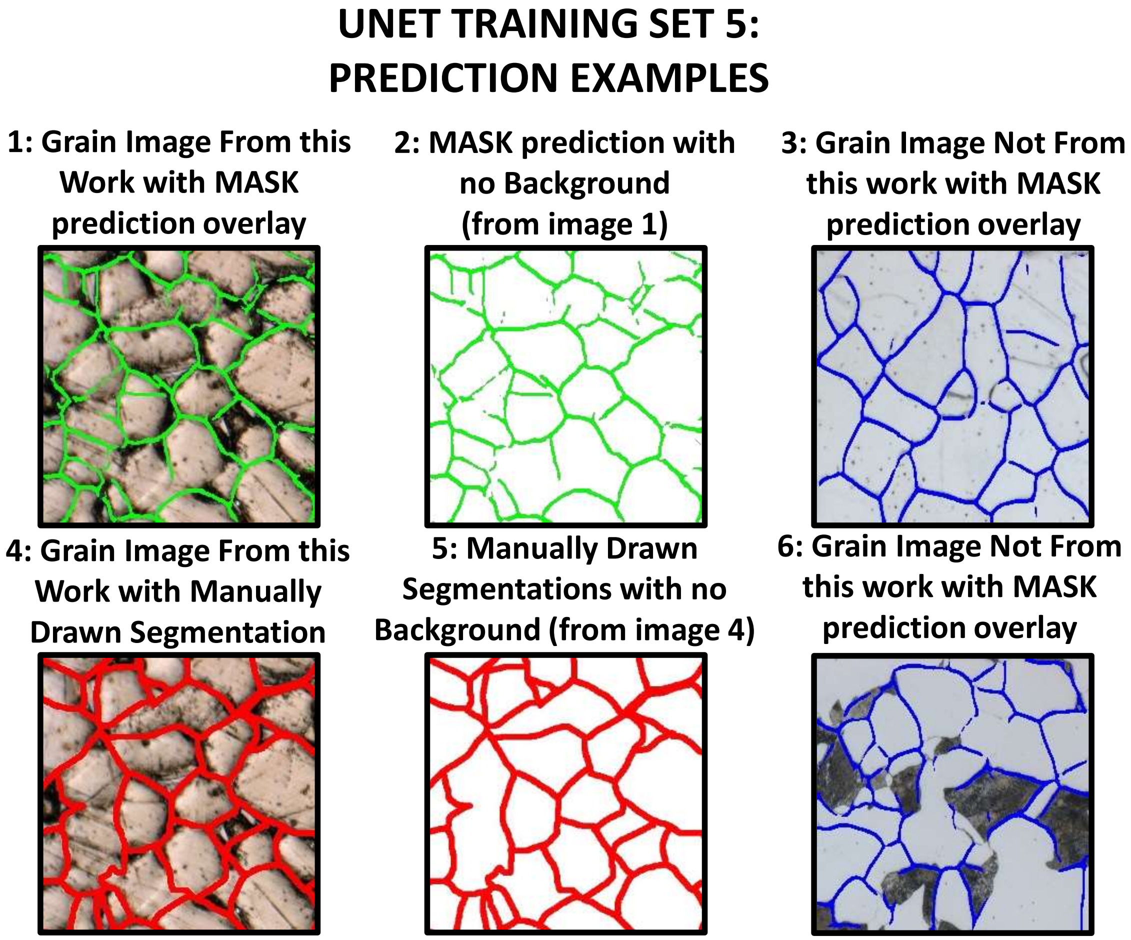

Figure 4.14: Qualitative results from the UNET trained on training set 5. This training set is composed of 50% manually segmented real grains and 50% artificially generated grains. (1) Real grain with a prediction of mask from UNET overlaid. (2) The mask from image 1 with background removed. (3) Image of grains this UNET did not train with predition of mask overlaid (4) Image 1 with manually segmentations overlaid (5) The mask from image 4 with background removed. (6) Image of grains this UNET did not train with predition of mask overlaid

shown in image 4. Images 2 and 5 are the masks without the grain boundaries, they are provided for comparison. They are not a perfect match, but UNET 3 did manage to not predict an voids as grain boundaries, and also did not predict any polishing scratches as grain boundaries as well.

Images 3 and 6 are images of stainless steel manufactured via injection molding. These images were not taken for this work, and they were not used for training. They are just given to show how this type of training using artificial data can be implemented to create more robust models. The UNET trained on data set 5 was able to make fairly accurate predictions for the grain boundaries in these images as well. In image six some of the grains are of a very dark color, and the UNET was still able to get the grain boundaries around the darker grains as well.

4.7 Conclusion

The conclusions from this work will be broken down into the different approaches to keep the statements organized and make it more clear.

The Traditional Methods: The traditional methods include manual thresholding, the gradient based approach, and the HED method. All of these methods require a a determination of the best settings for a given dataset of images, and cannot be applied universally. The inverse of portions of these methods can be used for noise generation to create more robust models.

UNET Training Set 1: Training set 1 performed well on both the dice score and the actual grain measurements, this should be expected. This UNET was trained only on the manually segmented images. The manually segmented images were regarded as ground truth throughout this work, so this UNET should be viewed as the best possible scores for this approach. The UNET training hyperparameters were constant for the UNETs, only the training data was varied.

UNET Training Sets 2-4: Training sets 2-4 included varying amounts of artificially generated Voronoi tessellation grains. At no point did the dice score or grain measurement accuracy drop significantly. The inclusion of artificial data can be used to increase the amount of training data, while not affecting the accuracy of the model.

UNET Training Set 5: Training sets 5 did perform the worst of all the UNETs, but the scores were still pretty reasonable. This is interesting because this UNET was trained entirely on artificially generated data. This shows it is possible to create or train a neural network to determine grain boundaries entirely from artificial data. It is also possible for the results to be better than the traditional methods such as gradient based approaches, manually thresholding, and the HED method.

UNET Training Set 6-10: Training sets 6-10 incorporated a varying amount of data the was filtered through the traditional methods. This means that the network was trained on some of the noisey data generated from the traditional methods. All of the models score very well on the Dice score and also had very accurate grain measurements. Set 10 included noise from all three of the traditional methods and scored the best out of all of them. This means that incorporating noise from all of these methods is beneficial to training. This could be used to create more robust models, capable of determining grain boundaries on various grain image settings and materials. Including artificial data can also assist in this goal.

Planimetric and Line Intercept Method: Planimetric and Line Intercept methods were both used to obtain various grain measurements in this work. The line intercept method is not as accurate as a full planimetric analysis, as should be expected. It can be used as a quick estimate, but more data is available with a planimetric analysis. Also more accurate measurements are possible through a planimetric analysis. A deep learning approach to image segmentation can create a suitable image for planimetric analysis as well.

Final Statements: A novel approach to data generation for grain boundaries was developed in this work. The artificial data included pores, polishing scratches and small grain fragments. The qualitative results from the UNET trained only on artificial data showed an ability to avoid polishing scratches and pores when predicting the grain boundaries. One weakness of the UNET trained on this data was the grains were not consistently closed, in other words, a small neck region would be opened connected two grains. This is the cause of the slightly lower dice score and grain measurement capabilities of this model.

For future machine learning and artificial inteliigence applications in materials science to be possible, scientist should continue to try to publish their data for others to use. In this work, we published a significant amount of grain data images from a fairly new method of additive manufacturing. Contributions to the data sets are just as important as the contributions to literature when dealing with machine learning applications.

CHAPTER 5: PARTICLE RECYCLE ITERATION DETECTION

5.1 Introduction

Laser Powder Bed Fusion (LPBF) is a 3D printing technique that uses a high-energy laser to melt and fuse together layers of powdered material, to create a 3D object. Metals and metal alloys are a difficult material to 3D print, but are able to be printed using LPBF [85, 28]. The process begins with a thin layer of powdered material being spread evenly across a build platform. A high-precision laser beam is then used to selectively melt the powder in the desired areas. As each layer is melted and solidified, the build platform is lowered and a new layer of powder is spread on top. This process is repeated layer by layer until the final 3D object is formed. LPBF enjoys all of the usual advantages over traditional manufacturing techniques. It allows for the creation of complex geometries and internal structures that cannot be produced using other methods [26]. It also has the potential to reduce material waste and lead times, and can enable the production of customized or one-of-a-kind parts.

Powder quality is critical parameter to the LPBF process. Powder quality has a direct affect on the quality and integrity of the final 3D printed part [92]. In LPBF, unused powder is typically reused for future builds. As a result, the powder quality can degrade over time due to oxidation, contamination, and other factors [93]. It is important to monitor and maintain the quality of the powder to ensure consistent quality of the printed parts. The size and shape of the powder particles can affect the packing density, flowability, and surface area of the powder bed, which in turn can affect the quality and consistency of the final part [94, 95]. Contaminants such as moisture, oxygen, and other particles can negatively impact the melting and solidification behavior of the material, leading to porosity, cracking, and other defects. Overall, the quality of the powder used in LPBF is critical to the quality and integrity of the final 3D printed part [96].

When powder is being reused in LPBF, it is important to evaluate its quality at each iteration of recycling to ensure that it meets the requirements for producing high-quality parts. Visual inspection of the powder can be used to detect any signs of contamination, clumping, or degradation [97, 98, 99]. With adequate visual images of the powder, a particle size distribution analysis can be completed. This analysis can be used to determine if the powder has changed in size distribution due to repeated use. Changes in particle size distribution can impact the packing density, flowability, and surface area of the powder bed. By monitoring the quality of the reused powder, it is possible to determine if the powder is still suitable for use in LPBF, or if it needs to be replaced to ensure the quality and integrity of the final parts. It is important to establish a consistent powder quality control process to ensure the quality of the powder is maintained over time [100, 101].

The recycling powder process typically involves sieving the powder to remove any clumps or large particles, and then mixing it with fresh powder to restore the desired particle size distribution and chemical composition. The excess unmelted powder is removed from the build chamber. This powder is typically collected and stored separately from the used powder that has been melted.

The used powder is sieved to remove any clumps or large particles. This helps to ensure that the powder has a consistent particle size distribution and flowability, which is important for achieving consistent quality in future builds. The recycled powder is then evaluated for quality using visual inspection methods. The development of these visual inspection quality determination methods is on-going, and is the focus of this work. Powder quality determination will ensure that the recycled powder meets the necessary requirements for producing high-quality parts.

Machine learning (ML) is a very efficient tool for processing, classifying, predicting, identifying, and analyzing data. ML techniques can be implemented on powder quality images to better determine powder quality, which can lead to more efficient and accurate quality control in LPBF [99, 102, 82]. By training a neural network on a large dataset of powder quality images, the model can quickly learn to identify patterns and features that are indicative of good or bad powder quality. This will enable faster and more accurate quality control of the powder. Lower resolution images and even fewer images will be required, if this methodology is correctly implemented. The images must be analyzed to identify the features that are most relevant for determining powder quality. This can be done by using convolutional neural networks (CNNs) to automatically extract features from the images. CNNs are currently the best method in ML at image segmentation and classification.

A machine learning model must be trained on microstructure images and extract visual features to predict the quality of the powder. This work will use both supervised learning, where the model is trained on labeled data, and unsupervised learning, where the model is trained to identify patterns in the data without explicit labels. The performance of the machine learning models trained in this work are evaluated using metrics such as accuracy, precision, and recall. The trained machine learning models can be deployed in the LPBF process to automate quality control of the powder. Overall, setting up a framework for machine learning in this field requires a significant amount of data collection, preprocessing, and model development. Once the framework is established, it can provide significant benefits in terms of efficiency and accuracy of powder quality control in LPBF [103]. There is a significant amount of authentic LPBF recycled powder microstructural data gathered processed in this work. The standard CNN models implemented in this work, show great promise, while also providing much need baselines for future researchers [23, 104].

5.2 Data Collection Methods

LPBF recycles and reuses powder after prints to save on material costs, and the powder bed is so large, that much of the powder is not in contact or even near contact with the laser. For this work, images of the powder were collected from a scanning electron microscope (SEM). For each category a total of 20 (1024 x 7968) images were collected at 500X. To better prepare these images for machine learning applications, and to expand the dataset, the images were split. The images were split 4 in the X and 3 in the Y. This makes 12 (256 x 256) images for every image. This brings the total images per category to 240, and each of these images is 256 x 256 pixels. This entire preprocessed dataset, along with all of the coding used in this work is available on kaggle [12].

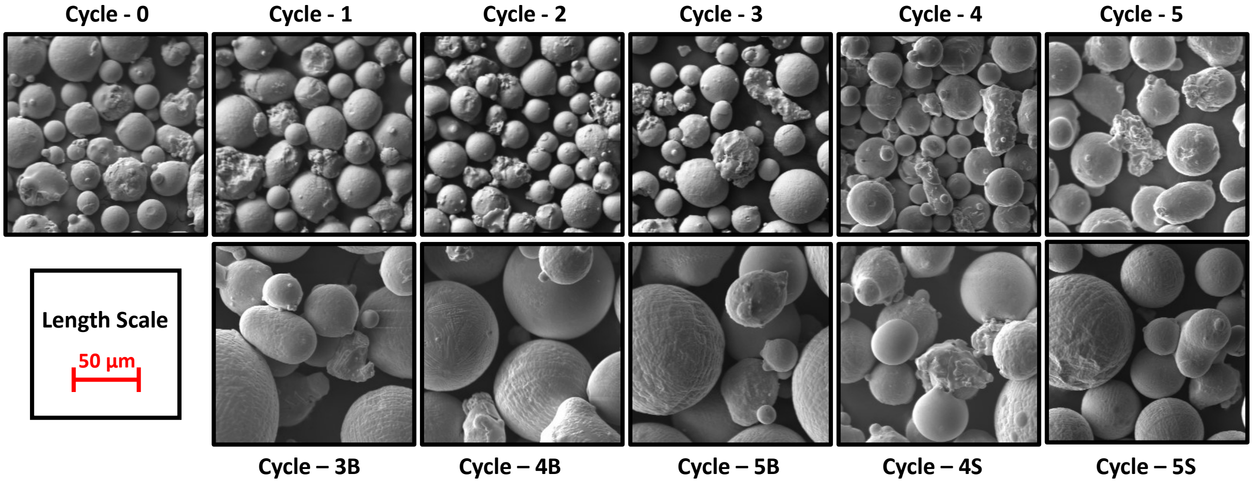

Figure 5.1: This is one example for all eleven powder categories that had images gathered in this work. The images are in black and white and are 256X256 pixels. The length scale is the same for all the images and is provided in the lower left image.

There were a total of 11 categories of powder were collected. An example of a 256 x 256 image from each category is shown in Figure5.1. At the top of the figure, from left to right we can see cycles 0 through 5. Cycle-0 is fresh powder, and after each print the powder is filtered through a 40 micron sieve and reused. Cycles 1 through 5 are labeled based on how many prints the powder has been recycled from, and that it was also filtered each time through the 40 micron sieve. Cycles 0 through 5 powder, can currently be classified as "acceptable" powder.

In this work, "unacceptable" powder images were also collected. Examples of these images are shown at the bottom of Figure5.1. The powder that was collected in the 40 micron sieve after each print was saved. This is the powder that could not fit through the sieve. Cycles 3B, 4B, and 5B indicate the powder that was collected in the sieve after the powder had been recycled 3, 4, or 5 times. The final two categories are 4S and 5S. These categories are the soot from the print chamber. This is powder that was left over in the print chamber. This powder typically sticks to the walls of the print chamber and during a material change it will get washed off and not reused. The soot is not considered to be acceptable or unacceptable, but is just typically expelled in common practice, because it is not worth the effort to retrieve.

5.3 Preliminary Data Analysis

There are many ways to conduct a particle analysis with microscopic images. In this work, machine learning methods are used to increase the accuracy of standard image thresholding methods. A large portion of the challenge is to segment the particles from the background and from each other. To tackle this challenge the Holistically Nested Edge Detection (HED) neural network was used in conjunction with other standard thresholding methods to get a fairly accurate segmention for the particles [89]. An example of the process used is shown in Figure5.2.

In the first image (top-left) on Figure5.2, there is a 256x256 image from the cycle 2 dataset. To the immediate left of this is the image that results from applying an HED neural network. To the immediate left of that image is the result of subtracting image 2 from image 1. The value of the pixels ranges from 0 (black) to 255 (white). The result of this subtraction yields a much more clear perimeter for the particles. The outer wall of the particles will be easier to threshold from the particles. This is shown in image 4, where an adaptive mean threshold is applied to the image with a kernel size of 11x11. Image 5 shows the result of the computational segmentation of the particles from image 4. When the segmentations are overlayed on the original image (shown

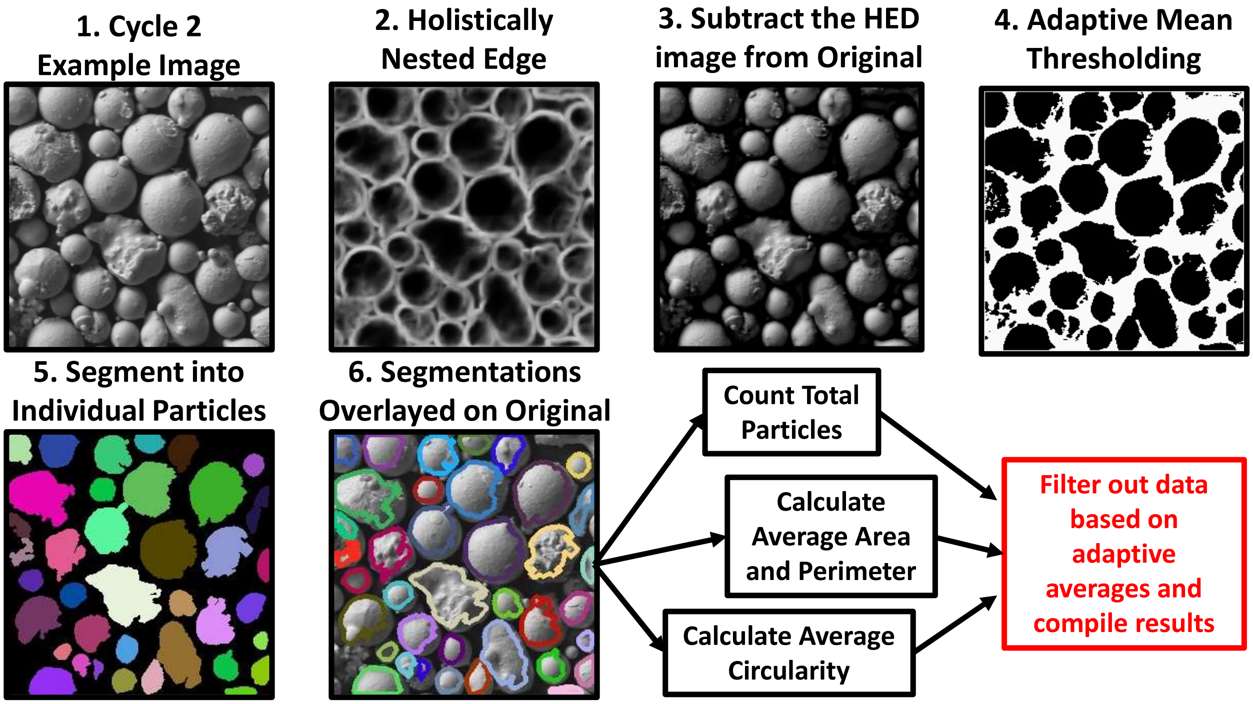

Figure 5.2: Step by step example of the particle segmentation method used for particle analysis in this work. Image 2 is the application of the Holistically Nested Edge detection (HED) neural net. Image 3 is the subtraction of image 2 from image 1. Image 4 is an adaptive mean threshold of with a kernel size of 11x11. Images 5 and 6 show the final segmentation of individual particles.

in image 6), it shows a fairly accurate segmentation. The particles are slightly under predicted in total size, but this is necessary to ensure multiple particles do not get merged together in the segmentation process. It is easy for overlapping particles to get counted as a single particle and throw off the average area measurement. For the purposes of this work it is preferred that the overlapping particles are definitely not counted as a single particle.

After the segmentation process is complete, the total particles are counted and analyzed. The average area and perimeter are tallied and stored. Prior to plotting the particles, some of the data must be filtered out. In some cases a small speck, can be mistaken for a particle. The only filter method for this preliminary data analysis was a minimum area filter. Any particle that was

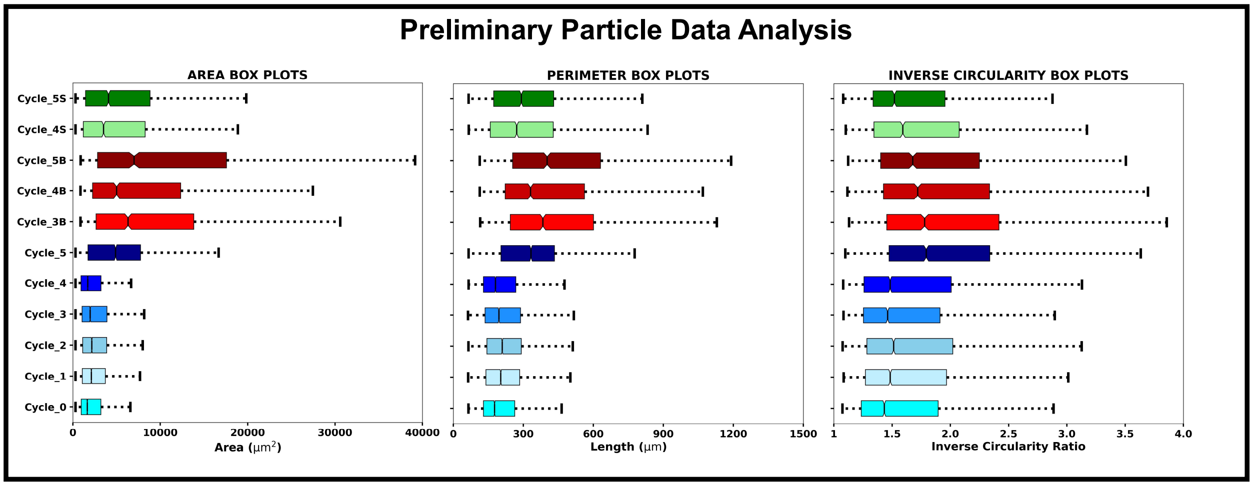

Figure 5.3: Three box plots are provided, one for area, one for perimeter, and one for inverse circularity. The whiskers are set to 1.5 times the interquartile range (IQR). Associated numerical data is provided in Table 5.3.

less that 100 μm^2 was not counted. This is equal to a particle of radius 5.6 μm. The inverse circularity of the particles can also be calculated from the area and perimeter. The equation for inverse circularity is given in equation 5.1 [105]. The inverse circularity ranges from 1 (perfect circle) to infinity (absolutely not a perfect circle). For reference, an equilateral triangle has an inverse circularity of 1.67, a square has an inverse circularity of 3.14, and an equilateral pentagon has an inverse circularity of 4.32. The inverse circularity function is a good method at detecting satellites, fractures, and ablations in the particles.

$$Inverse\ Circularity = \frac{P^2}{4\pi A} \tag{5.1}$$

To conclude the preliminary data analysis, box and whisker plots will be made for the three most important descriptors of the particles: area, perimeter, and inverse circularity. The whiskers for these plots are set to 1.5 times the interquartile range (IQR). The box and whisker plots were made for all eleven of the powder categories. Examples of the eleven powder categories can be seen in Figure5.1, and the box and whisker plots can be seen in Figure5.3. The numerical results for the average and standard deviation of the area, perimeter, and inverse circularity are given for all the particle categories in Table 5.3. The total number of particles counted over the entirety of the data for each category is provided in Table 5.3 as well.

Table 5.1: Particle Size Measurements

Category	Area μm^2	Perimeter μm	Inverse Circularity	Total Count
Cycle 0	$2,500 \pm 2,418$	215.2 ± 131.6	1.72 ± 0.79	7,550
Cycle 1	$2,749 \pm 2,308$	230.8 ± 133.9	1.78 ± 0.83	6,801
Cycle 2	$2,792 \pm 2,314$	234.8 ± 133.5	1.81 ± 0.84	6,700
Cycle 3	$2,882 \pm 2,668$	232.6 ± 142.1	1.74 ± 0.77	6,532
Cycle 4	$2,653 \pm 3,321$	230.1 ± 198.9	1.85 ± 1.13	8,172
Cycle 5	$5,253 \pm 4,037$	339.1 ± 185.7	2.09 ± 0.96	4,280
Cycle 3B	$10,711 \pm 12,911$	464.4 ± 294.3	2.12 ± 1.01	2,136
Cycle 4B	$10,167 \pm 12,874$	444.2 ± 327.4	2.05 ± 0.98	2,191
Cycle 5B	$13,253 \pm 16,907$	504.4 ± 374.2	2.09 ± 1.23	1,623
Cycle 4S	$6,978 \pm 9,775$	340.9 ± 264.1	1.88 ± 0.89	3,147
Cycle 5S	$6,766 \pm 7,997$	333.2 ± 218.7	1.79 ± 0.78	3,070

The box and whisker plots are useful at displaying how the data skews larger area, longer perimeter, and higher inverse circularity for the particles. It is clear that all three of the variables skew larger as the recycle iteration goes from 0 to 5. The one outlier is the 4th recycle iteration, which seems to be comparable to the fresh powder. This could possibly be explained from the experimental side, in either imaging or the handling of the powder. The differences between the 3B, 4B, and 5B particle data with the rest of the data is clear. These particles are easily detectable as unusable powder. The 4S and 5S does skew higher than the majority of the good recycled powder, with the exception of the 5th iteration of recycled powder.

The numerical data for the powder is given in Table 5.3. The total particl count does go down for the larger powder datasets (3B, 4B, and 5B) and also for the soot (4S and 5S). This is a result of less particles being in each image because of the larger average size of the particles. This can be confirmed by looking at the average area and perimeter of these categories as well. The "good" powder (Cycles 0 - 5) does show an increase in area, perimeter, and inverse circularity as the cycle recycle iteration count increases. Again the only exception is cycle 4. The data from this table is the same data that is plotted in the box and whisker plots in Figure5.3.

5.4 Machine Learning Approach

A Convolutional Neural Network (CNN) is a type of artificial neural network commonly used for image classification, object detection, and segmentation tasks. Unlike traditional neural networks, CNNs are designed to automatically identify and extract features from image data using a series of convolutional layers [106]. CNNs have an ability to automatically learn and identify complex features within images, making them an ideal candidate for image classification tasks. The utilization of convolutional layers, which apply a filter to the image and output a feature map that highlights areas of the image, allows CNNs to capture complex spatial relationships between the pixel intensities in a given image.

ResNet (Residual Network) is a type of CNN architecture that was introduced in 2015 to improve the performance of deep neural networks [72]. ResNet introduced a new building block called the residual block, which allows for easier training of deep networks by addressing the problem of vanishing gradients. This block can be seen in Figure5.4. The residual block includes a shortcut connection that allows the network to bypass one or more layers, which helps to prevent the gradients from becoming too small during training. This enables the ResNet architecture to achieve very deep networks, with over 100 layers, while still maintaining high accuracy on image classification tasks. The Resnet18 will be the convolutional neural network architecture used for the classification and segmentation tasks in this work.

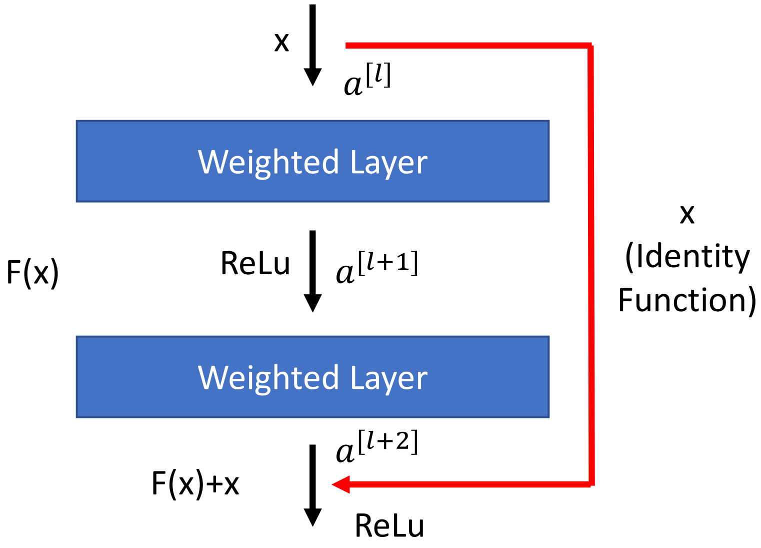

Figure 5.4: A basic residual building block diagram that makes up the resnet architecture. Relu is a rectified linear unit. This diagram details how the identity function passes through the layers of a given neural network.

The Resnet18 is very good classification neural network because it has a deep architecture with skip connections that allow for better feature extraction, and it uses batch normalization and ReLU activation functions to help prevent the vanishing gradient problem during training [72]. The Resnet18 will be used for all of the models in this work. The dataset that was gathered in this work, will be split in a variety of ways to examine the Resnet18's ability to classify the images. In Figure5.5, the layout of all of the training sets can be seen. There is a total of 4 different training set compositions. The increase in difficulty with each training set. Training set 1 is good powder vs bad powder, set 2 is early cycles vs late cycles, set 3 is 4 categories, and set 4 is 7 categories. Training set 3 is broken into early cycle, late cycle, soot, and bad powder. Training set 4 is broken down into every cycle (from fresh to cycle 5) and also has a category for bad powder. All of the specific powder examples are given in Figure5.1, and the specific powders in each training category are listed in Figure5.5.

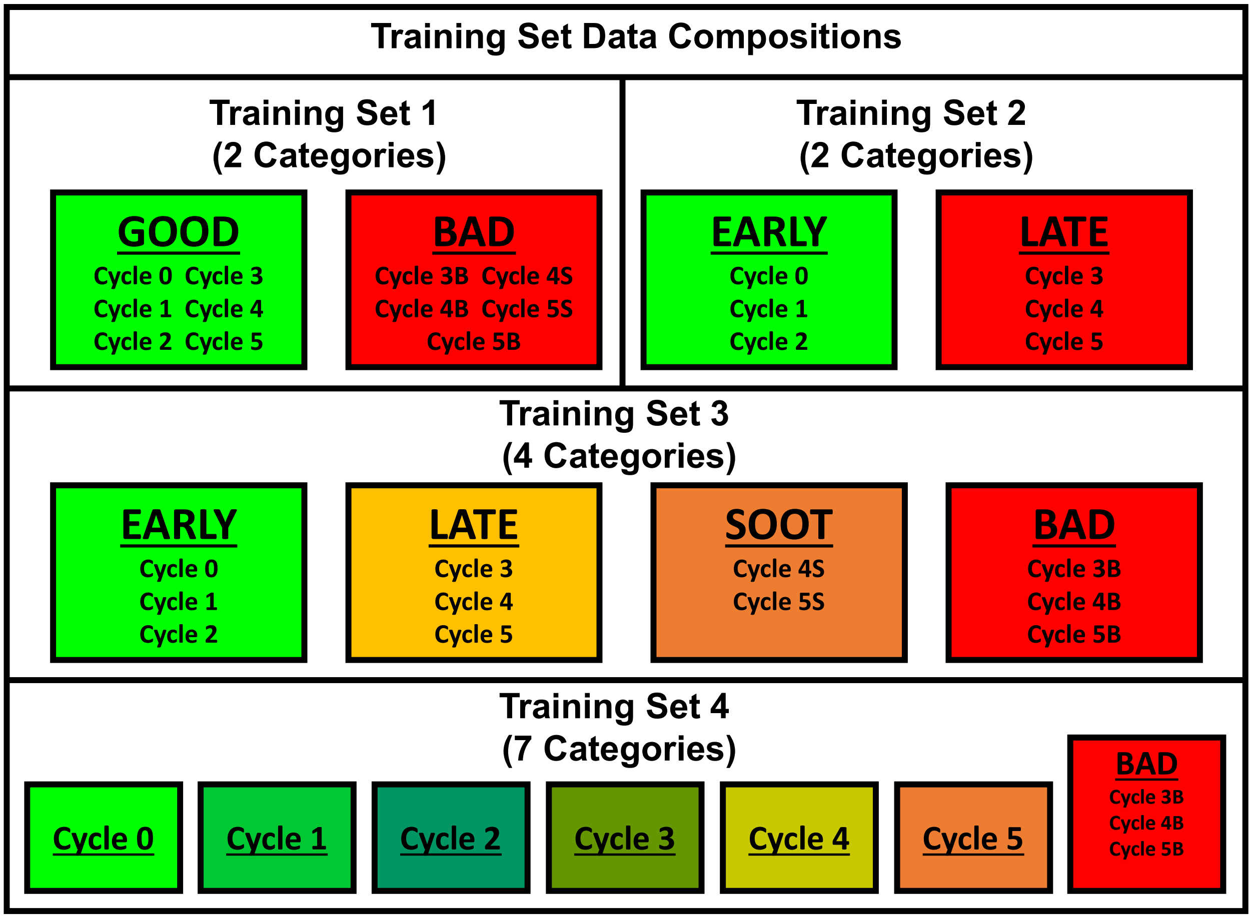

Figure 5.5: Training set data composition for the 4 different training sets. The categories provided in this figure had examples of images provided in Figure5.1.

The CNN used was a Resnet18. The loss function was cross entropy loss. The batch size was 16. The image size was 256 x 256, and the images were in black and white. The optimizer for training sets 1 and 2 was Adam, the learning rate was 0.001, and the epsilon value was 1e-8. The optimizer for training sets 3 and 4 was stochastic gradient descent (SGD), the learning rate was 0.001, and the epsilon value was 1e-8. All of the code for the training is provided on publicly available notebooks on kaggle under the dataset [12]. The amount of epochs was 12 for training set 1 and 15 for trainings sets 2, 3, and 4. The test train split was 80-20, and this process was random.

The reason for splitting the data into good vs bad powder, is because this is essentially the most important classification for the printer user. The early and late training set is also tested to see if the CNN can determine between low recycle iteration and high recycle iteration powder. These differences are not clear from the preliminary dataset analysis. Training set 3 was tested to see the CNNs ability to classify into multiple categories. Training set 4 is the biggest challenge for the CNN. This training set will determine if the CNN can identify powder based on what recycle iteration it is in, and determine if the powder is still usable. The training results and predictive capabilities will ge given in the next section. The accuracy of every training set composition, epoch vs loss graphs, and confusion matrices will be provided in Section 5: Results and Discussion.

5.5 Results and Discussion

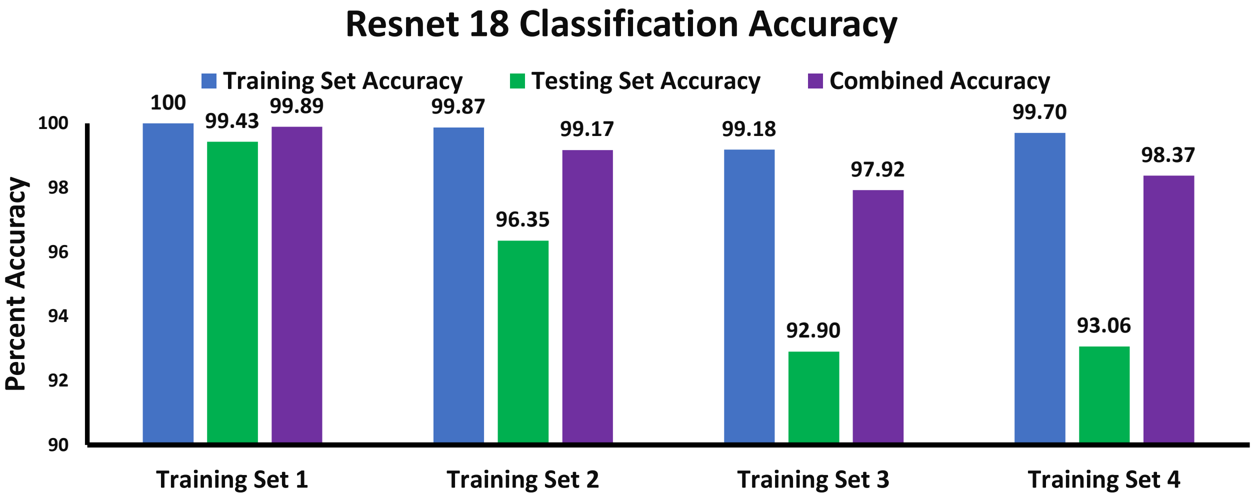

Figure 5.6: The accuracy of the Resnet18 classification after training. This is given for all 4 training sets provided in Figure 5.5. The training set, testing set, and combined accuracy are provided for each.

The Resnet18 classification accuracy of training set, testing set, and the combined set for all of the different dataset compositions is provided in Figure5.6. The composition of sets 1 through 4 was already provided in Figure5.5. The more critical accuracy is the testing set accuracy, because this is data that the CNN never trained on, and therefore never saw until testing. The good vs bad accuracy was near perfect. This indicates that this style of powder classification could be very beneficial in just determining whether powder could be used or not. On set 2, the classification is between early and late cycle powder. The testing set accuracy is still quite high at around 96%. This indicates that it is possible to determine a differences in the powder based on how many times the powder has been recycled. Training sets 3 and 4 did see a further drop in accuracy for their associated testing sets. These training sets were more complex and had more categories, so this should be expected.

A confusion matrix is a table used to evaluate the performance of a classification model by comparing its predictions against actual outcomes. It shows the number of true positives, false positives, true negatives, and false negatives. The confusion matrices for training set 3 and training set 4 are provided in Figs 5.7 and 5.8. These confusion matrices are only providing the prediction data for the testing sets of the associated dataset. The results from these confusion matrices are quite promising. There is a possibility that because of the (black-box) nature of a CNN, that these models are making predictions based on criteria that is not completely based on powder characteristics. Maybe the contrast in the SEM was set to a different lighting, maybe the powder was put on the slide a certain way, or some other unknown and unseen criteria is allowing these CNNs to make the predictions with such high accuracy. The confusion matrix in Figure5.7, shows that the CNN is much more likely to confuse high cycle with low cycle and soot with bad powder. The confusion matrix in Figure5.8, shows that if a powder is confused for another category it is most likely confusing it with a powder in a recycle iteration count close to the one that it is. Cycle 1 might be confused with fresh or cycle 2, but not confused with bad powder. This does indicate that the

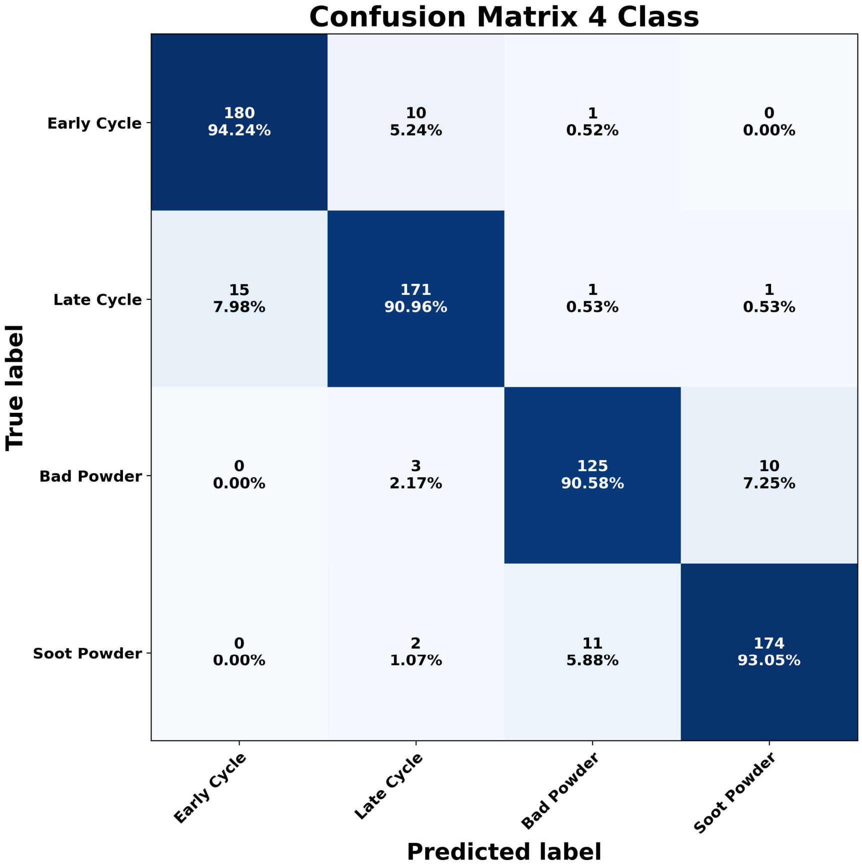

Figure 5.7: Confusion matrix for the results of the testing set for training set 3. Training set 3 has four classes as shown in Figure 5.5.

CNNs are at the very least partially identifying powder features and using those to classify the images. At best, they would be only considering powder related features. The classification for bad powder was 100% and only 3 images from cycle 5 (the highest recycle count) were classified as bad powder.

An epoch vs loss graph shows how the loss function of a machine learning model changes over the course of training, which can help to evaluate how well the model is learning. The x-axis represents the number of epochs (one epoch is one full pass through the training dataset), and the y-axis represents the value of the loss function. The graph can provide insights into how quickly

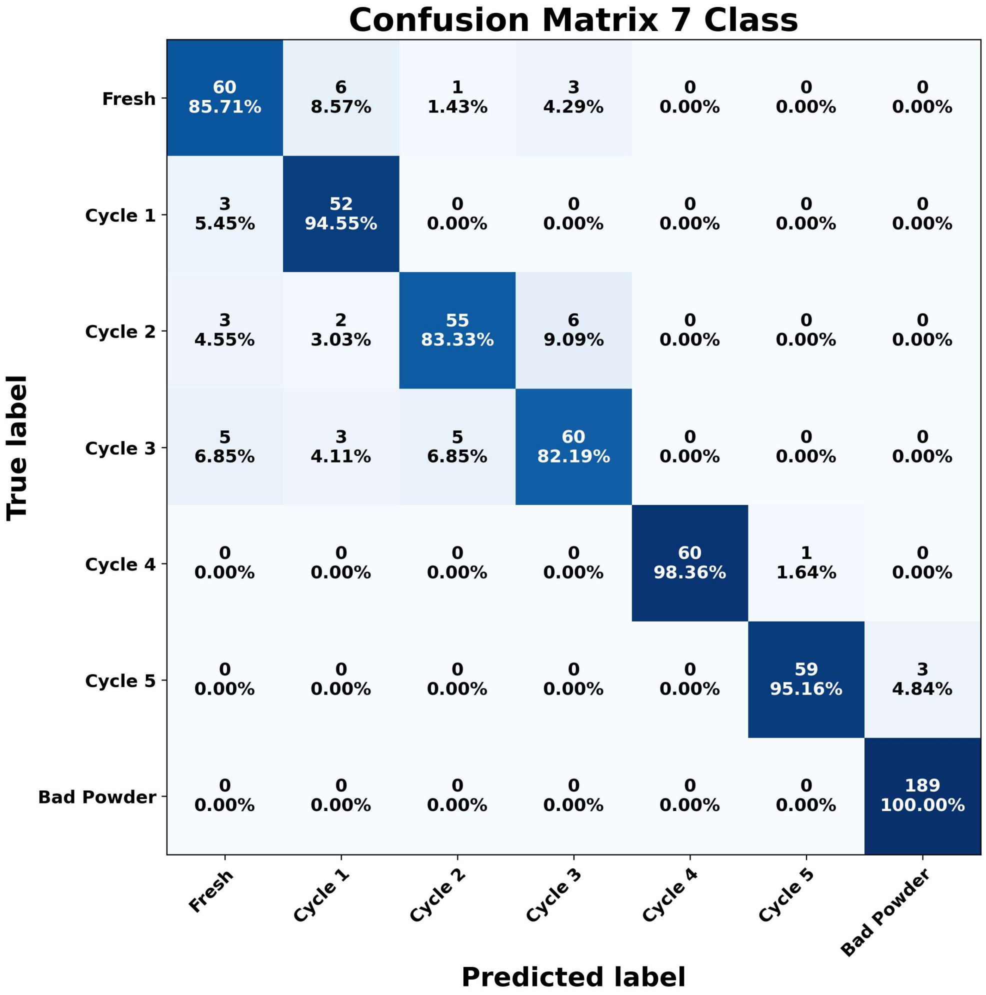

Figure 5.8: Confusion matrix for the results of the testing set for training set 4. Training set 4 has seven classes as shown in Figure 5.5.

the model is learning, whether it has converged to a good solution, and whether it is overfitting or underfitting the training data. Overfitting is indicated if the training set loss is consistently down and the testing set loss is increasing. The final testing set accuracy indicates that these models trained in this work were not overfitted. The epoch vs loss graphs for all of the training set data compositions are provided in Figure5.9. The good vs bad dataset used 12 total epochs and all of the rest used 15 epochs during the training process.

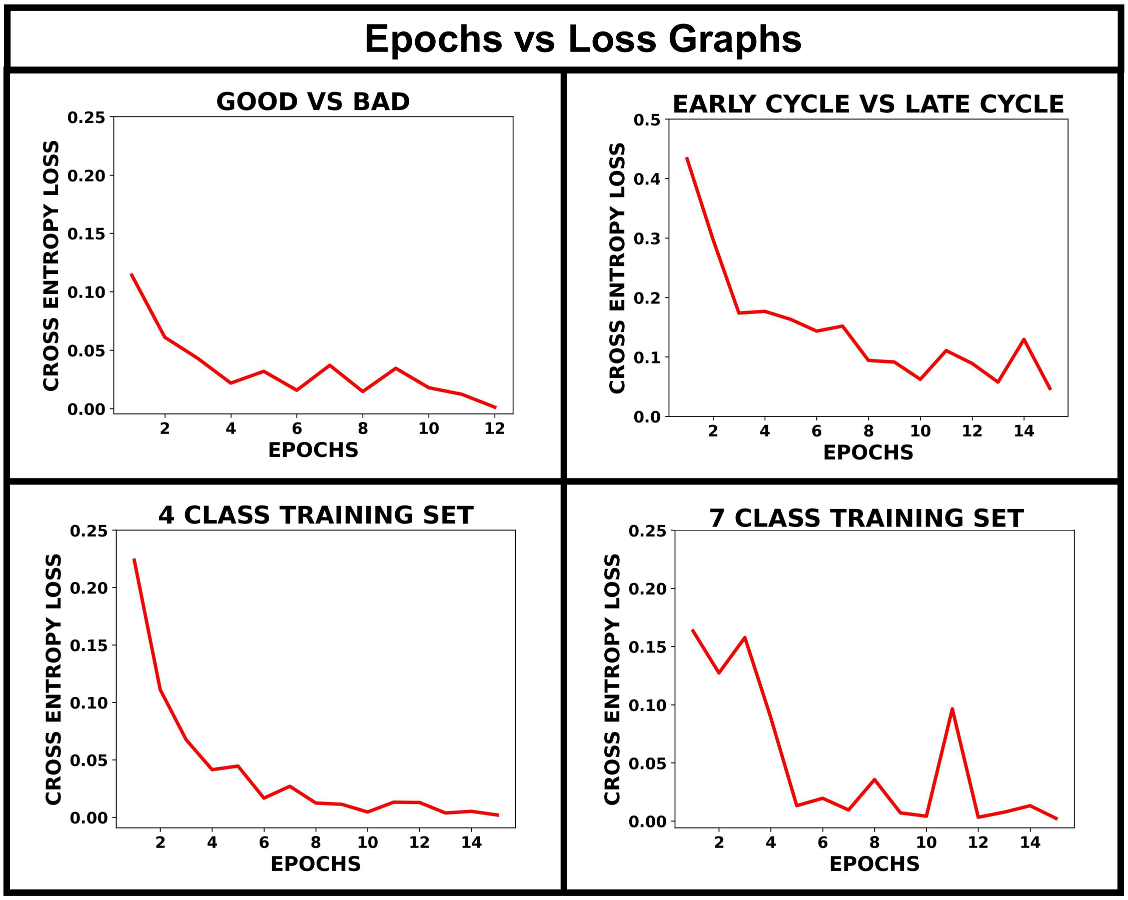

Figure 5.9: Epochs vs Loss graphs for all 4 of the different data set training composition organization methods.

5.6 Conclusion

Key differences were found in the extensive datasets of powder images for laser powder bed fusion printing in different conditions. These differences were present in the preliminary dataset analysis in the form of specific geometric properties such as average area, perimeter, and inverse circularity ratio. The differences in these properties were substantial for "usable" vs "unusable" powder, but much more modest for different iterations of recycled powder. It may be possible to determine the difference between "usable" and "unusable" powder using direct measurements of these geometric properties, but to determine iteration of recycling would not be possible with sufficient accuracy.

The training and implementation of the Resnet18 CNN architecture in this work displayed an ability to classify this powder in several different ways. The powder could be classified as sufficient for printing, classified into multiple categories, or classified based on number of iterations of recycling. This means that although the geometric differences in the powder after each iteration of use, may be very slight, a CNN can still manage to classify this with great accuracy. Because of the black box nature of a CNN, these differences should still be further explored and quantified using traditional methods, but machine learning could be implemented to help give quality engineers additional tools in the qualification of powders for various purposes.

It may be possible that the CNNs trained in this work are picking up clues about the different categories from unseen features that are irrelevant to powder quality. The confusion matrices for training sets 3 and 4 do confirm that they are at least in part picking up some features that are directly based on the features of the powder. The proximity of prediction to recycle iteration confirms that there is some relationship between the recycle iteration count, and how the network chooses to classify a given image. The machine learning models trained in this work can be deployed in the LPBF process to automate quality control of the powder, increase efficiency of the process, and decrease the amount of data required to make these key determinations of powder health.

CHAPTER 6: Martian AND LUNAR BINDER JETTING APPLICATIONS

6.1 Introduction

The prohibitive cost of transporting raw materials from the Earth to either the Moon or Mars is the driving factor for pursuing in-situ resource utilization (ISRU). The lack of oxygen, extreme thermal cycles, solar and cosmic radiation are significant challenges when attempting to construct a base in these harsh environments [107, 108, 109, 110]. Such bases, would most likely be constructed using a variety of materials, architectures and shapes as depicted in Figure 6.1. Among these, and primarily due to their natural abundance, Martian and Lunar regolith would remain the first choice for parent materials. Regolith has also shown promise in it's ability to withstand the thermal cycles and radiation in their respective environments [111, 112, 113]. However, using regolith for construction remains a formidable challenge for ISRU. Several materials in the masonry processing typically done on earth are missing in these harsh and desolate extra terrestrial environments in addition to the environmental conditions themselves [99].

In spite of this, many techniques have been proposed to utilize this material for realistic construction. These include using a brick making process that implemented a polymer material to bind the regolith powder together [114]. Work has been done to focus and magnify solar energy in order to sinter Lunar regolith in a layer by layer fashion [115]. This method is similar to the additive manufacturing method known as Selective Laser Sintering (SLS). Binding methods and materials have also been examined by recent research. Some works have been done that introduced a naturally occurring biopolymer (guar gum) to act as a binding agent [116, 117, 118]. The biopolymer could be potentially grown in situ, and the bricks constructed using this binding agent showed promising results. Some studies have experimented with bricks formed using liquid sulfur[119, 120, 121]. The process is similar to concrete formation, so it is often referred to as "MarsCrete."

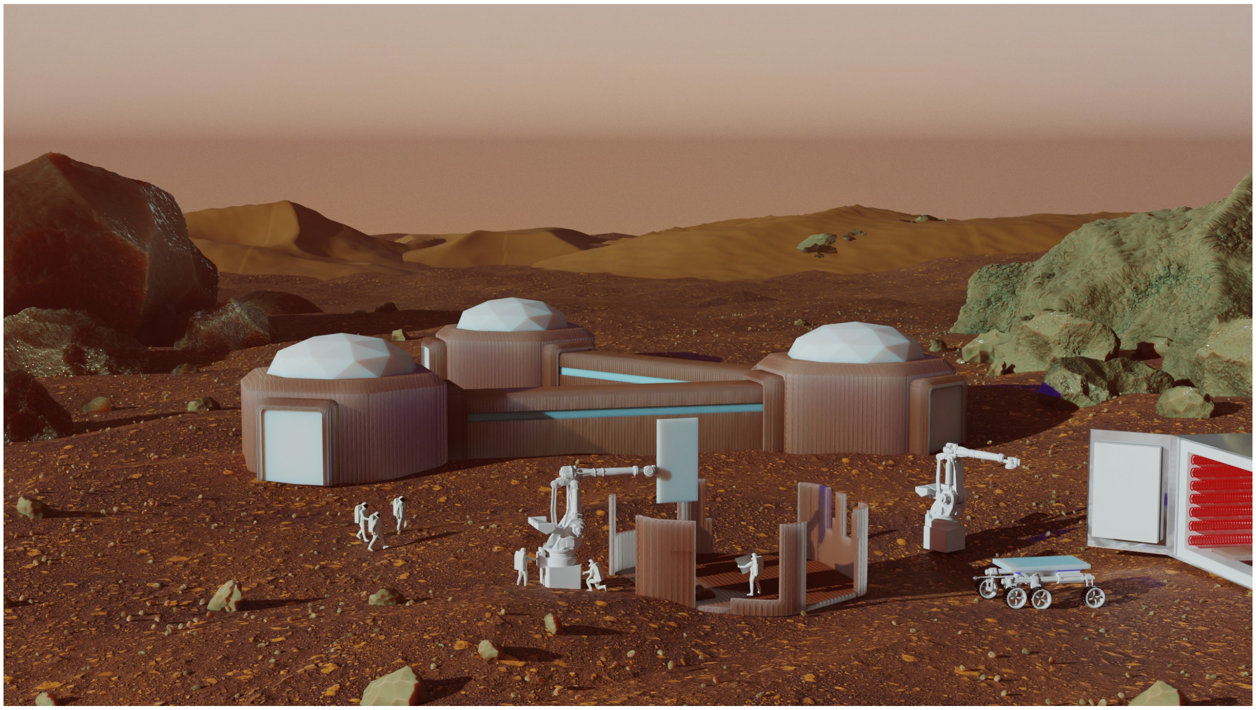

Figure 6.1: Depiction of a concept habitat of a Martian outpost. The outpost shows complexity of shapes and materials that must be constructed using ISRU. Additively manufactured subcomponents can speed up time and reduce energy for assembly procedure that would involve work by astronauts and robots.

All the proposed methods, do require transportation of either raw materials or equipment from earth to complete the proposed manufacturing processes.

These exciting advances suggest the crucial benefit of an organic or inorganic binding material to realize higher quality masonary. More interestingly, such binder materials can also form the basis of extra terrestrial binder jet printing technology (BJT). BJT is an additive manufacturing (AM) method that was developed in the early 1990s and is currently being used to manufacture both ceramic and metallic components [32, 85]. It is now steadily gaining attention due to its versatility. BJT has a less complicated design that does not use any high powered lasers and has demonstrated low cost scalability as a manufacturing platform [122]. The components are manufactured by accurately distributing a binder material onto a powder bed, lowering the powder bed, rolling out a new layer of powder, and then distributing the binder material again [123, 122]. The green part or green state refers the point in the manufacturing process at which the part has been printed but not sintered. This means the particles are only held together by the binder material, so the part is still fragile. After the initial print, the green component must undergo a sintering phase in order to bond the powder material together by reaching near melting temperatures of the powder material.

The selection of an adequate binder is a challenging portion of this endeavor. An optimal binder needs to be both capable of holding regolith together while the component is in the green state, and also would ideally be available in-situ. The simplistic salt water binder proposed in this work, exhibit the necessary qualities that are demanded of a binder solution. Binder material and sintering play a crucial role in BJT's success. More interestingly, other binder based technologies mentioned above can also potentially benefit from sintering since significant densification, which is critical towards high final strength occurs during the sintering process [124]. However, the sintering also causes significant microstructural changes and sample shrinkage. Thus, it has a critical impact on the overall accuracy and quality of the final manufactured product.

Considering this centrality of sintering, this work investigates the effect of sintering temperature on green regolith parts made using a simple yet potentially sustainable salt water binder. The microstructural evolution of Martian and Lunar regolith samples with sintering temperature, shrinkage and strength improvements are reported in detail.

6.2 Materials and Methods

6.2.1 Regolith Simulant

There have been about 400 kg of Lunar regolith retrieved and brought to earth during the apollo missions [125]. There has not currently been any Martian regolith retrieved from Mars, all study has been performed in situ. Therefore the quantity of Lunar regolith is insufficient for significant research and the quantity of Martian regolith is nonexistent [125]. This has driven the need for simulants. There have been around 30 different variants of the Lunar regolith and 40 types of Martian regolith developed [126, 127]. Variations in the regolith could cause variations in the final material properties of any manufactured component. For this work, we will be using MGS-1 (Mars Global Simulant) and LMS-1 (Lunar Mare Simulant) from Exolith labs [128, 129].

MGS-1 was selected as the simulant to be used for our work because is the currently the closest representation of Martian simulant, based on the soil that was analyzed by the Curiosity Rover [128]. The design philosophy behind MGS-1 was to create a regolith simulant that is the closest match mineral and chemical composition of actual Martian regolith. JSC Mars-1 has been used frequently in similar, and is a very close spectral analog match to Martian regolith. This material is mostly composed of volcanic ash from the Island of Hawaii [130]. The Lunar regolith used in this study (LMS-1) was selected because it is good match to the mineral and chemical composition of actual Lunar regolith. LMS-1 also matches some of the irregular shapes and sizes of particles that are found in Lunar regolith. The small irregular sharp particles that are present in Lunar regolith are the result of space weathering over millions of years, which includes meteor impacts, solar wind, and cosmic radiation [131]. Our work implements the regoliths as is, with no powder preprocessing, so the regoliths selected had to be very similar in powder distribution to actual conditions.

6.2.2 ISRU Binder

A pure distilled H_2O mixed with a pure iodized salt is used as the binder material for this study. The ratio of NaCl to H_2O was 1/16 or 6.25% NaCl. A binder material that can be found in-situ is optimal. A salt-water solution has not been implemented as a binder material in any of the previous works reviewed by the authors of this study. Salts have been found preserved in the rocks and soil on Mars, from when the planet was wetter [132]. Sodium is less prevalent on the Moon, but trace amounts have been detected in the regolith [133]. Water deposits have recently been reported on both Mars and the Moon, although accessing the water would be challenging [134]. The salt-water binder examined in this work is a simplistic and effective ISRU material. Retrieval of salt and water in an extraterrestrial environment would certainly have challenges, and is not the focus of this work. Any material that has the potential to be harvested in-situ should be receive adequate consideration and study as a potential candidate for construction materials.

6.2.3 Manufacturing method

The manufacturing method in this work will be injection molding. The molding itself was made from 3D printed PLA components, which are cylindrical in shape. The regolith is mixed with the salt water binder prior to being placed into the PLA printed molds. The regolith mixture is not compressed into the mold, just packed gently into it. Injection molding is a good replication of the binder jet printing method. It is a good replication because the green part is composed of binder and powder for both binder jetting and injection molding.

6.2.4 Molding Method

The samples were molded using 3D-printed molds out of a thermoplastic. The molds were 3D-printed on an Ultimaker S5 ®. A Tough PLA material of the translucent color was used for the molds. The samples made were cylindrical in shape and had a length of 1 inch and a diameter of 0.5 inch. The PLA 3D-printed molds can be seen in the bottom half of Figure 6.2. They have two components one is the cylindrical molds which were 3D-printed in two halves. The other is the base plate which can hold the two halves of the cylindrical mold in a secure fasion. The regolith and binder mixture can then be added to create the desired cylindrical shape.

The binder material was made from pure distilled water and pure iodized salt. The ratio of NaCl to H_2O was 1/16 or 6.25% NaCl. The addition of salt to the water made a noticeable difference in the binding of the material together. An attempt was made to produce these samples with just water, and it failed. During extraction from the PLA molds, the regolith cylinders would crumble apart. The addition of salt to the water made the extraction of the samples from the molds much easier and held the regolith together for both the Martian and Lunar versions quite well.

The regolith and binder ratio was 3.5 parts regolith to 1 part binder. This was selected from observation of the stability of the green part. If too much binder liquid is added the sample will collapse. Also if there is too little binder liquid added the sample will be too brittle and crumble. The regolith and binder mixture was loosely packed into the molds to mimic the behavior of the BJT printing method. They did not sit to allow the water to evaporate either. Immediately after packing the regolith and binder mixtures into the molds they were then extracted and the sintering process was initiated. The same conditions were applied to both the Lunar and Martian regoliths in order to create the data that could be compared upon completion of the manufacturing process.

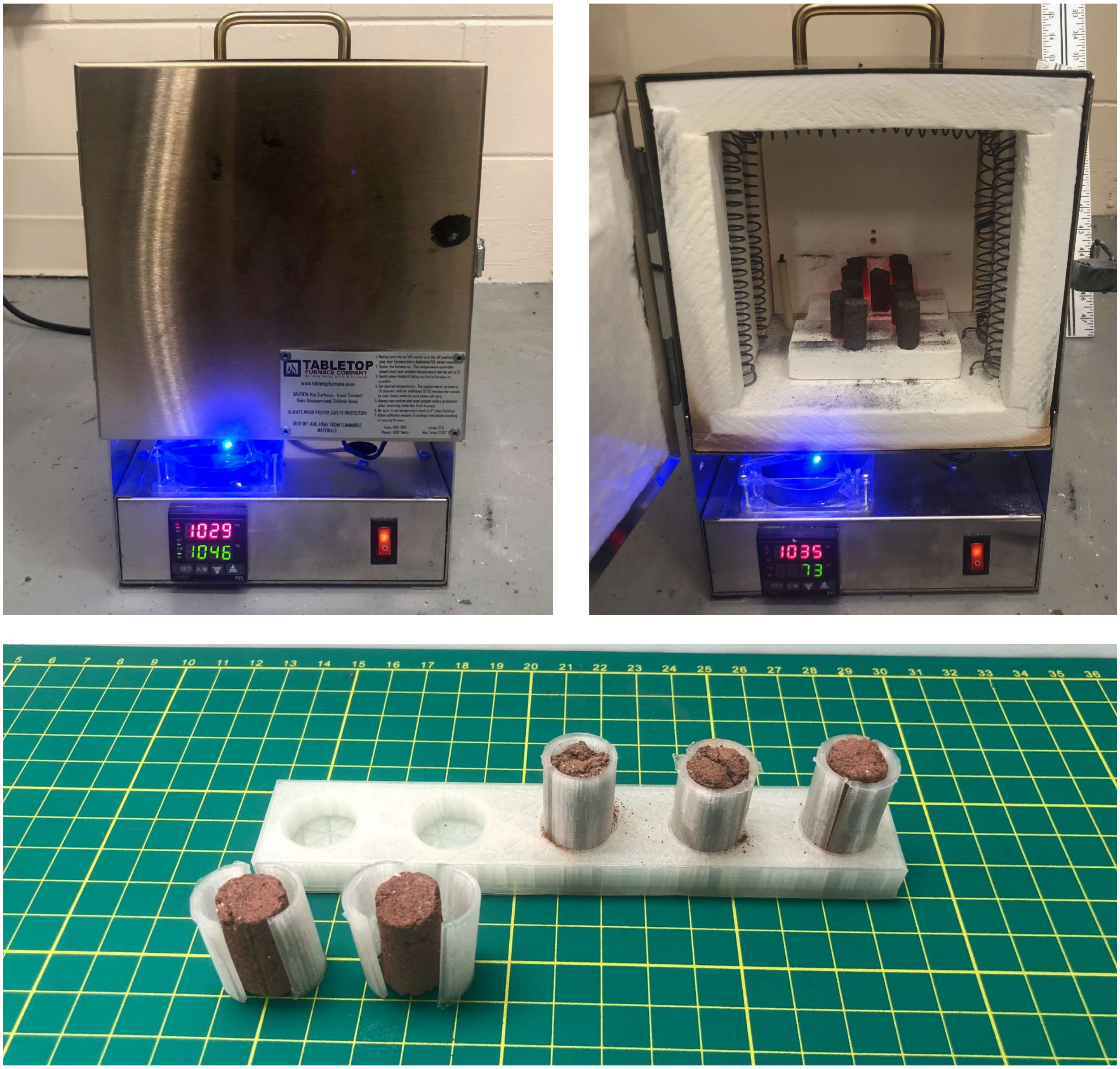

Figure 6.2: (Top Left) Sintering oven used for in operation, closed and latched shut (Rapidfire Standard Pro I ®). (Top Right) Oven opened after sintering a set of samples placed on Alumina pads. The oven is heated via two electical heating coils that run along the sides and top of the sintering oven.(Bottom) Photograph of the cylindrical samples in the 3D-printed halved cylindrical shell PLA molds. The samples are composed of MGS-1 Martian regolith and the binder material is salt water solution. The cylindrical molds are 0.5 inch in diameter and 1 inch in height. The grid line spacing is 1 centimeter.

6.2.5 Sintering Protocol

The sintering oven used to sinter the samples, is manufactured by the Tabletop Furnace Company and the model is the Rapidfire Standard Pro I ®. The furnace has a maximum temperature of 1200°C. The oven has 0.2% accuracy over the entire input range of the furnace. This furnace has two induction coils that run the full length of the sides and top of the furnace. This can be seen in the top half of Figure 6.1. The samples were placed on alumina blocks during the sintering procedures. All of the samples were pre sintered directly after the molding process. The presintering was performed at 200°C for a total of 1 hour. After completion of the presintering step, the samples were then sintered at high temperatures. The Martian and Lunar sintering conditions were again kept consistent with each other. A total of 15 samples were molded using the aforementioned molding methods. The 15 samples were split into groups of 5 after the presintering was completed. 5 samples were sintered at 1000°C for 1 hour, 5 samples were sintered at 1100°C for 1 hour, and 5 samples were sintered at 1200°C for 1 hour. Again this conducted for both Martian and Lunar regolith samples, creating a total of 30 samples. The heating ramp rate for both the presintering and sintering was 25°C per minute. The cool down was just completed by turning the oven off and allowing the temperature of the surrounding environment to bring the temperature of the oven back down. The cool down was relatively rapid and took about 10 minutes.

6.2.6 Material Testing

The material was tested on an MTS machine following the ASTM C1314 - Standard Test Method for Compressive Strength of Masonry Prisms [135]. The tensile test machine was an MTS Criterion Model 43, and the load cell was a 50 kN load cell model LPS504 C. The displacement rate of the compression pad was 0.2mm per second. Each of the samples were tested giving a sample weight of 5 to each category. The compression modulus was calculated for the samples sintered at 1200°C, and will be given in the results section. The samples that were sintered at 1000°C and 1100°C were too brittle to have a compression modulus of any significance. The material would fail under a relatively small load. The compression modulus testing set up is shown in Figure 6.3. This image was captured after the compression was performed to illustrate how the sample failed.

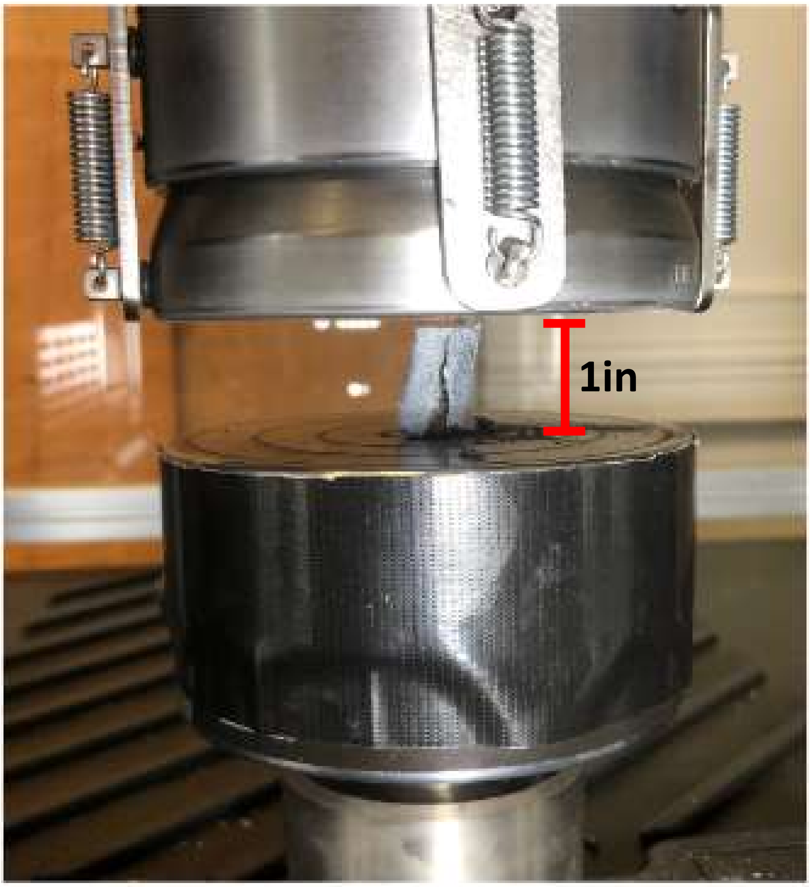

Figure 6.3: Experimental set-up for the compression testing for the sintered Martian and Lunar Regolith samples. The sample was painted white and then black dots were applied to make it possible to apply DIC measurements. The image was taken after failure of the sample had occurred. There is black duct tape on the lower compression pad to help prevent glare, which effects the DIC system.

6.2.7 Digital Image Correlation

Digital Image Correlation (DIC) was only performed on the samples sintered at 1200°C. The samples sintered at this temperature were more smooth and had less texture than the pre-sintered samples. The samples were painted with white and black spray paint to create speckle pattern on the samples to provide features for the Digital Image Correlation (DIC). This is often referred to as the speckle pattern. The DIC system was Dantec Dynamics Q-400 Digital 3D Image Correlation System. The DIC measurements provide a full 3D view of the strain map of the samples while they were under applied compressive load. 3D DIC was selected because the samples are cylindrical, therefore the curvature of the cylinder can be examined more in depth with the 3D method.

The compression pads are metal and the lights used for DIC are very bright and the glare affect the data gathered from the camera. Then, the tape on the compression pad seen in Figure 6.3 was put there to prevent the glare from affecting the DIC cameras. The DIC system used was a two camera setup with Dantec Dynamics software. The facet size was 19 pixels, the accuracy was 0.3 pixels, the residuum was 35 gray value, the 3D residuum was 0.4 pixels, and the grid spacing was set to 15 pixels, which equates to 1.1mm for the given camera resolution. Most of the values here are standard practice, except for facet size and grid spacing. These values are standard practice, but require a little optimization. Facet size was varied from 15-21 pixels and grid spacing was varied from 12-18. The DIC generated strain map which covered the specimen the most was selected.

6.2.8 Microstructure Inspection

At every stage of the manufacturing process the material was examined under a microscope. The examinations took place at the powder stage, after the molding phase, and after the sintering phase. The microscope used was a Keyence VHX-900F ®. Images were taken at 10X and 200X magnification. The 10X magnification gives a view of the entire top of the sample, and the 200X magnification provides a view of the particles that the samples are comprised of. The images will be given in the results section.

6.3 Results and Discussion

6.3.1 Microstructure Images

Digital images were gathered at both 10X magnification and 200X magnification using the Keyence VHX-900F ®. In Figure 6.4, we can see the top view of all of the samples. These images were recorded at 10X magnification. In this image, we can see both the Lunar and Martian samples at the green state, sintered at 1000°C, 1100°C, and 1200°C. The images show a very clear distinction between sintering at 1200°C and the other two lower temperatures for both the Martian and Lunar samples. The difference in coloring between the 1000°C and 1100°C is not substantial.

The images that were taken at 200X magnification display the rocky mixture of the composition very well. The images of the Lunar samples at 200X magnification are shown in Figure 6.5. In Figure 6.5, the powder state, the green state, and the three different sintering conditions are all displayed. These states are shown in the same order for the Martian samples in Figure 6.6. The temperature sintering conditions applied were one hour of at either 1000°C, 1100°C, and 1200°C. This was completed directly after the presintering portion of the cycle. Again we clearly see the distinction of sintering samples at the temperature of 1200°C. The 1200°C sintered image shows a glassy encasement of rocky particles. These samples also felt smooth and glass like to touch for both the Martian and Lunar samples.

In Figures 6.5 and 6.6 we can also observe the comparison between Lunar and Martian (respectively) regolith samples in the powder form (A) and in the green state (B). The green state is the

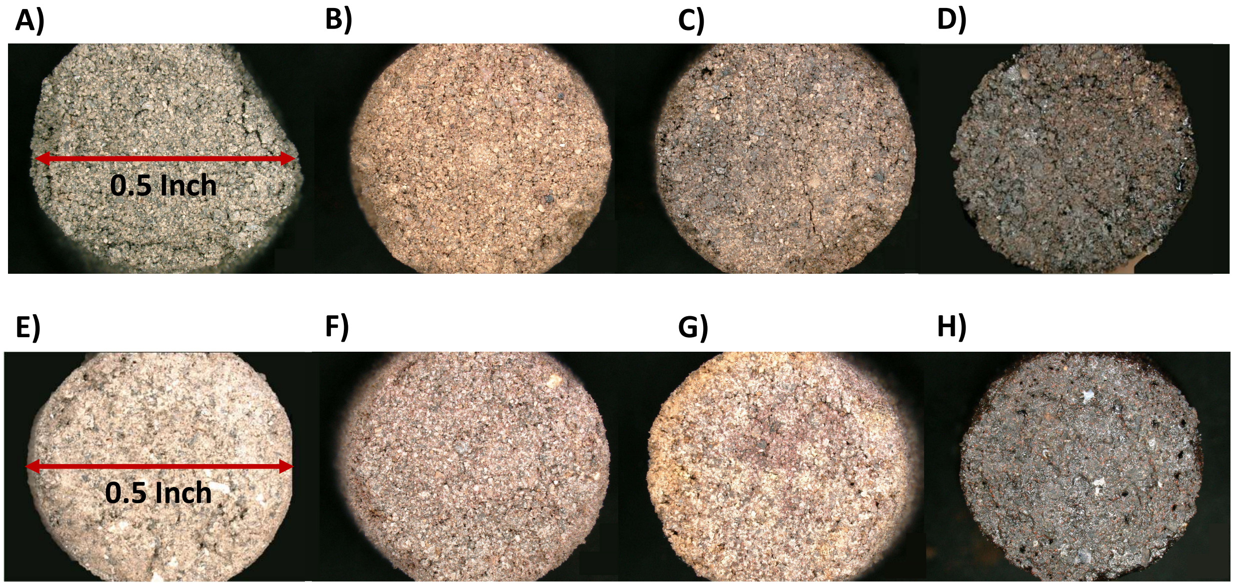

Figure 6.4: Microscopic images of the top view of the cylindrical regolith brick samples at 10X magnification: (A) Lunar prior to any sintering (green). (B) Lunar sintered for 1 hour at 1000°C. (C) Lunar sintered for 1 hour at 1100°C. (D) Lunar sintered for 1 hour at 1200°C. (E) Martian prior to any sintering (green). (F) Martian sintered for 1 hour at 1000°C. (G) Martian sintered for 1 hour at 1100°C. (H) Martian sintered for 1 hour at 1200°C.

state at which the binder material was mixed with the powder, but no sintering has occurred yet. The comparison between the powder state and the green state shows how the binder material is able to hold the regolith together. The salt water binder and smaller regolith particles combine to form a bonding agent and hold the larger regolith particles together. The binder material used was a 6.25% salt-water solution, as explained in Section 6.2.4. A more significant green state bond could be formed if the powder material was composed of smaller and more uniform particles. This could be achieved by using a milling machine on the powder prior to addition of the binder material.

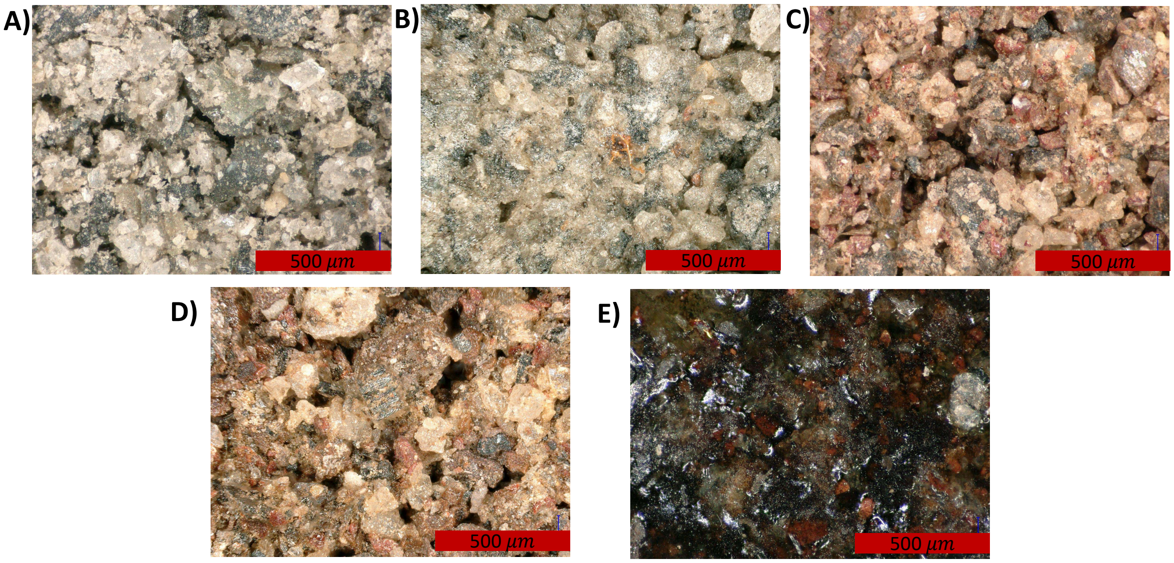

Figure 6.5: Microscopic images of the Lunar samples collected at 200X magnification: (A) Lunar sample during the green state, after molding, prior to sintering. (B) Lunar sample sintered for 1 hour at 1000°C. (C) Lunar sample sintered for 1 hour at 1100°C. (D) Lunar powder prior to any sintering or molding. (E) Lunar sample sintered for 1 hour at 1200°C.

6.3.2 Compression Testing

Compression testing was performed on all of the sintered samples. A total of 5 measurements were taken for each regolith and sintering category. All of the samples went through a curing portion directly after being molded which was 200°C for one hour. The samples were tested at this stage as well. After being sintered at 200°C for one hour the samples were sintered for another hour at either 1000°C, 1100°C, or 1200°C. All of the numerical data is available for the shrinkage and the compressive properties in Table 6.3.2. A graph that compares the compressive strength of the various sintering paths is shown in the top bar plot in Figure 6.7. The samples sintered at 1000°C and 1100°C did not achieve a very high compressive strength. The compressive strength increased by about 15 MPa for the samples sintered at 1200°C for both the Martian and Lunar samples.

The Martian samples had a slightly higher compression modulus and compressive strength than the

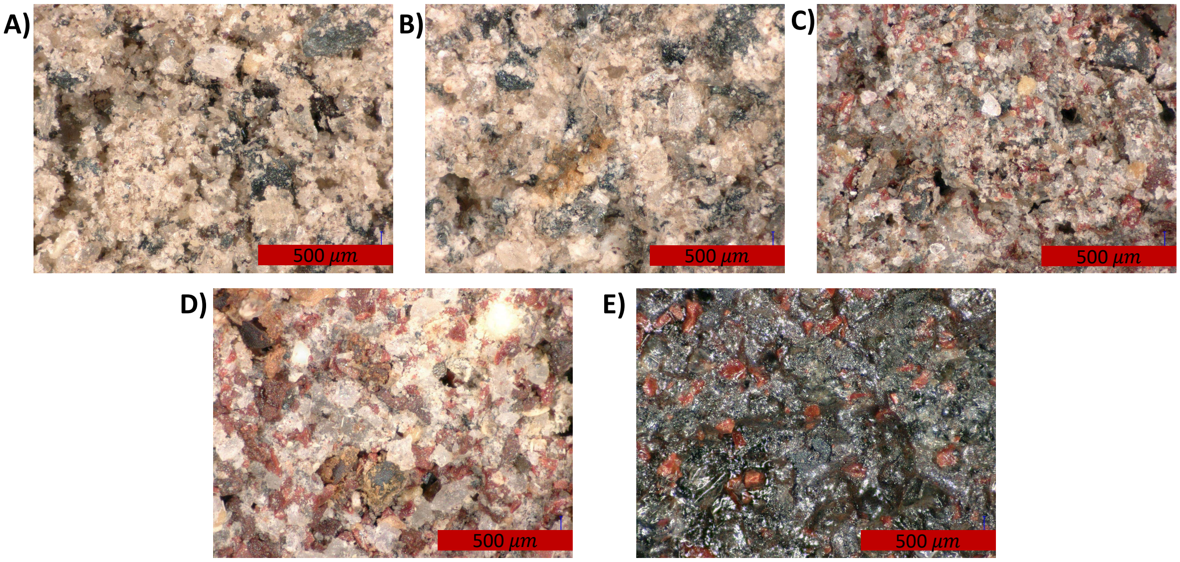

Figure 6.6: Microscopic images of the Martian samples collected at 200X magnification: (A) Martian sample during the green state, after molding, prior to sintering. (B) Martian sample sintered for 1 hour at 1000°C. (C) Martian sample sintered for 1 hour at 1100°C. (D) Martian powder prior to any sintering or molding. (E) Martian sample sintered for 1 hour at 1200°C.

Lunar samples. These values (for both the Martian and the Lunar samples) are in a similar range to that of brick, if not slightly higher. Brick has an compressive strength of around 6 MPa - 82 MPa [136, 137, 138]. This would indicate that this material is a suitable material for construction of load bearing structures.

As mentioned in the introduction, other researchers have looked into the mechanical properties of in situ extraterrestrial constructed samples. In Table 6.3.2 the values are given for the compressive strength of some of the previous manufacuring methods used. The focused solar ray method was similar to using a laser to raster across a powder bed in a layer by layer fashion [115]. This was a proven, direct 3D printing method. Lunar concrete and sulfur Lunar concrete both showed promising results, the sulfur-based has more materials available in situ [139, 140]. One study compared samples sintered in air at 1100°C for 3 hours and in a vacuum at 1125°C for 3 hours[141]. No binder was used for this study, but the samples were pre-pressed at 255 MPa in a 20-mm diame-

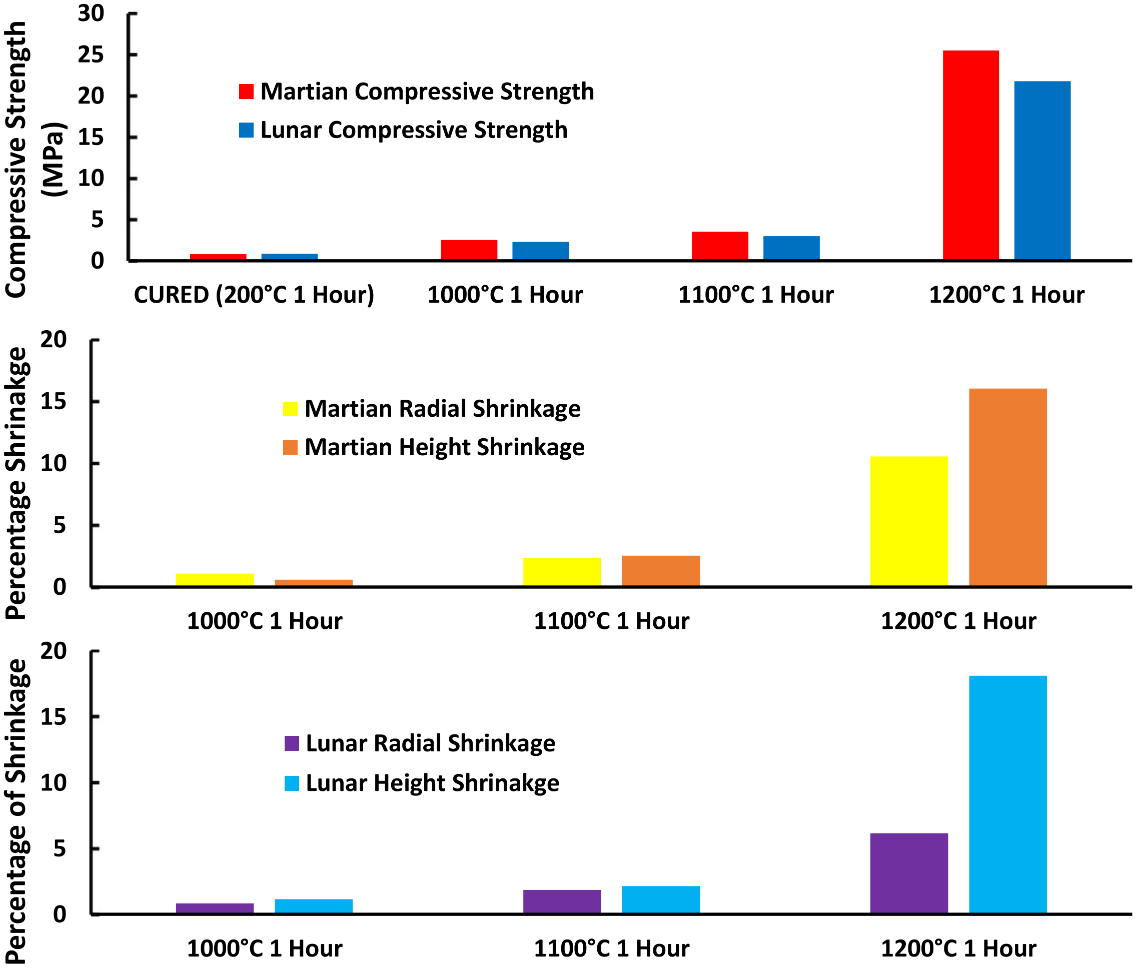

Figure 6.7: (Top) Bar graph that compares the average compressive strength of the Martian and Lunar samples after curing (200°C), 1000°C sintering, 1100°C sintering , or 1200°C sintering.(Middle) Bar graph that compares the average radial and height shrinkage that occured at the different sintering profiles for the Martian samples.(Bottom) Bar graph that compares the average radial and height shrinkage that occured at the different sintering profiles for the Lunar samples.

ter die. Another method performed successful D-shape 3D printed of a Lunar regolith[142]. The method used in this work did not pre-compact our samples and the powder was not milled either. The powder was used directly as is, and the binder material was a simple salt-water solution.

The Martian regolith used in this work was also not pre-pressed or milled prior to sintering. The regolith was used as is, and the binder was a simple-salt water solution. Other works that have

Table 6.1: Material properties of sintered Lunar and Martian samples.

	Martian Sample	Lunar Sample
1000°C Radial Shrinkage Percentage	1.06%	0.84%
1000°C Height Shrinkage Percentage	0.57%	1.16%
1100°C Radial Shrinkage Percentage	2.34%	1.85%
1100°C Height Shrinkage Percentage	2.52%	3.15%
1200°C Radial Shrinkage Percentage	10.54%	6.17%
1200°C Height Shrinkage Percentage	16.03%	18.13%
1200°C Compression Modulus	67.80 MPa	55.73 MPa
1200°C Compressive Strength	25.46 MPa	21.73 MPa
1100°C Compression Modulus	10.17 MPa	9.06 MPa
1100°C Compressive Strength	3.52 MPa	2.94 MPa
1000°C Compression Modulus	8.06 MPa	6.56 MPa
1000°C Compressive Strength	2.51 MPa	2.25 MPa
Cured Compression Modulus	5.54 MPa	5.34 MPa
Cured Compressive Strength	0.78 MPa	0.83 MPa

Table 6.2: Comparison of Compressive Strength of Lunar Materials

Manufacturing Technique	Regolith Composition	Compressive Strength
Focused Solar Ray Sintering [115]	JSC-1A	2.31 MPa
Lunar Sulfur Concrete [139]	35% Sulfur 65% JSC-1	31 MPa
Lunar Concrete [140]	1.75:1.0:0.485 (JSC-1:Cement:Water)	74 MPa
1100°C Vacuum 3 hour [141] Dry Pressed at 255 MPa	JSC-1A No Binder	152 MPa
1125°C Air 3 hour [141] Dry Pressed at 255 MPa	JSC-1A No Binder	98 MPa
D-Shape 3D Printing [142]	DNA	20 MPa
1200°C Air 1 hour	1:3.5 (Salt-Water:LMS-1)	21.73 MPa
Standard Brick	Clay or Shale	6-82 MPa

used various methods to produce and test Martian brick samples are seen in Table 6.3.2. A lot of work has been done into the feasibility and ultilization of the Martian concrete formed from liquid sulfur [119, 120, 121]. One work did sinter at 1130°C for 10 hours, and showed a very high compressive strength. The work did mill the regolith for 48 hours prior to sample manufacturing, and also filtered so that all particles were between 25 and 50 μm. A dry pressed sample at 70 MPa

Table 6.3: Comparison of Compressive Strength of Martian Materials

Manufacturing Technique	Regolith Composition	Compressive Strength
Dry Pressed 70 MPa 3 min [143, 124]	MGS-1	1.64 MPa
Layerwise Slurry Deposition [143, 124]	MGS-1:Proprietary Binder	30.8 MPa
Sintered at 1130°C for 10 hour [144] Powder was milled 48 hours	51:49 (Weight) JSC-Mars-1A powder:Water	51 MPa
Sulfur Martian Concrete [119]	50:50 (Volume) Sulfur:MGS-1	54.4 MPa
1200°C Air 1 hour	1:3.5 (Volume) Salt-Water:MGS-1	25.46 MPa
Standard Brick	Clay or Shale	6-82 MPa

for 3 minutes has been done [144]. Also a layerwise slurry deposition method was developed with good success, the component was sintered at 1150°C for 3 hours[124]. The binder material was proprietary. All of the reviewed research show a compressive strength range from about 1 MPa - 200 MPa, with the majority falling under 50 MPa. The values found in this work are in agreement to the values found in other research. The small variance among the research out there is a result of differences in the manufacturing method. Our simplistic approach achieved a compressive strength that is in the same range as common brick used in terrestrial applications[136].

6.3.3 Digital Image Correlation

DIC (Digital Image Correlation) was implemented in this work to obtain real-time strain maps, as the compressive force was being applied to the samples. The failure mechanism of the samples (both Lunar and Martian) was the formation and rapid propagation of a vertical crack. The crack propagated through the samples leading to a complete failure in less than 0.2 seconds. This occurred between 2 and 3 percent engineering strain for all of the samples sintered at 1200°C (both Martian and Lunar).

In Figure 6.8, we can see 5 DIC images for one of the Lunar samples sintered at 1200°C. These

DIC images show the strain pattern directly before failure of the sample. The regions of high strain are in a straight vertical line, beginning at the top of the samples. These high strain regions caused the crack to initiate and propagate down the sample very rapidly (<0.2s). This is an indication that the material is a brittle material and underwent a axial splitting brittle material failure [145]. The engineering strain percentage is plotted against stress (MPa) at the top of Figure 6.8. There are red dots the are marked on this plot which correlate to the exact times that the DIC images were taken. The same figureis provided for a Martian sample sintered at 1200°C in Figure 6.9.

In this case, the Martian sample also failed from a vertical crack formation, which also propagated through the sample very rapidly (<0.2s). There are also red dots on the stress-strain curve to correspond with the time that DIC images were taken. The formulas for engineering stress and engineering strain are given in Equations 6.1 and 6.2 respectively. The engineering strain can be represented as a percentage by multiplying by 100, and this is how it is represented on the X-axis of Figures 6.8 and 6.9

$$\sigma_{eng} = \frac{F}{A_0} \tag{6.1}$$

$$\varepsilon_{eng} = \left| \frac{L - L_0}{L_0} \right| \tag{6.2}$$

A brittle material cylinder will fail in either shear or a columnar direction or a combination of the two when receiving a sufficient compressive force. No cracks formed in the shear direction, all cracks formed parallel to the force applied (vertical through the length of the cylinder). This could be due to the shape of the particles in the regolith, as they were not preprocessed in any way. Another possibility is the rounded tops of the samples. It was also recorded that there was more shrinkage in the vertical direction during sintering, for both the Martian and Lunar samples. This

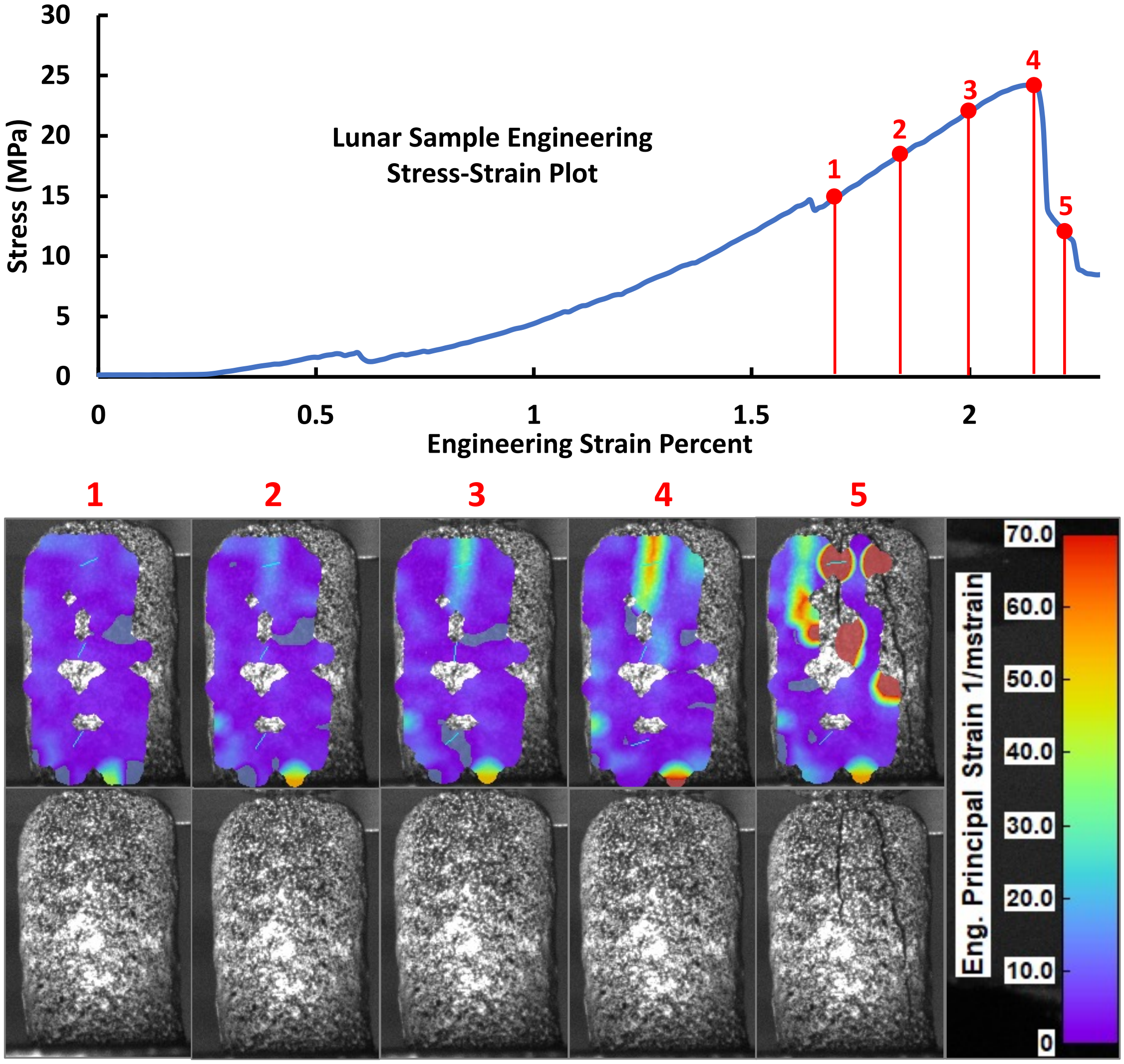

Figure 6.8: (Top) Engineering strain percentage plotted against stress for a Lunar sample. (Bottom) 5 DIC images that correspond to the red dot indicated on the stress strain curves above. The principal strain is shown on the DIC images in millistrain. Below the DIC images are the actual images in black in white. The DIC images were selected just before and during failure.

is caused by the gravitational force that is applied during sintering. It is possible that this leads to anisotropic properties in the samples.

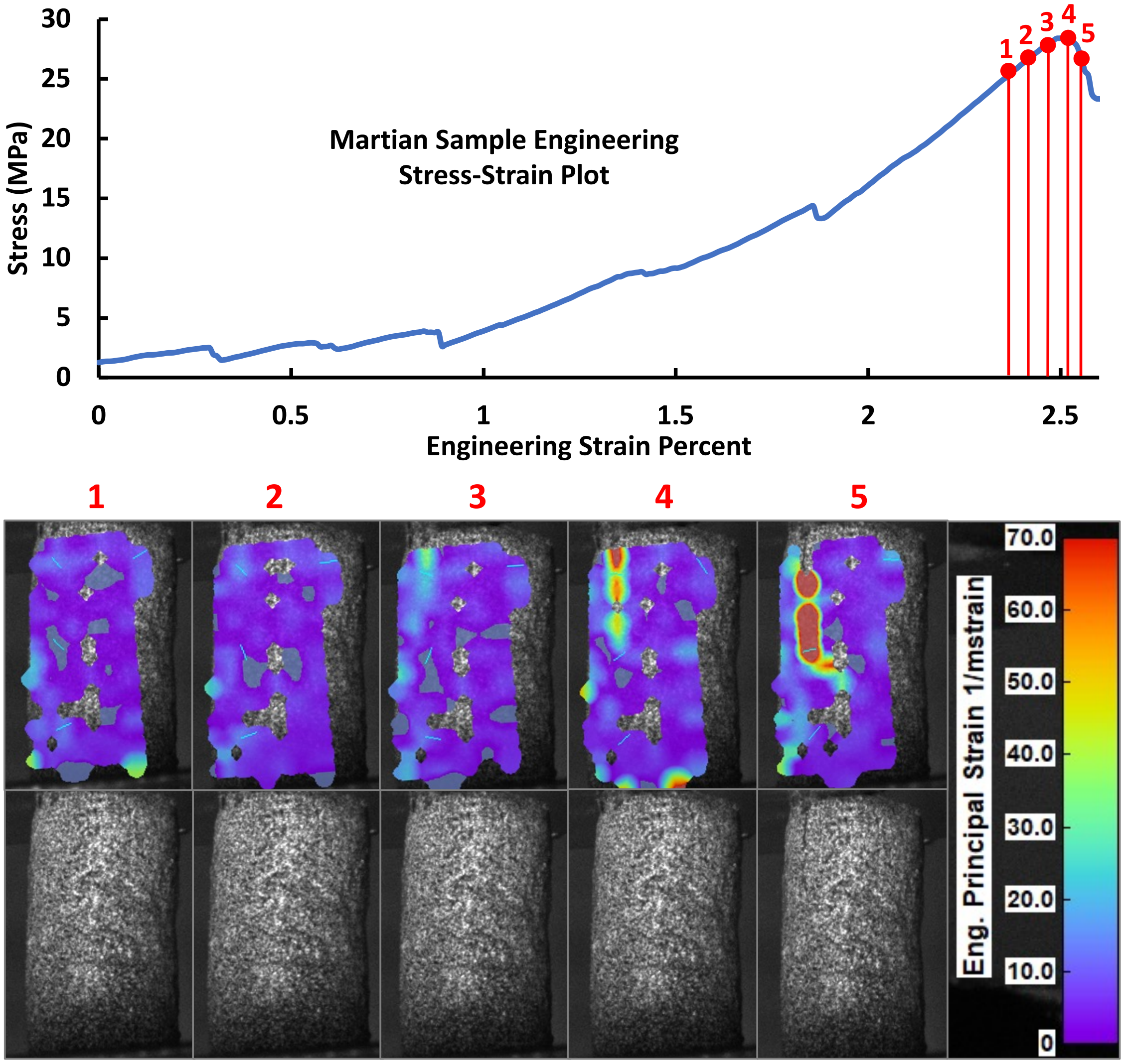

Figure 6.9: (Top) Engineering strain percentage plotted against stress for a Martian sample. (Bottom) 5 DIC images that correspond to the red dot indicated on the stress strain curves above. The principal strain is shown on the DIC images in millistrain. Below the DIC images are the actual images in black in white. The DIC images were selected just before and during failure.

6.3.4 Shrinkage Behavior

The shrinkage was calculated for all of the samples before and after sintering. This measurement was completed with digital calipers. There was negligible shrinkage for the samples sintered at

1000°C and 1100°C (about 1% - 2% in both directions). There was however a significant amount of shrinkage in both the radial and vertical directions for the samples sintered at 1200°C. These values are reported in Table 6.3.2. The values are also plotted in the middle and lower plots in Figure 6.7. The Lunar samples sintered at 1200°C experienced more shrinkage in the vertical direction than the Martian samples sintered at the same conditions. The Lunar samples sintered at 1200°C also experienced less radial shrinkage than the Martian samples sintered at the same conditions. All of the samples were sintered standing straight up, as seen in the top half of Figure 6.2.

The dimensional shrinkage reported in this work has a statistical weight of 5 for both the Lunar and Martian samples at each sintering condition, because 5 samples were manufactured at each condition. If this material is to be additively manufactured via BJT the shrinkage behavior has to be accurately predicted prior to sintering and scaled up accordingly. This is already a common practice in BJT additive manufacturing for both metallic and ceramic parts [146, 84]. Shrinkage in each direction must be accurately predicted. It is clear from this work that inequalities between vertical and horizontal shrinkage were significant for both the Martian and Lunar samples.

6.3.5 Mineral Composition

The mineral composition that is found in the regolith is shown for the LMS-1 simulant in Table 6.3.5 and for the MGS-1 simulant in Table 6.3.5 [128, 129]. A full chemical and mineral composition of the simulants is available on the Exolith Labs simulant website [147]. Pyroxene, plagioclase, and anorthosite are fusible minerals, and olivine is not [148]. It has been shown in previous research that an increase in plagioclase and anorthosite will increase the melting temperature. It was also shown that an increase in pyroxene will decrease the melting temperature [148]. Our study shows this same pattern. The Lunar simulant had a lower melting point in our study. The

Lunar simulant had more pyroxene content than the Martian simulant. The Lunar simulant also had less anorthosite than the Martian simulant had. The Martian simulant also has more plagioclase.

All of these factors are in agreement as the sintering shrinkage measurements confirm the Lunar simulant had a lower melting point. The Lunar samples underwent more vertical shrinkage during sintering than the Martian samples. The Lunar samples contain about 10% more pyroxene than the Martian samples. The Martian samples contain about 8% more plagioclase than the Lunar has in anorthosite.

Table 6.4: Lunar Simulant LMS-1 Mineral Composition

Component	Wt.%
Pyroxene	32.8
Glass-rich Basalt	32.0
Anorthosite	19.8
Olivine	11.7
Ilmenite	4.3

Table 6.5: Martian Simulant MGS-1 Mineral Composition

Component	Wt.%
Plagioclase	27.1
Glass-rich Basalt	22.9
Pyroxene	20.3
Olivine	13.7
Mg-sulfate	4.0
Ferrihydrite	3.5
Hydrated silica	3.0
Magnetite	1.9
Anhydrite	1.7
Fe-carbonate	1.4
Hematite	0.5

6.4 Conclusion

This study has shown that both Martian and Lunar regolith have the potential to be implemented in an additive manufacturing method referred to as binder jetting. The binder material used in this work was a 6.25% salt water solution by volume, and it held the material together adequately. The regolith simulants did not undergo any preprocessing procedures for this study, allowing for a more uncomplicated implementation. After sintering it was found that the compressive strength and compressive modulus of the Martian samples was slightly higher than the Lunar samples. The compressive strength and compressive modulus of both the Lunar and Martian samples was found to be in the range of brick, which indicates that the material is capability for the construction of load bearing structures. The material failure mode and stress strain behavior showed that the material is brittle and ceramic, for both the Lunar and Martian samples. The DIC data also showed sudden catastrophic failure in the form of vertical crack formation and rapid propagation. A BJT method of additive manufacturing could be implemented in either a Martian of Lunar extraterrestrial environments. The final printed and sintered components would be well suited to laying foundation, erecting structures, and fabricating miscellaneous components.

It was also determined that the most optimal sintering temperature is somewhere between 1100°C and 1200°C. The shrinkage was around 15% - 20% in the vertical directions and 5% - 10% in the radial direction when sintered at 1200°C. Most of the shrinkage during sintering occurred between the temperatures of 1100°C and 1200°C. The Lunar samples did undergo more shrinkage and deformation during sintering, this indicates a lower sintering temperature will be required for the Lunar samples for optimal properties. The Martian material had a slightly higher compression modulus and compressive strength than the Lunar material under the given manufacturing conditions. This is the result of differences in the mineral composition of the regoliths.

The microstructure of the samples was also analyzed via microscope at each of the manufacturing stages. After it was determined that water alone would not work as a binder material for either Martian or Lunar regolith, a 6.25% salt-water solution was used. The bond that occurred between the particles in both powders was seen to be driven primarily by the smaller particles (less than 50 microns). This mixture of binder and small particles is what holds the larger particles together. It would be beneficial to explore the effect of milling the regoliths (both Martian and Lunar) prior to manufacturing to decrease the average size of the particles that make up the powder. It is also seen that the samples that were sintered at 1200°C are very smooth in texture and appearance. This work also confirmed previous findings that showed that an increase in pyroxene content can decrease the melting temperature, and that an increase in anorthosite or plagioclase will increase the melting temperature.

The cost of transportation of earth based materials is astronomically higher than simply utilizing materials that are readily available in these environments. The need for adaptive manufacturing in these challenging environments is critical to design and construct habitats capable of housing equipment and possibly people. This need can be met through the implementation of additive manufacturing techniques. The development of additive manufacturing methods which utilize materials found in such environments would greatly assist in the exploration and establishment of settlements in these unforgiving environments. Additive manufacturing provides much needed versatility in an extraterrestrial setting. The ability to manufacture components rapidly to solve challenges that may arise on the Moon or on Mars is vital to ensuring success of such formidable endeavors.

CHAPTER 7: SHRINKAGE PREDICTION FOR METALLIC ADDITIVE MANUFACTURING

7.1 Introduction

Effective predictive models for shrinkage during sintering would provide an immediate benefit to a myriad of industries. High temperature ceramic and metallic materials typically have to go through a sintering phase during manufacturing [149]. The conditions of the sintering oven will have a direct effect on the final dimensions and final properties of the component of interest [46]. Sintering models have been a desire of industry for almost a century and that desire will continue to grow. Additive manufacturing methods will require more sintering models than the traditional injection methods. This requirement is the result of a substantial increase in the amount of key variables to an already untenable equation [149].

Over the years, academic research has focused on several different avenues for researching sintering simulations. In the 1960's research was predominantly focused on the interaction between two particles in contact with one another during sintering. A neck will form in this region connecting the two particles [46]. The problem is fascinating from an experimentation and modeling perspective, but has little application to industrial needs. Throughout the 1970's and 1980's, research was more focused on one-dimensional shrinkage and prediction of density [46]. This period of research was tailored more to industrial needs, but still industries were unable to leverage this research for comprehensive modeling for shrinkage prediction. The 1990's was filled with finite element simulations of varying shapes and sizes [150]. Finally, more recent research points to artificial intelligence and hybrid simulations to tackle the problem. In theory, problems which appear untenable due to having a surplus of key variables and parameters, are well suited for ar-

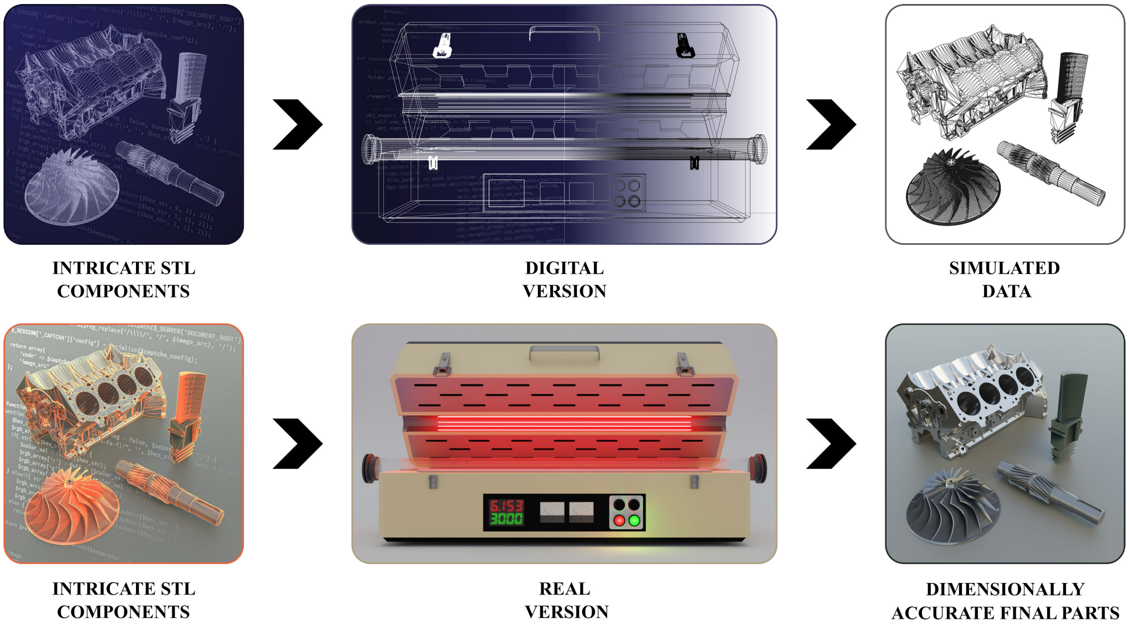

Figure 7.1: Graphical illustration of the process of utilizing artificially generated data to train a model and develop and accurate scaling method for STL (Stereolithography CAD) files to counter act the deformation that will occur during sintering.

tificial intelligence and machine learning assistance[52]. The industry requirements for sintering will most likely be solved through a hybrid of physics-based modeling combined with machine learning assistance.

Sintering models have lacked accuracy due to the high degree of difficulty in describing the physical phenomena that occur during the process. There are also a significant amount of factors that can affect this complex process. Some of the major parameters are particle size, material composition, original component geometry, sintering duration, maximum temperature, hold time, ramp rate, and oven conditions. These variables expand in complication due to material property dependence on temperature, exothermic reactions, microstructure changes, phase changes, residual stresses, and many more factors [46]. All of these factors are the reason that a comprehensive sintering model has eluded researchers for such a long period of time. Simplifications must be made in order to model the behavior. Some research has just looked at grain boundaries, surface area, and grain size as a method of prediction with good results[151]. Numerical simulations are effective, but difficult to have accurate material properties over the wide temperature range that occurs during sintering [152, 153]. Metal injection molding (MIM) can be easier to predict the final geometry, than additive manufactured components. This is because MIM parts are packed tight into molds and the binder jetted components are loosely held together by a binder. This means that sintering models will have to become more accurate to support the needs of the end user.

There are several new and innovative types of additive manufacturing methods, and this has led to a capability to 3D print more different materials. High temperature materials are much more complex to 3D print than thermoplastic materials. Many additive manufacturing techniques exploit the melting point to manipulate the material being printed. This means that high temperature materials have to be raised to higher temperatures during the manufacturing stage. 3D printing of ceramic and metallic components will always involve some form of sintering. The three most common 3D printing methods for metallic materials and ceramics are binder jet technology (BJT), selective laser sintering (SLS), and fused filament fabrication (FFF)[154]. All of these methods include a sintering phase.

BJT and FFF both involve a distinct printing phase and a distinct sintering phase during the manufacturing process. The BJT printing method involves dripping a binder onto a powder bed to hold the particles together during the “green" stage. The green stage refers to the stage during manufacturing prior to sintering, where the part is still fragile. The FFF method has the metallic powder bound together in a filament and then prints the component by rapid heating and extrusion [155, 156]. The printing stage of the FFF method is almost identical to a fused deposition method for a thermoplastic. After the printing stage, both FFF and BJT printed components will be processed and sintered. During the sintering phase the part or components will densify and shrink. The sintering modeling methods can be used to help predict this shrinkage. The SLS method uses a laser to rapidly heat up a powder and bind the powder together. This method does not require a sintering oven [157]. There are parts of this work that could assist in prediction of shrinkage during the rapid laser heating process in SLS method, but the developed method in this work is mostly focused on the oven sintering.

The turbomachinery industry can benefit greatly from additive manufacturing. The rapid production of intricate components, which are application specific, will allow for rapid prototyping and testing. The modeling of thermally grown oxides and other phenomena could provide more accurate information of the turbine health during operation [158, 159, 160].This increase in experimentation efficiency will increase problem solving capability and innovation for turbomachinery industry. Turbine blades are very intricately designed to help balance several competing performance parameters. Additive manufacturing could increase the capability of producing more intricate cooling patterns [161, 162]. The roughness could also be tailored to specific flow situations to help control the general cooling of the turbine blades[163]. In order to have these capabilities, the control over the additive manufacturing sintering process must first be better understood and gain better control on the process.

Because of the complexity of the physical phenomena that occur during sintering, modeling of shrinkage has been difficult. A more data driven approach that uses machine learning could help to fill in the gaps to create more comprehensive models. A graphical illustration of that process is given in Figure 7.1. This work will propose a framework for gathering data to help in modeling the sintering shrinkage trajectories. The main parameters that end users are concerned with are density and shrinkage, which are correlated. This work will aim to help predict these parameters based on data gathered before, after, and during sintering. The physics model used in this work is straight forward and simplistic to generate data for machine learning algorithms to create accurate models for shrinkage prediction. Machine learning and artificial intelligence approaches to additive manufacturing have been investigated in a variety of ways. Image processing techniques have been implemented to discover and classify defects during the manufacturing process [102]. Also, machine learning methods have been used to balance input parameters for optimal material properties [24]. Non destructive evaluation methods continue to advance and produce more data. This data is well suited to be more efficiently processed via machine learning techniques [7, 10].

7.2 Sintering Physics

It is very difficult to create a model which utilizes the temperature-dependent material properties to predict the amount of shrinkage that occurs. Many models assume material constants, however the constants change drastically with temperature. There are other temperature induced phenomena that make modeling difficult as well, like phase transformation, microstructural coarsening, and exothermic reactions. [46]. Simplifications are necessary with so many interacting parameters. Some of those parameters could be included as elasticity, plasticity, surface energy, particle size, particle shape, and many more. The models used in this work will be based on 3 measurable parameters including particle surface area, grain size, and density. It has been shown that these parameters can accurately model sintering trajectories on their own [164]. The end-users (industry) would prefer simpler formulas that are more focused on an accurate prediction on the amount of shrinkage that occurs.

Grain size, grain boundary, surface area, porosity, and density are all correlated parameters that can assist in sintering shrinkage modeling. A schematic of some of the aforementioned parameters are shown in Figure 7.2. Grain size is the average diameter of the grains. Grain boundary is indicated by the red area, which shows two particles in contact with each other, this is where necking occurs. The surface area is shown in purple, and that is the area where the particle is exposed to a pore and not in contact with another particle. All of these measurements can be taken from an SEM (Scanning Electron Microscope) image through various methods of image processing. ImageJ is

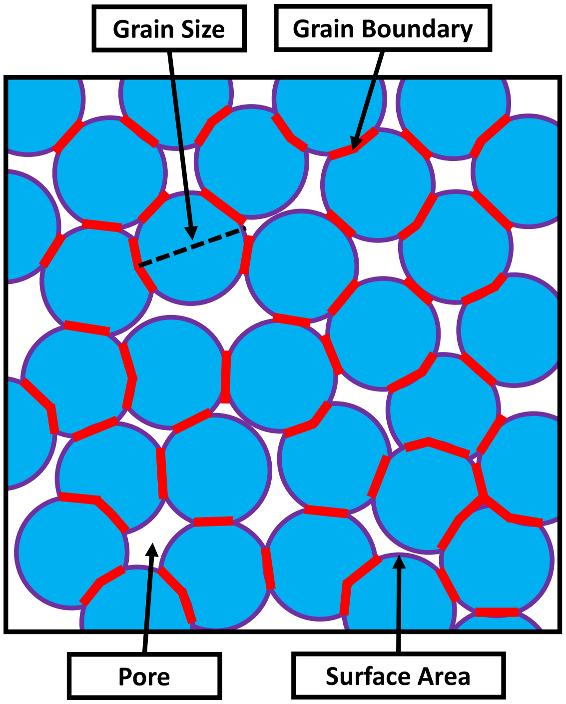

Figure 7.2: Sintering particle schematic: Grain size is the average diameter of the grains. Grain boundary is indicated by the red. Surface area is indicated by the purple. Porosity is the percentage of white area compared to total area.

one software that is capable of this[165].

Surface area could be measured by SEM images, but it can also be measured through gas absorption or fluid permeability. Surface area per unit mass (S_M) would be measured via gas absorption or fluid permeability and have the units m^2/g. The volumetric surface (S_V) area could be measured from an SEM image and would have the units m^2/m^3 [46]. The types of surface areas are interchangeable and related to the current sintered density ρ_s in Equation 7.1. Sintered density ρ_s is the theoretical maximum density ρ_T divided by the fractional density f. This is shown in Equation 7.2.

$$S_M = \frac{S_V}{\rho_S} \tag{7.1}$$

$$\rho_S = \frac{\rho_T}{f} \tag{7.2}$$

A way to model a given sintering trajectory is by plotting surface area against density. The constants a and b are dependent upon material and sintering conditions. Equation 7.3 shows this relationship. S_O represents initials surface area, f_S is current sintered fractional density, and S_M/S_O is often referred to as the normalized surface area. This relationship has seen experimental validation for various material configurations [166, 167, 46].

$$\frac{S_M}{S_O} = a - bf_S \tag{7.3}$$

Density is directly related to shrinkage in Equation 7.4. f_G represents the density of the "green" component. Green means the component has not yet been sintered. Y represents the shrinkage ($\triangle L/L_o$). This shrinkage term assumes uniform shrinkage in all directions.

$$f_S = \frac{f_G}{(1-Y)^3} \tag{7.4}$$

As sintering occurs, the surface area will slowly reduce. At the same time the grain size and grain boundaries will increase. A physical intuition of this can be obtained by looking at Figure 7.2. The relationship between grain size and sintering time is inverse cubic as shown in Equation 7.5. G is current grain size, G_O is green grain size, K is a material and temperature dependent parameter, and t is sintering hold time. If we solve for current grain size in Equation 7.5, we can get Equation 7.6. Equation 7.6 is given in a forward time step format [46].

$$G^3 = G_O{}^3 + Kt \tag{7.5}$$

$$G_2 = [G_1^3 + \triangle t_{1-2}K)]^{1/3} \tag{7.6}$$

A quick conversion between fractional porosity ε and fractional density f is given in Equation 7.7. Porosity is the ratio of total volume of pores to the total volume of the given component.

$$\varepsilon = 1 - f \tag{7.7}$$

A conversion between grain size G and fractional porosity ε is given in Equation 7.8. Here, G_0 is initial grain size, and θ is a geometric constant that is near 0.6 [164].

$$G = \theta \frac{G_0}{\sqrt{\varepsilon}} \tag{7.8}$$

It is possible to use more complex equations and relationships to describe sintering, however the end goal is to create a simplistic model that can be implemented by the additive manufacturing industry to accurately predict shrinkage and maximize density. Surface area, grain size, and grain boundaries can all be used to help predict the sintering duration versus densification relationships. Densification is directly related to shrinkage, so scaling prior to sintering could be done more accurately.

7.3 Sintering Data Measurement and Data Generation

There are some generated plots of the values obtained experimentally in Figure 7.3. The values are from stainless steel 17-4 PH, printed from a Markforged Metal-X printer. The parts were sintered with the specifications selected by the software. This means for this work the oven conditions and material were held constant. The values for the plots are $K = 5.5 \mu m^3/min$, $G_O = 2.5\mu$m, $G = 20\mu$m, $a = 3.3$, and $b = -3.6$. These plots help to illustrate the relationship between time, density, grain size, and surface area. The plots were generated using Equation 7.3, Equation 7.5, Equation 7.7, and Equation 7.8. The plots show that during sintering grain size increases. As the density increases, grain size will increase at a faster rate, and as sintering time increases, grain size will increase at a slower rate. Density will increase quickly during the beginning of the sintering, but it slows down as the sintering time increases. Normalized surface area has a linear relationship with fractional density. Surface area decreases as the density increases, and therefore will decrease as the sintering time increases. The relationship between grain size versus time is inversely cubic, and the relationship between grain size and density is cubic. Moreover, the relationship between density versus time is also inversely cubic in these plots.

All parameters can be measured, ultimately the end user will want to optimize sintering time and conditions to ensure high uniform density. Surface area, density, and grain size can all be measured experimentally. These measurements will have some errors which will be explored in this work. The error will be simulated via adding Gaussian noise to the measured variables. The parameters that we want to calculate from the simulated measurements are a, b, and K. These parameters help to describe the relationships between surface area, grain size, and density. The measurement of surface area and grain size can be done from SEM image pixels in a variety of ways. The most simplistic is to draw a line and and use the scale provided by that line to determine how long the line is. Then you count how many particles that the line touches. The grain size is equivalent to

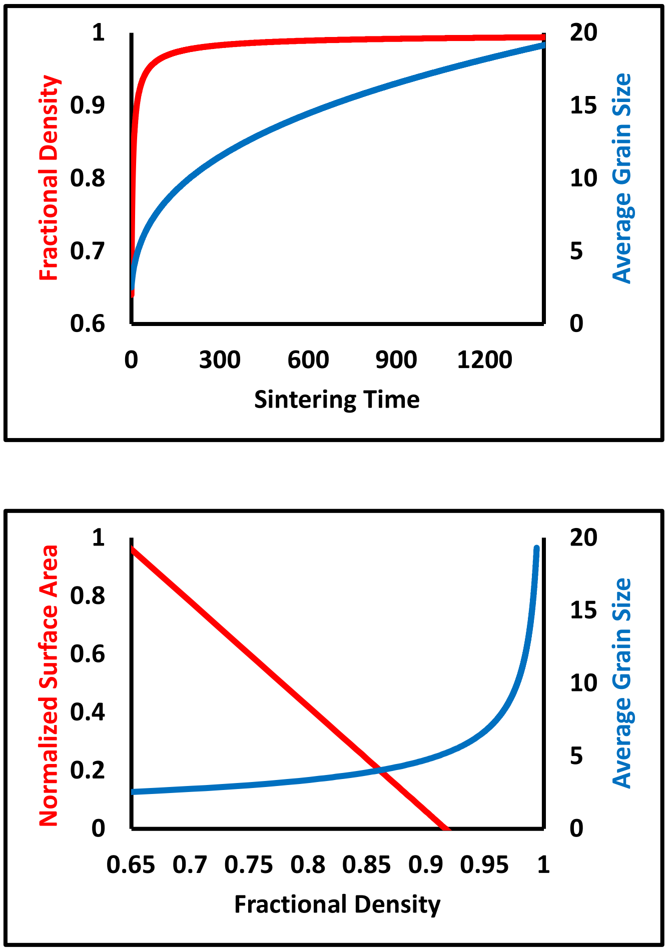

Figure 7.3: Artificially generated sintered data: (Top Graph) fractional density (normalized) and average grain size (μm) are plotted against sintering duration (minutes). (Bottom Graph) surface area (normalized) and average grain size (μm) are plotted against fractional density (normalized).

the number of particles divided by the length of the line. This is shown in Equation 7.9 as follows:

$$Grain\ Size = \frac{Number\ of\ Grains\ in\ Contact\ With\ Line}{Total\ Length\ of\ the\ Line} \tag{7.9}$$

The process is also illustrated in the SEM pictures in Figure 7.4. The top images are green Markforged Metal-X 17-4 PH stainless steel. The bottom images are the same components after sintering according to the Markforged proprietary algorithm. For the line in the top right, the grain size calculation is about 2.5 μm and for the bottom left the line indicated provides a grain size of about 20 μm.

The surface area measurement is more complex. The perimeter of the particles must be measured for this. This can be done through pixel threshold adjustment and pixel clustering. This can be done fairly easily using ImageJ software [165]. The surface area of the post-sintered components is almost zero. In the bottom left image of Figure 7.4, we can see only a few voids, which will provide a very low surface area. In the bottom right image of Figure 7.4, there are a few particles which remain unsintered. This image is taken at the interface between two layers of the 3D print. The surface area will be higher in this region and the grain size will be smaller. This means there is a lower density in that region as well.

The measurements from the Markforged 17-4 PH stainless steel gave a pre-sintered grain size of 2.5 μm and after sintered grain size of 20 μm. This is for the red lines shown on Figure 7.4. ImageJ could do this for every pixel line in the image. The images are 1280 × 960 pixels. There is the black bar with data that would need to be cropped out making it 1280 × 860 pixels. This is 1280 lines for measurement in the vertical direction and 860 lines in the horizontal that could be used to calculate the grain size. This was done through ImageJ for the image on the top right which led to a grain size of 2.5 ± 0.6 μm. 0.6 μm is the standard deviation. It was more difficult to have ImageJ do this automatically for the post-sintering because the brightness is different in different regions of the image. This was completed by hand with 20 lines in both the vertical and horizontal directions. The measurements for horizontal were 23.3 ± 1.2 μm and 20.1 ± 1.5 μm in the vertical direction. If we use the number 20 μm for post-sintered and 2.5 μm for pre-sintered, and the total sintering time was 24 hours (1440 minutes), then K would be equal to 5.5 $\frac{\mu^3}{min}$. The grain size measurements are shown in Table7.1. The global coordinates for the horizontal would be the X-direction and the vertical would be the Z-Direction. All the data used for the machine learning approach suggested in this work is derived from this experimental data. The data is created by adding Gaussian noise to the measured data that was determined through the process described in this paragraph.

Table 7.1: EXPERIMENTAL GRAIN SIZE MEASUREMENTS.

Time	Before Sintering	After Sintering
Grain Size Horizontal	$2.5 \pm 0.6\ \mu$m	$23.3 \pm 1.2\ \mu$m
Grain Size Vertical	$2.4 \pm 0.5\ \mu$m	$20.1 \pm 1.5\ \mu$m

The uncertainty in the measurements for grain size is in the form of microns. This was demonstrated in the measurements recorded in Table7.1. In order to generate artificial data for this paper, Equation 7.5 and Equation 7.6 will be used. The Gaussian noise will be applied to the grain size measurements to simulate reality. The parameter that will be calculated is K, and the degree of accuracy with which this parameter can be calculated will be recorded. For the surface area, the problem is slightly different. There is still uncertainty in the measurement of both density and surface area, but they are different. To combat this, the Gaussian noise will be applied to the normalized surface area and the fractional density. This means the Gaussian noise is dimensionless as both properties are normalized. The parameters to be determined will be a and b, and again the degree of accuracy of these parameters will be reported. The surface area equation is listed in Equation 7.3.

7.4 Machine Learning Prediction Methods

In this work I developed a machine learning method that uses regression on supplied data to determine the relationship between sintering time, grain size, surface area, and density. The data was mostly generated artificially, but it was based on the measurements taken from the sample seen in Figure 7.4. The data was generated by adding Gaussian noise to the data that was measured

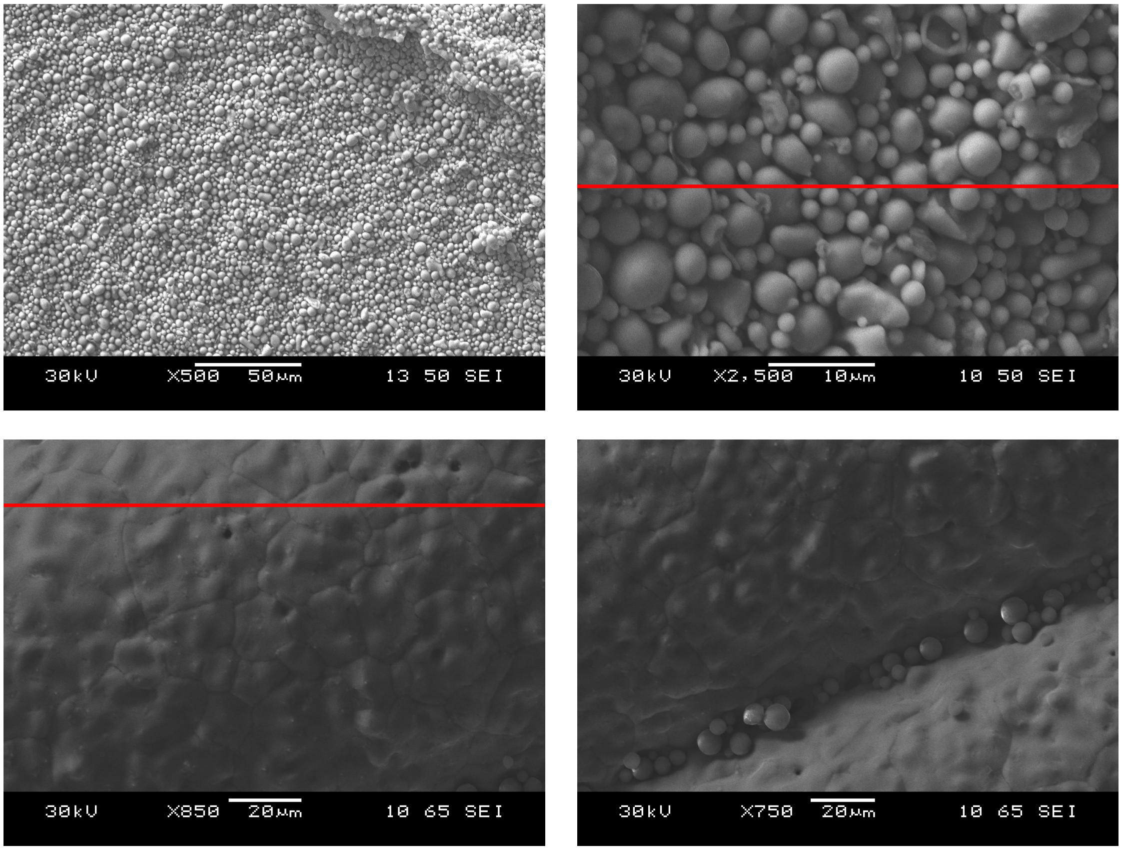

Figure 7.4: SEM images of the markforged metal X printed components from 17-4 PH stainless steel: (Top 2 Images) green components, after extrusion and prior to sintering. (Bottom 2 images) after sintering at the markforged specifications.

experimentally. The grain size, sintering time, surface area, and density relationships were then determined using linear regression and polynomial regression. The input for this model is the material properties (grain size, surface area, and density). This was produced from adding Gaussian noise to the experimental data to supplement the data set. The output for this model is the sintering trajectory parameters (a, b, or K). If an accurate sintering trajectory is to be defined for a given material and oven condition, the uncertainty of measurements must be quantified. This can be done by preemptively inserting uncertainty into the measurements and determining what effect this has on the final outcome of the parameters of interest. All code for this work is available in a Github repository [87]. The code is broken into three parts: one is for generating plots with various parameters, one is for the prediction of surface area parameters, and the last one is for the prediction of grain size parameters. The language of the code is python and it was written in Anaconda GUI.

If sintering trajectories can be produced with quantifiable uncertainty, then they can be implemented and optimize sintering times for material properties, like density. The prediction of shrinkage is essential and is directly related to density through Equation 7.4. The graphs in Figure 7.5 show the uncertainty in the predictions for the a and b parameters associated with surface area. The standard deviation is indicated by StD in the legends of the graph. The error percentage is given by the Y-axis and the number of measurements is given by the X- axis. The standard deviation was applied equally to the fractional density and normalized surface area. A total of 10,000 simulations were run for all 4 of the standard deviations in the legend. The machine learning method applied to the generated data was linear regression. It is clear that a reduction in the uncertainty within the measurements will decrease the error. Another solution would be to simply take more measurements. Taking measurements requires the user to stop the sintering process, take measurements, and then restart the sintering process. This will most likely affect the sintering process, so fewer measuring points should be desired. When the standard deviation is significantly low, very few measurements are required. It is also clear the number of measurements does not produce less error in the a and b parameters at around 7 or 8. Parameters a and b are described in Equation 7.3, they relate density to surface area. If you count the final measurement, this would mean stopping the process about 6 or 7 times. The beginning is not counted because all measurements are normalized with respect to the first measurement for surface area.

The uncertainty in measuring the fractional density should only occur in the measuring of the sintered density according to Equation 7.2. The theoretical density should be well known (unless it is a new material). Therefore the uncertainty will occur during the measuring of the current sintered density. The surface area measurement uncertainty will depend on both the sintered density measurement as well as the volumetric surface area according to Equation 7.1. The error equation is shown in Equation 7.10 as follows:

$$Percent\ Error = \left|\frac{True\ Value - Measured\ Value}{True\ Value}\right| \cdot 100\% \tag{7.10}$$

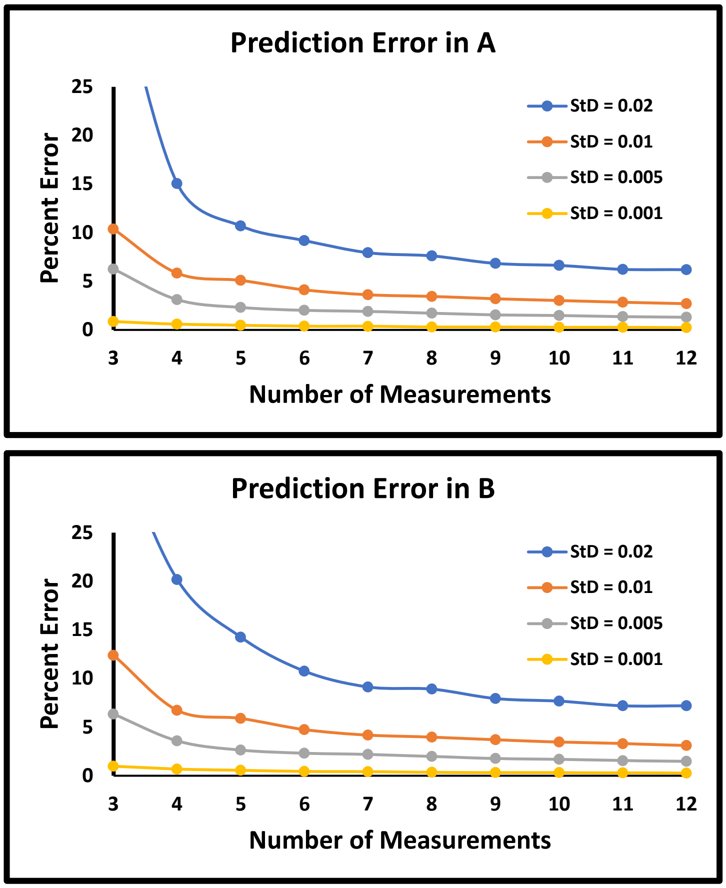

Figure 7.5: Prediction error for parameters in equation 7.3 from artificially generated data by adding Gaussian noise to experimentally gathered data. The data is then modeled through linear regression to determine a and b: (Top Graph) Prediction error in material parameter a (Bottom Graph) Prediction error in material parameter b

The error quantification calculations were also performed for the grain size. The grain size equations used were Equation 7.5 and Equation 7.6. The standard deviation was varied for the input grain size for $K = 5$. For these results, 10,000 simulations were run at each standard deviation increment. The standard deviation increment was 0.1 μm from 0.1 μm to 2.9 μm. The unit for grain size was μm. K was determined through polynomial regression. The Gaussian noise was added to both the current and original grain size. Total sintering time was set to 1440 minutes or 24 hours. The relationship from the sintering model between the standard deviation in grain size measurement and the accuracy of K prediction is shown in Figure 7.6. The standard deviation range is compatible with most FFF and BJT printing materials and sintering configurations. The standard deviation could be higher values if the user starts with particles of varying size, but this is not very common for additive manufacturing where everything needs to be highly controlled.

The number of measurements for grain size was varied from 1 to 4. This is shown in the legend of Figure 7.6. 1 measurement indicates measuring before and after sintering. The additional measurements were taken 1 hour prior to completion of sintering. This means that for 4 measurements, the grain size was recorded at 3, 2, and 1 hour(s) before sintering completion, and then again when sintering was completed. It was determined that measuring the grain size in the latter part of the sintering treatment produced higher accuracy in the K parameter. This is caused by the cubic nature of the function. The increase in measurement does increase the accuracy in which K can be predicted. Decreasing the standard deviation in the grain size seems to have a greater effect. The accuracy of an SEM image can provide the grain size with a fairly low standard deviation for the system examined in this work. This was the FFF Markforged 17-4 PH stainless steel. More SEM images would provide a better picture of the grain size distribution. In addition, this method could be expanded into 3 dimensions by changing the orientation of where the SEM is taken. This will be shown in the next section.

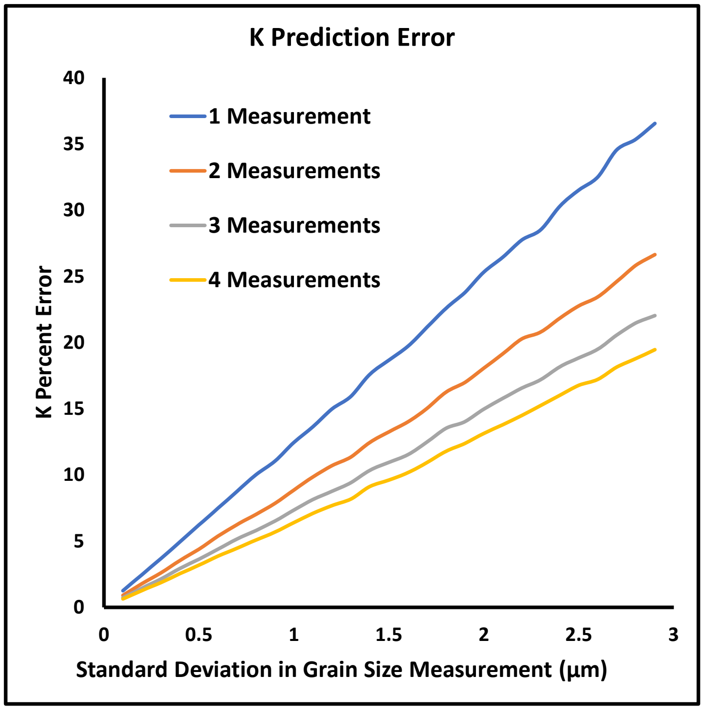

Figure 7.6: Prediction error in the parameter K in equation 7.5. The standard deviation in measurement for grain size is shown on the X-Axis and the average error in K prediction is shown on the Y-axis. The machine learning method is linear regression and the data was generated by adding Gaussian noise to experimental data.

7.5 Expansion to Three Dimensions

The sintering process for additive manufactured components and metal injected molding components is very similar. One main difference is that the additive manufactured components will have anisotropic properties due to the layer-by-layer print style. This is especially true for the highlighted methods in this work, which are FFF and BJT. In between the layers of 3D print, the properties will not be the same as in the middle of the layer. This will require the equations that describe the sintering process to be expanded into three dimensions. There is also a need to format these equations to operate on the STL (stereolithography CAD) data that is used for 3D printing software. Expansion of Equation 7.5 is shown in 3D in Equation 7.11, Equation 7.12, and Equation 7.13. This leads to 3 separate Ks (one for each direction) that can be used to predict and then control the shrinkage during sintering.

The same expansion process can be applied on Equation 7.3. From this system of equations, the density could be solved for in each Cartesian direction using Equation 7.8 or Equation 7.3. Ultimately 3D printing pre-sintering scaling algorithms will need to conform and adapt to the discrepancies in shrinkage in different directions or optimize 3D printing and sintering parameters to minimize these differences or a combination of the two. We propose the solution will be a combination of the two.

$$G_x^3 = {G_{xO}}^3 + K_x t \tag{7.11}$$

$$G_y^3 = {G_{yO}}^3 + K_y t \tag{7.12}$$

$$G_z^3 = {G_{zO}}^3 + K_z t \tag{7.13}$$

File formats for 3D components that are about to be sliced, are typically STL, OBJ, or AMF. There are others but the most common are STL and OBJ. STLs are stored in the form of a triangulated mesh. The mesh consists of 3 points in Cartesian coordinates. These points form a triangle and the normal of that triangle indicates the outer or inner surface of the CAD. Scaling the STL files is done by directly multiplying a scaling factor to the points in the vertices of the triangulated mesh. If a component was going to shrink by uniformly by 20% in all directions during sintering, then the software should just scale up the component by 20% prior to sintering. The issue is that the scale factors are not uniform with additive manufacturing. By measuring grain sizes in each direction the scale factors could also be retroactively determined and applied preemptively in future prints. The difference in grain size growth during sintering was clearly shown in Table7.1.

The method of measurement for the grain size growth in the different Cartesian coordinate's is illustrated in Figure 7.7. If the user takes at least 3 different SEM images of the component from the 3 different planes, the grain size growth can be determined. It could even be completed with just 2, but 3 is more thorough. Each image provides the ability to measure grain size using the line method shown in Equation 4.1. The line can go pixel by pixel as shown in Figure 7.4. 3 Images provide the ability to take the measurements for each direction twice, and for each pixel in that dimension. If all the images are 500×500, that would yield 1000 lines to measure grain size per direction.

Using this 3D format to predict shrinkage could allow the user to implement the algorithm on a variety of geometries. The effect of different geometries could be measured and computed via Equation 7.11, Equation 7.12, and Equation 7.13. The parameter K can account for discrepancies in shrinkage that come with manufacturing different geometries. This machine learning approach is a framework that can be used if given a substantial data set.

7.6 Conclusion

A framework was produced in this work to utilize the capabilities of machine learning on the data generated from sintering data experiments. This data can be extrapolated and fed into machine learning models to help to predict the trajectory at which a component will densify during sintering. If accurate pathways are known for sintering, accurate scaling and modifications can be applied to the pre-sintered component for optimal output results. The models in this work generate thousands of artificial data points and then feed these points into machine learning algorithms. The models

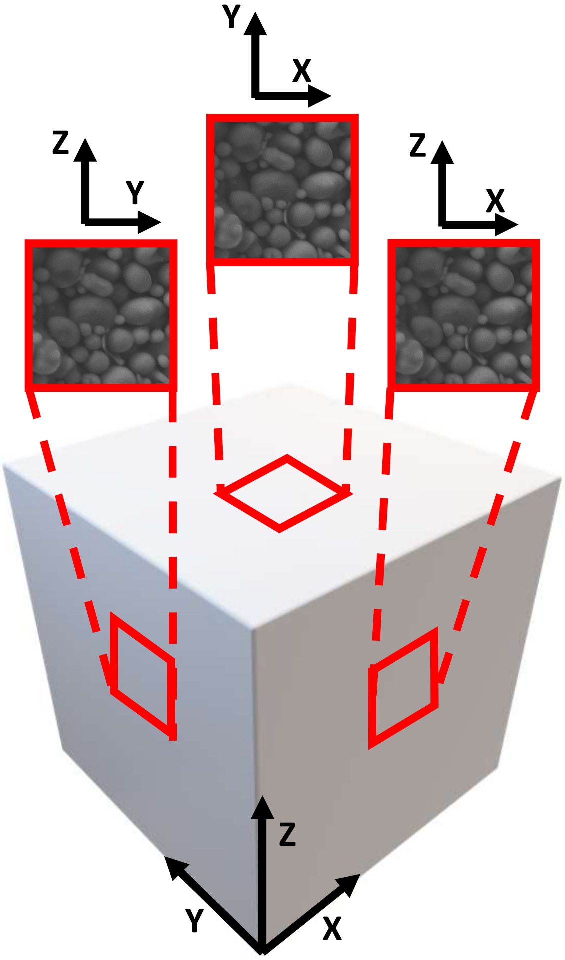

Figure 7.7: Visual schemative of measurement of grain size in a specific cartesian direction. Three SEM images would provide the opportunity to measure grain size twice in the X, Y and Z direction.

were also supported and verified by experimental data. The method created in this work is a good foundation to apply machine learning to this kind of data. In the future more data could be included to further refine the method and account for a change in material or oven condition. More machine learning methods, such as neural networks might also be necessary if more and more different types of data are to be utilized.

The effect that accuracy of measurement has on the prediction of key sintering parameters was shown in this work. The relationship between the number of measurements during sintering with the final prediction accuracy was also shown. These parameters need to be balanced in order to determine the optimal number of measurements required to ensure a given level of confidence in the sintering parameter of interest. Stopping the oven and taking measurements is not convenient and may affect the sintering process. This work has shown a way to determine the minimum amount of stops and measurements required for the end user to make an accurate prediction of deformation and other properties during sintering.

Additive manufacturing of metallic and ceramic components typically needs to undergo sintering prior to manufacturing completion. This requires an accurate knowledge of the sintering process. The components need to be scaled correctly in order to ensure geometric accuracy in the final component. The method presented in this work has been shown that it can expand to 3-dimensions to help predict the shrinkage and deformation more accurately. Additive manufactured components do not shrink uniformly and need to be scaled up prior to sintering accordingly. The models presented in this work can predict the amount of shrinkage in each direction and scale files accordingly. This will be essential moving forward for the additive manufacturing of high temperature metallic and ceramic components.

REFERENCES

[1] P Gardner et al. "Machine learning at the interface of structural health monitoring and non-destructive evaluation". In: Philosophical Transactions of the Royal Society A 378.2182 (2020), p. 20190581.

[2] Mohammad I Albakri et al. "Impedance-based non-destructive evaluation of additively manufactured parts". In: Rapid Prototyping Journal (2017).

[3] Tuan D Ngo et al. "Additive manufacturing (3D printing): A review of materials, methods, applications and challenges". In: Composites Part B: Engineering 143 (2018), pp. 172–196.

[4] Yong He et al. "Developments of 3D printing microfluidics and applications in chemistry and biology: a review". In: Electroanalysis 28.8 (2016), pp. 1658–1678.

[5] Md Hazrat Ali, Shaheidula Batai, and Dastan Sarbassov. "3D printing: A critical review of current development and future prospects". In: Rapid Prototyping Journal (2019).

[6] Hessein Ali et al. "Tailorable stiffness lightweight soft robotic materials with architectured exoskeleton". In: AIAA Scitech 2020 Forum. 2020, p. 1551.

[7] Peter Warren et al. "Investigation of an Advanced Acoustic Based Nondestructive Evaluation Method". In: Turbo Expo: Power for Land, Sea, and Air. Vol. 58677. American Society of Mechanical Engineers. 2019, V006T05A005.

[8] Peter Warren. "Nondestructive Testing Methods Aided Via Numerical Computation Models for Various Critical Aerospace Power Generation Systems". MA thesis. University of Central Florida, 2018.

[9] Jan Drewes Achenbach. "Quantitative nondestructive evaluation". In: International Journal of Solids and Structures 37.1-2 (2000), pp. 13–27.

[10] Joel B Harley and Daniel Sparkman. “Machine learning and NDE: Past, present, and future”. In: AIP Conference Proceedings. Vol. 2102. 1. AIP Publishing LLC. 2019, p. 090001.

[11] Peipei Zhu et al. “A novel machine learning model for eddy current testing with uncertainty”. In: NDT & E International 101 (2019), pp. 104–112.

[12] Peter Warren. “Particle Dataset”. `https://www.kaggle.com/datasets/peterwarren/particle-dataset`. 2023.

[13] Peter Warren. “Artificial Grains and Real Grains”. `https://www.kaggle.com/datasets/peterwarren/voronoi-artificial-grains-gen`. 2023.

[14] Peter Warren. “ExONE Stainless Steel 316L Grains 500X”. `https://www.kaggle.com/datasets/peterwarren/exone-stainless-steel-316l-grains-500x`. 2023.

[15] Mostafa Yakout, MA Elbestawi, and Stephen C Veldhuis. “A review of metal additive manufacturing technologies”. In: Solid State Phenomena 278 (2018), pp. 1–14.

[16] ASTM Committee F42 on Additive Manufacturing Technologies and ASTM Committee F42 on Additive Manufacturing Technologies. Subcommittee F42. 91 on Terminology. Standard terminology for additive manufacturing technologies. Astm International, 2012.

[17] Amir Mostafaei et al. “Binder jet 3D printing–Process parameters, materials, properties, and challenges”. In: Progress in Materials Science (2020), p. 100707.

[18] Mohsen Ziaee, Eric M Tridas, and Nathan B Crane. “Binder-jet printing of fine stainless steel powder with varied final density”. In: Jom 69.3 (2017), pp. 592–596.

[19] Craig Buchanan and Leroy Gardner. “Metal 3D printing in construction: A review of methods, research, applications, opportunities and challenges”. In: Engineering Structures 180 (2019), pp. 332–348.

[20] Zengguang Liu et al. “A critical review of fused deposition modeling 3D printing technology in manufacturing polylactic acid parts”. In: The International Journal of Advanced Manufacturing Technology 102.9 (2019), pp. 2877–2889.

[21] Samuel Clinton Daminabo et al. “Fused deposition modeling-based additive manufacturing (3D printing): techniques for polymer material systems”. In: Materials today chemistry 16 (2020), p. 100248.

[22] K Arunprasath et al. “Development in Additive Manufacturing Techniques”. In: Innovations in Additive Manufacturing. Springer, 2022, pp. 33–53.

[23] Chengcheng Wang et al. “Machine learning in additive manufacturing: State-of-the-art and perspectives”. In: Additive Manufacturing 36 (2020), p. 101538.

[24] Lingbin Meng et al. “Machine learning in additive manufacturing: a review”. In: Jom 72.6 (2020), pp. 2363–2377.

[25] Zeqing Jin et al. “Machine learning for advanced additive manufacturing”. In: Matter 3.5 (2020), pp. 1541–1556.

[26] Wayne E King et al. “Laser powder bed fusion additive manufacturing of metals; physics, computational, and materials challenges”. In: Applied Physics Reviews 2.4 (2015), p. 041304.

[27] SL Sing and WY Yeong. “Laser powder bed fusion for metal additive manufacturing: perspectives on recent developments”. In: Virtual and Physical Prototyping 15.3 (2020), pp. 359–370.

[28] Valmik Bhavar et al. “A review on powder bed fusion technology of metal additive manufacturing”. In: Additive manufacturing handbook (2017), pp. 251–253.

[29] HR Kotadia et al. “A review of Laser Powder Bed Fusion Additive Manufacturing of aluminium alloys: Microstructure and properties”. In: Additive Manufacturing 46 (2021), p. 102155.

[30] Wenchao Du et al. “Binder jetting additive manufacturing of ceramics: A literature review”. In: ASME International Mechanical Engineering Congress and Exposition. Vol. 58493. American Society of Mechanical Engineers. 2017, V014T07A006.

[31] Saereh Mirzababaei and Somayeh Pasebani. “A review on binder jet additive manufacturing of 316L stainless steel”. In: Journal of Manufacturing and Materials Processing 3.3 (2019), p. 82.

[32] Ming Li et al. “Metal binder jetting additive manufacturing: a literature review”. In: Journal of Manufacturing Science and Engineering 142.9 (2020).

[33] James Frederic Bredt. “Binder stability and powder/binder interaction in three-dimensional printing.” In: (1997).

[34] Peter Ross Baker. “Three dimensional printing with fine metal powders”. PhD thesis. Massachusetts Institute of Technology, 1997.

[35] Tailin Fan. “Droplet-powder impact interaction in three dimensional printing”. PhD thesis. Massachusetts Institute of Technology, 1996.

[36] Marcos Esterman. “Characterization of the powder/binder interaction in the three dimensional printing process”. PhD thesis. Massachusetts Institute of Technology, 1990.

[37] Mika Salmi. “Additive manufacturing processes in medical applications”. In: Materials 14.1 (2021), p. 191.

[38] Ahmed Elkaseer et al. “Material jetting for advanced applications: A state-of-the-art review, gaps and future directions”. In: Additive Manufacturing (2022), p. 103270.

[39] RM German. “History of sintering: empirical phase”. In: Powder Metallurgy 56.2 (2013), pp. 117–123.

[40] Randall German. Sintering: from empirical observations to scientific principles. Butterworth-Heinemann, 2014.

[41] Ernst Pernicka et al. Early Bronze Age metallurgy in the north-east Aegean. Springer, 2003.

[42] Lili Fang. Chinese ceramics. Cambridge University Press, 2011.

[43] John Collis. The European iron age. Routledge, 2003.

[44] Hermann Genz and Dirk Paul Mielke. Insights into Hittite history and archaeology. Peeters Leuven, 2011.

[45] Leslie Anne Warden. Ceramic Perspectives on Ancient Egyptian Society. Cambridge University Press, 2021.

[46] Randall M German. Sintering theory and practice. 1996.

[47] Ernest R Alexander. “Density measures: A review and analysis”. In: Journal of architectural and planning research (1993), pp. 181–202.

[48] David Brandon and Wayne D Kaplan. Microstructural characterization of materials. John Wiley & Sons, 2013.

[49] Norman Bekkedahl. “Volume dilatometry”. In: J Res Natl Bur Stand 43.2 (1949), pp. 145–56.

[50] Melvin Avrami. “Kinetics of phase change. I General theory”. In: The Journal of chemical physics 7.12 (1939), pp. 1103–1112.

[51] Melvin Avrami. “Kinetics of phase change. II transformation-time relations for random distribution of nuclei”. In: The Journal of chemical physics 8.2 (1940), pp. 212–224.

[52] Eugene A Olevsky, Veena Tikare, and Terry Garino. “Multi-scale study of sintering: a review”. In: Journal of the American Ceramic Society 89.6 (2006), pp. 1914–1922.

[53] Stephen C Parker and Charles T Campbell. “Kinetic model for sintering of supported metal particles with improved size-dependent energetics and applications to Au on TiO 2 (110)”. In: Physical Review B 75.3 (2007), p. 035430.

[54] Jingzhe Pan. “Modelling sintering at different length scales”. In: International Materials Reviews 48.2 (2003), pp. 69–85.

[55] Warren S McCulloch and Walter Pitts. “A logical calculus of the ideas immanent in nervous activity”. In: The bulletin of mathematical biophysics 5 (1943), pp. 115–133.

[56] Frank Rosenblatt. “The perceptron: a probabilistic model for information storage and organization in the brain.” In: Psychological review 65.6 (1958), p. 386.

[57] Yann LeCun et al. “Handwritten digit recognition with a back-propagation network”. In: Advances in neural information processing systems 2 (1989).

[58] Keiron O’Shea and Ryan Nash. “An introduction to convolutional neural networks”. In: arXiv preprint arXiv:1511.08458 (2015).

[59] Phil Kim and Phil Kim. “Convolutional neural network”. In: MATLAB deep learning: with machine learning, neural networks and artificial intelligence (2017), pp. 121–147.

[60] Olaf Ronneberger, Philipp Fischer, and Thomas Brox. “U-net: Convolutional networks for biomedical image segmentation”. In: International Conference on Medical image computing and computer-assisted intervention. Springer. 2015, pp. 234–241.

[61] Ian J Goodfellow. “On distinguishability criteria for estimating generative models”. In: arXiv preprint arXiv:1412.6515 (2014).

[62] Ian Goodfellow et al. “Generative adversarial networks”. In: Communications of the ACM 63.11 (2020), pp. 139–144.

[63] Ian J Goodfellow, Jonathon Shlens, and Christian Szegedy. “Explaining and harnessing adversarial examples”. In: arXiv preprint arXiv:1412.6572 (2014).

[64] Sandip Haldar et al. “Synchrotron XRD Measurements of Thermal Barrier Coating Configurations With Rare Earth Elements for Phosphor Thermometry”. In: Turbo Expo: Power for Land, Sea, and Air. Vol. 58677. American Society of Mechanical Engineers. 2019, V006T24A014.

[65] Kun Qian. “Automated Detection of Steel Defects via Machine Learning based on Real-Time Semantic Segmentation”. In: Proceedings of the 3rd International Conference on Video and Image Processing. 2019, pp. 42–46.

[66] Ihor Konovalenko et al. “Steel Surface Defect Classification Using Deep Residual Neural Network”. In: Metals 10.6 (2020), p. 846.

[67] Vira Fitriza Fadli and Iwa Ovyawan Herlistiono. “Steel Surface Defect Detection using Deep Learning”. In: ().

[68] John Brandon Graham-Knight. “Efficient 2D image segmentation”. PhD thesis. University of British Columbia, 2020.

[69] Junyoung Park et al. “Computed tomography super-resolution using deep convolutional neural network”. In: Physics in Medicine & Biology 63.14 (2018), p. 145011.

[70] Bram Van Ginneken et al. "Off-the-shelf convolutional neural network features for pulmonary nodule detection in computed tomography scans". In: 2015 IEEE 12th International symposium on biomedical imaging (ISBI). IEEE. 2015, pp. 286–289.

[71] Severstal. Steel Defect Dataset. Kaggle. URL https://www.kaggle.com/c/severstal-steel-defect-detection. Oct. 2019.

[72] Kaiming He et al. "Deep residual learning for image recognition". In: Proceedings of the IEEE conference on computer vision and pattern recognition. 2016, pp. 770–778.

[73] NEU. Steel Defect Dataset. (accessed November 30, 2020) `http://faculty.neu.edu.cn/yunhyan/NEU_surface_defect_database.html`. 2018.

[74] UCI. Steel Defect Dataset. (accessed November 30, 2020) `https://archive.ics.uci.edu/ml/index.php`. 2020.

[75] Fuyao Yan, Wei Xiong, and Eric J Faierson. "Grain structure control of additively manufactured metallic materials". In: Materials 10.11 (2017), p. 1260.

[76] Jianguo Lin, Daniel Balint, and Maciej Pietrzyk. Microstructure evolution in metal forming processes. Elsevier, 2012.

[77] Choong Do Lee. "Effect of grain size on the tensile properties of magnesium alloy". In: Materials Science and Engineering: A 459.1-2 (2007), pp. 355–360.

[78] Philipp Schempp et al. "Influence of grain size on mechanical properties of aluminium GTA weld metal". In: Welding in the World 57.3 (2013), pp. 293–304.

[79] Ning Wang et al. "Effect of grain size on mechanical properties of nanocrystalline materials". In: Acta Metallurgica et Materialia 43.2 (1995), pp. 519–528.

[80] SI Heo et al. "Influence of particle size and shape on electrical and mechanical properties of graphite reinforced conductive polymer composites for the bipolar plate of PEM fuel cells". In: Advanced composite materials 15.1 (2006), pp. 115–126.

[81] Sheikh M Uddin et al. "Effect of size and shape of metal particles to improve hardness and electrical properties of carbon nanotube reinforced copper and copper alloy composites". In: Composites Science and Technology 70.16 (2010), pp. 2253–2257.

[82] Nandhini Raju et al. "Sintering Behaviour of 3d Printed 17-4PH Stainless Steel". In: Turbo Expo: Power for Land, Sea, and Air. Vol. 86052. American Society of Mechanical Engineers. 2022, V007T17A028.

[83] Peter Warren et al. "Shrinkage Prediction Using Machine Learning for Additively Manufactured Ceramic and Metallic Components for Gas Turbine Applications". In: Turbo Expo: Power for Land, Sea, and Air. Vol. 85987. American Society of Mechanical Engineers. 2022, V002T05A023.

[84] Yun Bai, Grady Wagner, and Christopher B Williams. "Effect of particle size distribution on powder packing and sintering in binder jetting additive manufacturing of metals". In: Journal of Manufacturing Science and Engineering 139.8 (2017).

[85] Nandhini Raju et al. "Material Properties of 17-4PH Stainless Steel Fabricated by Atomic Diffusion Additive Manufacturing (ADAM)". In: 2021 International Solid Freeform Fabrication Symposium. University of Texas at Austin. 2021.

[86] G. Bradski. "The OpenCV Library". In: Dr. Dobb's Journal of Software Tools (2000).

[87] Peter Warren. "SinteringTrajectory Github Repository". `https://github.com/Peterwarren623/GrainBoundaryDetection`. 2022.

[88] John Canny. “A computational approach to edge detection”. In: IEEE Transactions on pattern analysis and machine intelligence 6 (1986), pp. 679–698.

[89] Saining Xie and Zhuowen Tu. “Holistically-nested edge detection”. In: Proceedings of the IEEE international conference on computer vision. 2015, pp. 1395–1403.

[90] Emil Heyn. Physical Metallography. Wiley, 1925.

[91] Georges Voronoi. “Nouvelles applications des paramètres continus à la théorie des formes quadratiques. Deuxième mémoire. Recherches sur les parallélloèdres primitifs.” In: Journal für die reine und angewandte Mathematik (Crelles Journal) 1908.134 (1908), pp. 198–287.

[92] Jie Yin et al. “Correlation between forming quality and spatter dynamics in laser powder bed fusion”. In: Additive Manufacturing 31 (2020), p. 100958.

[93] M Hossein Sehhat and Ali Mahdianikhotbesara. “Powder spreading in laser-powder bed fusion process”. In: Granular Matter 23.4 (2021), p. 89.

[94] Alistair Jones et al. “Effect of surface geometry on laser powder bed fusion defects”. In: Journal of Materials Processing Technology 296 (2021), p. 117179.

[95] Alexander J Wildgoose et al. “Impacts of the Additive Manufacturing Process on the Roughness of Engine Scale Vanes and Cooling Channels”. In: Turbo Expo: Power for Land, Sea, and Air. Vol. 86045. American Society of Mechanical Engineers. 2022, V06BT13A025.

[96] Ramesh Subramanian. “Additive Manufactured Metallic 3D Ox-Ox CMC Integrated Structures for 65% Combined Cycle Efficient Gas Turbine Components”. In: Siemens Energy, Inc., Orlando, FL (United States). 2020.

[97] Kenneth DM Harris, Maryjane Tremayne, and Benson M Kariuki. “Contemporary advances in the use of powder X-ray diffraction for structure determination”. In: Angewandte Chemie International Edition 40.9 (2001), pp. 1626–1651.

[98] Ronan McCann et al. “In-situ sensing, process monitoring and machine control in Laser Powder Bed Fusion: A review”. In: Additive Manufacturing 45 (2021), p. 102058.

[99] Peter Warren et al. “Effect of sintering temperature on microstructure and mechanical properties of molded Martian and Lunar regolith”. In: Ceramics International 48.23 (2022), pp. 35825–35833.

[100] Rui Liu, Sen Liu, and Xiaoli Zhang. “A physics-informed machine learning model for porosity analysis in laser powder bed fusion additive manufacturing”. In: The International Journal of Advanced Manufacturing Technology 113.7-8 (2021), pp. 1943–1958.

[101] W Zouhri et al. “Optical process monitoring for Laser-Powder Bed Fusion (L-PBF)”. In: CIRP Journal of Manufacturing Science and Technology 31 (2020), pp. 607–617.

[102] Peter Warren et al. “Rapid Defect Detection and Classification in Images Using Convolutional Neural Networks”. In: Turbo Expo: Power for Land, Sea, and Air. Vol. 84966. American Society of Mechanical Engineers. 2021, V004T05A013.

[103] Qi Tian et al. “Deep learning-based data fusion method for in situ porosity detection in laser-based additive manufacturing”. In: Journal of Manufacturing Science and Engineering 143.4 (2021), p. 041011.

[104] Alessandra Caggiano et al. “Machine learning-based image processing for on-line defect recognition in additive manufacturing”. In: CIRP annals 68.1 (2019), pp. 451–454.

[105] M Mills. “Introduction to the measurement of roundness”. In: Taylor-Hobson Precision, online (2010).

[106] Yann LeCun et al. “Gradient-based learning applied to document recognition”. In: Proceedings of the IEEE 86.11 (1998), pp. 2278–2324.

[107] Sebastian Wilhelm and Manfred Curbach. “Review of possible mineral materials and production techniques for a building material on the moon”. In: Structural Concrete 15.3 (2014), pp. 419–428.

[108] Melanie Bodiford et al. “In-situ resource-based lunar and martian habitat structures development at NASA/MSFC”. In: 1st space exploration conference: Continuing the voyage of discovery. 2005, p. 2704.

[109] Lisa C Simonsen et al. “Space radiation shielding for a martian habitat”. In: SAE transactions (1990), pp. 972–979.

[110] Florian Ruess, J Schaenzlin, and H Benaroya. “Structural design of a lunar habitat”. In: Journal of Aerospace Engineering 19.3 (2006), pp. 133–157.

[111] Jack Miller et al. “Lunar soil as shielding against space radiation”. In: Radiation Measurements 44.2 (2009), pp. 163–167.

[112] Lisa C Simonsen and John E Nealy. “Radiation Protection for H un1an Missions to the Moon and Mars”. In: NASA TP 3079 (1991).

[113] Tony C Slaba, Chris J Mertens, and Steve R Blattnig. Radiation shielding optimization on Mars. Tech. rep. National Aeronautics and Space Administration (NASA), 2013.

[114] Brian J Chow et al. “Direct formation of structural components using a martian soil simulant”. In: Scientific reports 7.1 (2017), pp. 1–8.

[115] Alexandre Meurisse et al. “Solar 3D printing of lunar regolith”. In: Acta Astronautica 152 (2018), pp. 800–810.

[116] Rashmi Dikshit et al. "Space bricks: From LSS to machinable structures via MICP". In: Ceramics International 47.10 (2021), pp. 14892–14898.

[117] Rashmi Dikshit et al. "Microbially induced calcite precipitation using Bacillus velezensis with guar gum". In: PloS one 15.8 (2020), e0236745.

[118] Aloke Kumar et al. "Bacterial Growth Induced Biocementation Technology,'Space-Brick'-A Proposal for Experiment at Microgravity and Planetary Environments". In: bioRxiv (2020).

[119] Lin Wan, Roman Wendner, and Gianluca Cusatis. "A novel material for in situ construction on Mars: experiments and numerical simulations". In: Construction and Building Materials 120 (2016), pp. 222–231.

[120] Behrokh Khoshnevis et al. "Construction by Contour Crafting using sulfur concrete with planetary applications". In: Rapid Prototyping Journal (2016).

[121] Matthew Troemner et al. "Marscrete: A Martian Concrete for Additive Construction Applications Utilizing In Situ Resources". In: Earth and Space 2021. 2020, pp. 801–807.

[122] Mohsen Ziaee and Nathan B Crane. "Binder jetting: A review of process, materials, and methods". In: Additive Manufacturing 28 (2019), pp. 781–801.

[123] Ian Gibson et al. "Binder jetting". In: Additive manufacturing technologies. Springer, 2021, pp. 237–252.

[124] David Karl et al. "Sintering of ceramics for clay in situ resource utilization on Mars". In: Open Ceramics 3 (2020), p. 100008.

[125] Carole McLemore. "The need for lunar simulants". In: LPI contributions 1515 (2009).

[126] Altan Alpay Altun et al. "Additive manufacturing of lunar regolith structures". In: Open Ceramics 5 (2021), p. 100058.

[127] Jiawen Liu et al. “In-situ Resources for Infrastructure Construction on Mars: A Review”. In: International Journal of Transportation Science and Technology (2021).

[128] Kevin M Cannon et al. “Mars global simulant MGS-1: A Rocknest-based open standard for basaltic martian regolith simulants”. In: Icarus 317 (2019), pp. 470–478.

[129] Zoe Landsman and Daniel Britt. “Simulated Asteroid and Planetary Materials at the CLASS Exolith Lab”. In: European Planetary Science Congress. 2020, EPSC2020–906.

[130] Carlton C Allen et al. “Martian regolith simulant JSC Mars-1”. In: Lunar and planetary science conference. 1690. 1998, p. 1690.

[131] Maxim Isachenkov et al. “Regolith-based additive manufacturing for sustainable development of lunar infrastructure–An overview”. In: Acta Astronautica (2021).

[132] Benton C Clark and Daniel C Van Hart. “The salts of Mars”. In: Icarus 45.2 (1981), pp. 370–378.

[133] Edward Mc Cullough and Andrew Cutler. “ISRU lunar processing research at Boeing”. In: 39th Aerospace Sciences Meeting and Exhibit. 2001, p. 938.

[134] Hans Rickman et al. “Water in the history of Mars: An assessment”. In: Planetary and Space Science 166 (2019), pp. 70–89.

[135] ASTM C1314-21, Standard Test Method for Compressive Strength of Masonry Prisms. Tech. rep. ASTM International, West Conshohocken, PA, 2021.

[136] KS Gumaste et al. “Strength and elasticity of brick masonry prisms and wallettes under compression”. In: Materials and structures 40.2 (2007), pp. 241–253.

[137] AW Page. “The biaxial compressive strength of brick masonry.” In: Proceedings of the Institution of Civil Engineers 71.3 (1981), pp. 893–906.

[138] SB Singh and Pankaj Munjal. “Bond strength and compressive stress-strain characteristics of brick masonry”. In: Journal of Building Engineering 9 (2017), pp. 10–16.

[139] Houssam A Toutanji, Steve Evans, and Richard N Grugel. “Performance of lunar sulfur concrete in lunar environments”. In: Construction and Building Materials 29 (2012), pp. 444–448.

[140] TD Lin, H Love, and David Stark. “Physical properties of concrete made with Apollo 16 lunar soil sample”. In: NASA. Johnson Space Center, Volume 2. 1992.

[141] Alexandre Meurisse et al. “Influence of mineral composition on sintering lunar regolith”. In: Journal of Aerospace Engineering 30.4 (2017), p. 04017014.

[142] Giovanni Cesaretti et al. “Building components for an outpost on the Lunar soil by means of a novel 3D printing technology”. In: Acta Astronautica 93 (2014), pp. 430–450.

[143] David Karl et al. “Clay in situ resource utilization with Mars global simulant slurries for additive manufacturing and traditional shaping of unfired green bodies”. In: Acta Astronautica 174 (2020), pp. 241–253.

[144] David Karl et al. “Towards the colonization of Mars by in-situ resource utilization: Slip cast ceramics from Martian soil simulant”. In: PloS one 13.10 (2018), e0204025.

[145] Jean Lemaitre and Rodrigue Desmorat. Engineering damage mechanics: ductile, creep, fatigue and brittle failures. Springer Science & Business Media, 2006.

[146] Yujia Wang and Yaoyao Fiona Zhao. “Investigation of sintering shrinkage in binder jetting additive manufacturing process”. In: Procedia Manufacturing 10 (2017), pp. 779–790.

[147] Dan Britt. Exolith Lab. `https://sciences.ucf.edu/class/exolithlab/`. 2021.

[148] Xingfen Chen et al. “Study of melting properties of basalt based on their mineral components”. In: Composites Part B: Engineering 116 (2017), pp. 53–60.

[149] D Lynn Johnson and Ivan B Cutler. “Diffusion sintering: I, initial stage sintering models and their application to shrinkage of powder compacts”. In: Journal of the American Ceramic Society 46.11 (1963), pp. 541–545.

[150] Randall M German. “Computer modeling of sintering processes”. In: International Journal of Powder Metallurgy 38.2 (2002), pp. 48–66.

[151] Randall M German. “Sintering trajectories: description on how density, surface area, and grain size change”. In: Jom 68.3 (2016), pp. 878–884.

[152] M Sahli et al. “Numerical simulation and experimental analysis of solid-state sintering response of 316 L stainless steel micro-parts manufactured by metal injection molding”. In: The International Journal of Advanced Manufacturing Technology 79.9 (2015), pp. 2079–2092.

[153] Ijaz Ul Mohsin et al. “Finite element sintering analysis of metal injection molded copper brown body using thermo-physical data and kinetics”. In: Computational materials science 53.1 (2012), pp. 6–11.

[154] Kedarnath Rane and Matteo Strano. “A comprehensive review of extrusion-based additive manufacturing processes for rapid production of metallic and ceramic parts”. In: Advances in Manufacturing 7.2 (2019), pp. 155–173.

[155] Aghnia Ilmiah Nurhudan et al. “Additive manufacturing of metallic based on extrusion process: a review”. In: Journal of Manufacturing Processes 66 (2021), pp. 228–237.

[156] Andrea Zocca et al. “Additive manufacturing of ceramics: issues, potentialities, and opportunities”. In: Journal of the American Ceramic Society 98.7 (2015), pp. 1983–2001.

[157] J-P Kruth et al. “Binding mechanisms in selective laser sintering and selective laser melting”. In: Rapid prototyping journal (2005).

[158] Peter Warren et al. “Modeling Thermally Grown Oxides in Thermal Barrier Coatings Using Koch Fractal”. In: Turbo Expo: Power for Land, Sea, and Air. Vol. 58677. American Society of Mechanical Engineers. 2019, V006T24A019.

[159] Peter Warren et al. “Investigating Load Transfer in Ceramic Reinforcements”. In: Turbo Expo: Power for Land, Sea, and Air. Vol. 51128. American Society of Mechanical Engineers. 2018, V006T02A012.

[160] Hessein Ali et al. “Computational model of mechano-electrochemical effect of aluminum alloys corrosion”. In: Journal of Engineering for Gas Turbines and Power 144.4 (2022), p. 041004.

[161] Liubov Magerramova, Boris Vasilyev, and Vladimir Kinzburskiy. “Novel designs of turbine blades for additive manufacturing”. In: Turbo Expo: Power for Land, Sea, and Air. Vol. 49804. American Society of Mechanical Engineers. 2016, V05CT18A001.

[162] Audrey Gaymann, Francesco Montomoli, and Marco Pietropaoli. “Design for additive manufacturing: valves without moving parts”. In: Turbo Expo: Power for Land, Sea, and Air. Vol. 50800. American Society of Mechanical Engineers. 2017, V02CT47A022.

[163] Jacob C Snyder and Karen A Thole. “Effect of additive manufacturing process parameters on turbine cooling”. In: Turbo Expo: Power for Land, Sea, and Air. Vol. 58653. American Society of Mechanical Engineers. 2019, V05BT21A002.

[164] Randall M German. “Sintering simplified: Surface area, density, and grain size relations”. In: Materials Science Forum. Vol. 835. Trans Tech Publ. 2016, pp. 50–75.

[165] Wayne S Rasband et al. ImageJ. 1997.

[166] Ian Nettleship, Mitchell D Lehigh, and Rangan Sampathkumar. “Microstructural pathways for the sintering of alumina ceramics”. In: Scripta materialia 37.4 (1997).

[167] W Beere. “The sintering and morphology of interconnected porosity in UO 2 powder compacts”. In: Journal of Materials Science 8.12 (1973), pp. 1717–1724.